

Author(s)	Collins, Brian Harris
Title	Thermal imagery spectral analysis
Publisher	Monterey, California. Naval Postgraduate School
Issue Date	1996 09
URL	<a href="http://hdl.handle.net/10945/39300">http://hdl.handle.net/10945/39300</a>

This document was downloaded on May 04, 2015 at 22:43:48



<http://www.nps.edu/library>

Calhoun is a project of the Dudley Knox Library at NPS, furthering the precepts and goals of open government and government transparency. All information contained herein has been approved for release by the NPS Public Affairs Officer.

**Dudley Knox Library / Naval Postgraduate School  
411 Dyer Road / 1 University Circle  
Monterey, California USA 93943**



<http://www.nps.edu/>

# NAVAL POSTGRADUATE SCHOOL MONTEREY, CALIFORNIA



## THESIS

**THERMAL IMAGERY SPECTRAL ANALYSIS**

by

Brian Harris Collins

September, 1996

Thesis Advisor:

R. C. Olsen

19970123 039

Approved for public release; distribution is unlimited.

DTIC QUALITY ASSURED

# REPORT DOCUMENTATION PAGE

Form Approved OMB No. 0704-0188

Public reporting burden for this collection of information is estimated to average 1 hour per response, including the time for reviewing instruction, searching existing data sources, gathering and maintaining the data needed, and completing and reviewing the collection of information. Send comments regarding this burden estimate or any other aspect of this collection of information, including suggestions for reducing this burden, to Washington Headquarters Services, Directorate for Information Operations and Reports, 1215 Jefferson Davis Highway, Suite 1204, Arlington, VA 22202-4302, and to the Office of Management and Budget, Paperwork Reduction Project (0704-0188) Washington DC 20503.

1. AGENCY USE ONLY (Leave blank)	2. REPORT DATE September 1996	3. REPORT TYPE AND DATES COVERED Master's Thesis	
4. TITLE AND SUBTITLE TITLE OF THESIS. Thermal Imagery Spectral Analysis		5. FUNDING NUMBERS	
6. AUTHOR(S) Brian Harris Collins		8. PERFORMING ORGANIZATION REPORT NUMBER	
7. PERFORMING ORGANIZATION NAME(S) AND ADDRESS(ES) Naval Postgraduate School Monterey CA 93943-5000			
9. SPONSORING/MONITORING AGENCY NAME(S) AND ADDRESS(ES)		10. SPONSORING/MONITORING AGENCY REPORT NUMBER	
11. SUPPLEMENTARY NOTES The views expressed in this thesis are those of the author and do not reflect the official policy or position of the Department of Defense or the U.S. Government.			
12a. DISTRIBUTION/AVAILABILITY STATEMENT Approved for public release; distribution is unlimited.		12b. DISTRIBUTION CODE	
13. ABSTRACT (maximum 200 words) The first thermal imagery from the Spatially Enhanced Broadband Array Spectrograph System (SEBASS) was analyzed for target detection purposes. Data were acquired during Exercise WESTERN RAINBOW in October of 1995 with Aerospace Corporation's new instrument. SEBASS is a thermal infrared spectral imaging system which collects data in 128 wavelength bands from 7.8 to 13.4 $\mu\text{m}$ . The system has 128 spatial pixels and a ground sample distance of 2.5 feet under the operating conditions of the exercise. The data reduction process included thermal calibration using on-board calibration sources, atmospheric correction through the use of in-scene data, and derivation of thermal emissivity. Analysis of the data was performed using techniques adopted from hyperspectral imagery. The application of the principal components transformation, the spectral angle mapper, and a spectral matched filter showed substantial enhancement of target detection capabilities when compared to the analysis of standard infrared imagery.			
14. SUBJECT TERMS Hyperspectral, Thermal, Spectroscopy, Imagery, Support to Military Operations, SEBASS, Remote Sensing		15. NUMBER OF PAGES 180	
17. SECURITY CLASSIFICATION OF REPORT Unclassified		16. PRICE CODE	
		20. LIMITATION OF ABSTRACT UL	
18. SECURITY CLASSIFICATION OF THIS PAGE Unclassified	19. SECURITY CLASSIFICATION OF ABSTRACT Unclassified		

NSN 7540-01-280-5500

Standard Form 298 (Rev. 2-89)  
Prescribed by ANSI Std. Z39-18 298-102



**Approved for public release; distribution is unlimited.**

**THERMAL IMAGERY SPECTRAL ANALYSIS**

Brian Harris Collins  
Captain, United States Marine Corps  
B.S., Rice University, 1990

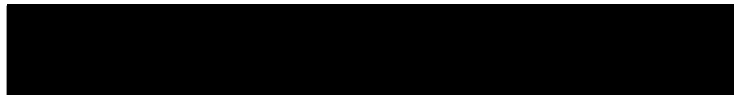
Submitted in partial fulfillment  
of the requirements for the degree of

**MASTER OF SCIENCE IN SYSTEMS TECHNOLOGY  
(SPACE SYSTEMS OPERATIONS)**

from the

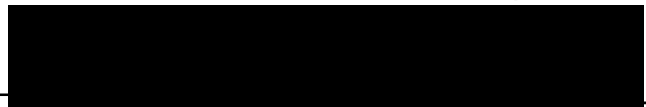
**NAVAL POSTGRADUATE SCHOOL  
September 1996**

Author:



Brian Harris Collins

Approved by:



R. C. Olsen, Thesis Advisor



David Cleary, Co-Advisor



 Rudy Panholtzer, Chairman  
Space Systems Academic Group



## ABSTRACT

The first thermal imagery from the Spatially Enhanced Broadband Array Spectrograph System (SEBASS) was analyzed for target detection purposes. Data were acquired during Exercise WESTERN RAINBOW in October of 1995 with Aerospace Corporation's new instrument. SEBASS is a thermal infrared spectral imaging system which collects data in 128 wavelength bands from 7.8 to 13.4  $\mu\text{m}$ . The system has 128 spatial pixels and a ground sample distance of 2.5 feet under the operating conditions of the exercise. The data reduction process included thermal calibration using on-board calibration sources, atmospheric correction through the use of in-scene data, and derivation of thermal emissivity. Analysis of the data was performed using techniques adopted from hyperspectral imagery. The application of the principal components transformation, the spectral angle mapper, and a spectral matched filter showed substantial enhancement of target detection capabilities when compared to the analysis of standard infrared imagery.



# TABLE OF CONTENTS

I. INTRODUCTION .....	1
II. INFRARED HYPERSPECTRAL REMOTE SENSING.....	5
A. SPECTRAL REMOTE SENSING .....	6
1. Electromagnetic Spectrum .....	6
a. Visible, Near Infrared, and Shortwave Infrared .....	7
b. Midwave Infrared and Longwave Infrared.....	7
2. Spectral Resolution .....	8
a. Multispectral Sensors .....	9
b. Hyperspectral Sensors.....	9
c. Ultraspectral Sensors.....	10
B. INFRARED REMOTE SENSING.....	10
1. The Planck Function .....	11
2. Molecular Properties .....	12
3. Radiative Transfer.....	14
4. Atmospheric Effects.....	15
a. Atmospheric Models .....	16
b. Empirical Line Method .....	16
c. Plastic Ruler Atmospheric Compensation Technique.....	17
C. HYPERSPECTRAL DATA ANALYSIS .....	18
1. Principal Components Analysis .....	19
2. Spectral Angle Mapper .....	21
3. Spectral Matched Filter.....	22
III. THE DEVELOPMENT OF THE SPATIALLY ENHANCED BROADBAND ARRAY SPECTROGRAPH SYSTEM (SEBASS).....	25
A. THERMAL INFRARED MAPPING SCANNER (TIMS).....	25
B. THE BROADBAND ARRAY SPECTROGRAPH SYSTEM (BASS) .....	26
1. Instrument Design .....	27
2. SMO Utility .....	27
C. THE SPATIALLY ENHANCED BROADBAND ARRAY SPECTROGRAPH SYSTEM .....	28
1. Instrument Design .....	28
2. Data Format and Use.....	29
a. Spectral Calibration.....	30
b. Radiometric Calibration.....	31
IV. EXERCISE WESTERN RAINBOW .....	33
A. EXERCISE SCENARIO.....	33

B. COLLECTION SITES .....	34
1. Malpai Site .....	35
2. JCCD Tank and Artillery Site.....	36
3. Arroyo Site TBM Site .....	38
C. GROUND COLLECTION EQUIPMENT.....	39
D. AIRBORNE COLLECTION EQUIPMENT .....	39
V. EXPERIMENT OBSERVATIONS .....	41
A. YUMA PROVING GROUND OBSERVATIONS .....	41
1. Collection Sites .....	41
2. Weather Conditions .....	42
B. SEBASS PERFORMANCE.....	42
1. Flight Operations .....	42
2. Sensor Performance .....	43
C. GROUND TRUTH OBSERVATIONS .....	44
D. HYPERSPECTRAL OBSERVATIONS .....	45
1. Hyperspectral Image Data.....	46
2. Data Preparation.....	46
a. Spectral and Radiometric Calibration .....	47
b. Generation of a Simulated, FLIR Image.....	47
c. Atmospheric Correction .....	47
d. Conversion to Apparent Emissivity .....	49
3. Hardware and Software Configuration .....	49
VI. DATA ANALYSIS.....	51
A. MALPAI COLLECTION SITE - 20 OCTOBER 1995.....	51
1. Data Processing.....	51
2. Single-band Images.....	52
3. Principal Components Analysis .....	53
a. Radiance Data Sets.....	53
b. PCA Results on Calibrated Data Set.....	54
c. Principal Components Analysis on Emissivity Data Set.....	56
4. Spectral Angle Mapper Analysis .....	57
a. SAM Analysis Using Ground Truth Spectra.....	57
b. SAM Analysis Using Ground Truth and Extracted Spectra .....	58
5. Spectral Matched Filter Analysis.....	59
B. JCCD COLLECTION SITE - 23 OCTOBER 1995.....	60
1. Data Processing.....	60
2. JCCD Decoy Line One - 23 October 1995 .....	60
a. Single-band Images .....	60
b. Principal Components Analysis.....	61
c. Spectral Angle Mapper Analysis.....	62
d. Spectral Matched Filter Analysis .....	63

3. JCCD Decoy Line Two - 23 October 1995.....	64
a. Single-band Images.....	64
b. Principal Components Analysis.....	64
c. Spectral Angle Mapper Analysis.....	65
d. Spectral Matched Filter Analysis.....	66
4. JCCD Vehicle Target Line - 23 October 1995.....	66
a. Single-band Images.....	66
b. Principal Components Analysis.....	67
c. Spectral Angle Mapper Analysis.....	67
d. Spectral Matched Filter Analysis.....	67
C. ARROYO COLLECTION SITE - 23 OCTOBER 1995.....	68
1. Data Processing.....	68
2. Single-band Images.....	68
3. Principal Components Analysis.....	69
4. Spectral Angle Mapper Analysis.....	69
5. Spectral Matched Filter Analysis.....	70
D. TARGET DETECTION RESULTS.....	70
VII. SUMMARY AND CONCLUSIONS.....	73
APPENDIX A. FIGURES.....	77
APPENDIX B. ATMOSPHERIC COMPENSATION ALGORITHM.....	151
LIST OF REFERENCES.....	159
INITIAL DISTRIBUTION LIST.....	163



## LIST OF SYMBOLS

$\lambda$	wavelength
$T$	temperature
$L_{xx}$	radiance from source XX [ $\mu W/cm^2 \mu m sr$ ]
$\epsilon_\lambda$	emissivity
$\alpha_\lambda$	absorptivity
$\rho_\lambda$	reflectivity
$\tau_\lambda$	atmospheric transmittance



## ACKNOWLEDGEMENTS

The author would like to thank John Hackwell of The Aerospace Corporation for the opportunity to work with SEBASS in its initial development. Special thanks to Thomas Hayhurst and Bob Johnson also of The Aerospace Corporation for sharing their expertise in spectral remote sensing. The author would also like to thank Wayne Wilson and Sharon Yamasaki of Photon Research Associates for their assistance. Programmatic support for this research was provided by Bob Alexander of the Office of Research and Development, Central Intelligence Agency.

## I. INTRODUCTION

Rapid advances in remote sensing technologies have led to new sensors which greatly improve our ability to gather information about distant objects without direct physical contact. While many of these sensors and technologies were designed for environmental monitoring and earth science, they may have important uses in the Department of Defense (DOD) as today's warfighter strives to gain a complete picture of the battlespace around him. As the numbers and capabilities of these sensors continue to grow, the evaluation of their capabilities in a support to military operations (SMO) setting has become increasingly important.

Hyperspectral imagery is one of the most promising of these emerging technologies. Hyperspectral imaging refers to a version of imaging spectroscopy in which measurements of reflected or emitted light are taken in hundreds of narrow spectral bands (Multispectral Users Guide, 1995). Because the reflection or emission of electromagnetic energy is characteristic of a material's molecular makeup, this high resolution trace of radiation versus wavelength can form a graphical record unique to a given material (Rinker, 1990). The high spectral resolution of hyperspectral sensors can provide opportunities to detect subtle differences between material signatures. From the standpoint of military targeting and identification, hyperspectral sensors have a potential beyond many previous remote sensing instruments.

Most hyperspectral instruments, like the Airborne Visible/Infrared Imaging Spectrometer (AVIRIS) and the Hyperspectral Digital Imagery Collection Experiment (HYDICE), collect information in the region of the electromagnetic spectrum dominated by solar illumination. These instruments acquire a complete reflectance spectrum by recording the reflected solar radiation from an object. Although these sensors have achieved success in material identification, they are ineffective at night in the absence of solar illumination. The Aerospace Corporation created the Spatially Enhanced Broadband Array Spectrograph System (SEBASS) to extend the range of hyperspectral sensors into the thermal infrared region. In contrast to the visible region of the electromagnetic spectrum, the infrared region is dominated by thermal self-emission.

This allows the sensor to operate equally well during both day and night. Thermal infrared hyperspectral sensors have the potential to perform target detection, terrain categorization, and materials classification regardless of illumination conditions. They achieve this by examining the emissivity differences between target objects in the same way that visible hyperspectral sensors examine differences in solar reflectivity. Because of its freedom from the restraint of solar illumination, SEBASS may represent a step forward in the SMO capabilities of hyperspectral sensors.

The analysis of hyperspectral imagery differs dramatically from the literal interpretation of single-band imagery because of the nature of hyperspectral data. By recording measurements in hundreds of spectral bands, hyperspectral sensors generate large amounts of data that require complex methods of analysis (Multispectral Users Guide, 1995). Unlike single-band systems in which target detection is based on contrast and spatial resolution, hyperspectral sensors discriminate between various target and background types on the basis of their reflective or emissive characteristics. Many techniques have been devised to accomplish this spectral analysis. The overall shape of a target's radiation curve can be compared to known laboratory measurements. The locations of specific features within several spectral curves may be recorded and compared. Even statistical analysis of the variations between all of the spectral data within an entire scene can lead to significant information about scene content. The choice and application of a particular technique has a direct impact on the ability of the sensor/algorithm combination to detect or classify a target.

The MASINT Hyperspectral Study (MHS) was initiated in 1993 to assess the utility of hyperspectral imagery (MHS: Interim Progress Report, 1995). The MHS defined three SMO goals to guide its efforts:

- Find threat vehicles and defeat Camouflage, Concealment, and Deception (CCD) efforts better than currently done
- Improve current capabilities for the categorization of terrain features
- Demonstrate the utility of thermal hyperspectral products for military and terrain categorization problems (MHS: Interim Progress Report, 1995).

In support of these goals, the MHS program sponsored Exercise WESTERN RAINBOW at the Yuma Proving Ground, Arizona, in October 1995. During this exercise, a variety of airborne and ground-based hyperspectral sensors were employed in a SMO scenario.

This thesis will present an assessment of SEBASS and its capability to conduct SMO missions. It evaluates the utility of thermal hyperspectral products for military and terrain categorization problems using data collected during WESTERN RAINBOW. A description of hyperspectral remote sensing theory and hyperspectral data analysis techniques is presented in Chapter II. Chapter III is a discussion of the history and development of SEBASS. The experimental setup of Exercise WESTERN RAINBOW is outlined in Chapter IV while the experimental observations collected during the exercise are described in Chapter V. Chapter V also includes ground truth measurements, SEBASS data set descriptions, and a complete description of the SEBASS data preparation process. Spatial and spectral analysis of the WESTERN RAINBOW data is discussed in Chapter VI. Finally, Chapter VII will present the conclusions drawn from the analysis of SEBASS data collected during the exercise.



## II. INFRARED HYPERSPECTRAL REMOTE SENSING

The goal of spectral remote sensing is the identification of material through the examination of reflected or emitted electromagnetic radiation. All materials have a unique spectral signature based on their ability to reflect or emit electromagnetic energy at different wavelengths. The spectral signature of an object is usually presented as a reflectance or emittance spectrum. A reflectance spectrum graphically depicts the ability of an object to reflect incident electromagnetic radiation at different wavelengths. An emittance spectrum depicts the ability of a material to emit thermal energy.

Figure 2.1 depicts the differences between the reflectance spectrum of healthy vegetation and two types of camouflage (Multispectral Users Guide, 1995). The figure illustrates how spectral information can be used to identify and discriminate between materials based on their spectral properties. From 0.4 to 0.7  $\mu\text{m}$ , all three materials appear similar. This wavelength region corresponds to the visible portion of the electromagnetic spectrum and confirms that modern camouflage is designed to simulate natural vegetation. At wavelengths longer than 0.7  $\mu\text{m}$ , significant differences between the man-made camouflage and natural vegetation begin to become discernible. Sensors able to record electromagnetic radiation at these longer wavelengths would be able to discriminate between all three types of objects.

The ability of a sensor to detect subtle spectral differences between objects depends on several factors. As shown in the discussion of Figure 2.1, different regions of the electromagnetic spectrum can reveal differences between materials that may not otherwise be detectable. Also, a high spectral resolution sensor will be able to detect small, unique features within a particular spectrum. For example, the sensor used to collect the data for Figure 2.1 has a spectral resolution better than 0.05  $\mu\text{m}$ . This narrow bandwidth allows the sensor to accurately measure the narrow drop in reflectivity at 1.45  $\mu\text{m}$  in the spectrum of green vegetation. The atmosphere between an object and the sensor can also affect the quality of the reflectance or emittance spectrum collected by an instrument. Molecules within the atmosphere absorb, emit, and scatter electromagnetic energy. Sensors which are designed to exploit the differences between spectra collected

from ground materials must have a method of compensating for these degrading effects which can mask the true emission characteristics of the target material. Finally, spectral data analysis techniques vary in their ability to detect and exploit features within collected spectral data.

This chapter presents a description of infrared hyperspectral remote sensing. It begins with a description of the principles of spectral remote sensing. The specific characteristics of infrared remote sensing are then presented. Finally, it concludes with a discussion of several classes of hyperspectral data analysis techniques.

## **A. SPECTRAL REMOTE SENSING**

Spectral sensors are designed to exploit particular regions of the electromagnetic spectrum in an effort to take advantage of the properties of electromagnetic radiation at different wavelengths. A sensor may be designed to operate during periods of low solar illumination, to detect a characteristic spectral feature of a target material, or to discriminate between several types of minerals. To satisfy these different uses, the number of spectral bands measured by remote sensing instruments as well as their width and location within the electromagnetic spectrum will vary. These characteristics are selected to achieve the level of resolution required to satisfy the sensor's intended goal.

### **1. Electromagnetic Spectrum**

The portion of the electromagnetic spectrum used most frequently in spectral remote sensing ranges from 0.2  $\mu\text{m}$  to 14.0  $\mu\text{m}$ . Figure 2.2 graphically depicts this region of the spectrum (Multispectral Users Guide, 1995). Sensors operating in the region from 0.2  $\mu\text{m}$  to 2.5  $\mu\text{m}$  collect and record reflected solar energy. In the transition region between 2.5  $\mu\text{m}$  and 8.0  $\mu\text{m}$ , both reflected solar energy and thermal self-emission contribute to the electromagnetic energy measured by a sensor. Between 8.0 and 14.0  $\mu\text{m}$ , thermal self-emission dominates the observed spectrum. Sensors operating at

wavelengths longer than 8.0  $\mu\text{m}$  collect emitted radiation and do not depend on reflected solar illumination.

*a. Visible, Near Infrared, and Shortwave Infrared*

Spectral imagery in the visible, near infrared (NIR), and shortwave infrared (SWIR) region of the electromagnetic spectrum is dominated by the reflection of solar energy. Visible light ranges from 0.4  $\mu\text{m}$  to 0.7  $\mu\text{m}$  and is usually classified according to color. The shorter wavelengths correspond to blue light while the longer wavelengths correspond to red light. The reflectance of many materials differ within the visible region providing the many variations of color we observe between objects (Anderson, et al, 1994). The NIR (0.7 to 1.1  $\mu\text{m}$ ) and SWIR (1.1 to 2.5  $\mu\text{m}$ ) regions of the electromagnetic spectrum, although not detectable by the human eye, are also dominated by the reflection of solar energy.

Sensors operating in the visible, NIR, and SWIR regions exploit variations in the ability of objects to reflect radiation. Energy in the blue region of visible light is absorbed by chlorophyll. It also can penetrate clear water to a depth of about 40m (Multispectral Users Guide, 1995). Reflected energy in the visible red region has been useful for vegetation and soil discrimination (Multispectral Users Guide, 1995). NIR reflectance is used for vegetation analysis because it is strongly affected by the cellular structure of leaf tissue. Sensors operating in the SWIR region are used to detect moisture content and highlight the contrast between vegetation types.

*b. Midwave Infrared and Longwave Infrared*

Thermal emission of radiation becomes a significant factor in the midwave infrared (MWIR) and longwave infrared (LWIR) regions of the electromagnetic spectrum. MWIR radiation includes wavelengths from 3.0 to 5.0  $\mu\text{m}$ . The LWIR region extends from 8.0 to 14.0  $\mu\text{m}$ . In these longer wavelength regions, materials emit more radiation than they reflect from the sun. As a result, sensors which operate within this region are not constrained by solar illumination. Variations in the ability of materials to

emit radiation are the thermal infrared counterpart to reflectance variations that are used for material discrimination in visible, NIR, and SWIR remote sensing.

During the day, MWIR energy is a mix of reflected and emitted energy. At night, the reflected solar component is reduced and the energy recorded by a sensor operating in the MWIR region consists almost entirely of emitted radiation. MWIR imagery can be used to penetrate smoke and has been used to measure surface temperature (Multispectral Users Guide, 1995). LWIR imagery has traditionally been used for thermal temperature measurements. LWIR sensors and emittance spectra can also be used to conduct vegetation classification and perform geologic mapping (Multispectral Users Guide, 1995).

## **2. Spectral Resolution**

The spectral resolution of a sensor describes its ability to detect and record differences in reflected or emitted electromagnetic energy as a function of wavelength. Spectral resolution varies from sensor to sensor based on intended use and current technology. Low resolution sensors include single-band sensors which collect and record all electromagnetic energy within a broad spectral band as well as sensors which collect data in several wide wavelength bands. High resolution sensors record hundreds and even thousands of energy measurements in very narrow bands.

Single-band remote sensing instruments record the total electromagnetic energy received within a single wavelength band. Panchromatic photography and forward-looking infrared (FLIR) sensors are examples of single-band sensors (Anderson, et al, 1994). Panchromatic photography is sensitive to visible wavelength energy between 0.4  $\mu\text{m}$  and 0.7  $\mu\text{m}$ . FLIR sensors generally operate between 8  $\mu\text{m}$  and 12  $\mu\text{m}$ . Bright and dark areas within these images indicate high and low surface reflectances or warm and cold surfaces.

The drawback of single-band sensors is that many materials will appear similar within a single, wide band. The spectral features that distinguish one material from another may be very narrow or may be located in widely dispersed regions of the

electromagnetic spectrum. To increase the possibility of detecting these spectral differences, sensors which record the same scene in separate wavelength bands are used. Multi-band sensors are classified according to the number and width of their spectral bands. The three classes of multi-band sensors are multispectral, hyperspectral, and ultraspectral. Figure 2.3 depicts these three classes of sensors and their relative capabilities (Multispectral Users Guide, 1995).

*a. Multispectral Sensors*

Multispectral sensors have 2-20 spectral bands (Anderson, et al, 1994). These sensors take multiple images of a scene by collecting and recording radiation within each separate band. The bands selected for multispectral sensors do not need to be contiguous and often include a combination of visible, NIR, SWIR, MWIR and LWIR spectral bands. By comparing the recorded electromagnetic energy within these bands, multispectral sensors can perform terrain classification, camouflage detection, soil analysis, and trafficability analysis (Anderson, et al, 1994). A variety of airborne multispectral sensors have been developed including the current generation of Landsat and SPOT sensors. Table 2.1 is a summary of the bands employed in the Landsat Thematic Mapper multispectral instrument.

Band Number	Spectral Bands ( $\mu\text{m}$ )
1	0.45 - 0.52 (blue)
2	0.52 - 0.60 (green)
3	0.63 - 0.69 (red)
4	0.76 - 0.90 (NIR)
5	1.55 - 1.75 (SWIR)
6	10.4 - 12.5 (LWIR)
7	2.08 - 2.35 (SWIR)

Table 2.1. Landsat Thematic Mapper Spectral Bands. From Richards, 1993.

*b. Hyperspectral Sensors*

Hyperspectral sensors record data in hundreds of narrow, contiguous spectral bands (Multispectral Users Guide, 1995). "The increased number of sensor bands provides higher spectral resolution and more opportunities to detect subtle spectral

differences in signatures that are too narrow to be differentiated on multispectral imagery.” (Multispectral Users Guide, 1995) This increased spectral resolution allows the instrument to approximate the true reflectance or emittance spectrum of target objects and allow for the identification and classification of surface materials on a pixel-by-pixel basis (Goetz, et al, 1985). NASA's AVIRIS sensor (Vane, et al ,1993), the DOD HYDICE instrument (Rickard, et al, 1993), and Aerospace's SEBASS (Hackwell, et al, 1996) are examples of airborne hyperspectral sensors. AVIRIS and HYDICE operate in the visible, NIR, and SWIR regions of the electromagnetic spectrum. SEBASS collects data in the LWIR region of the spectrum. The basic characteristics of these sensors are listed in Table 2.2.

Instrument	Spectral Range ( $\mu\text{m}$ )	Number of Spectral Bands
AVIRIS	0.4 - 2.5	224
HYDICE	0.4 - 2.5	206
SEBASS	7.8 - 13.4	128

Table 2.2. Spectral Band Characteristics of Several Hyperspectral Sensors. After Vane, et al, 1993; Rickard, et al, 1993; and Hackwell, et al, 1996.

*c.      **Ultraspectral Sensors***

Ultraspectral sensors record data in thousand of contiguous spectral bands. They are useful for detecting narrow spectral phenomena within a small portion of the electromagnetic spectrum. This very high resolution capability has been used for specific material identification and molecular identification of aerosol and plume components (Multispectral Users Guide, 1995).

**B.      INFRARED REMOTE SENSING**

A spectral sensor collects reflected and emitted radiation from a source. The initial energy source may be the sun, thermal emission from the target object, or energy radiated from the sensor. In the LWIR region of the spectrum, the source of radiation is the target material itself. The radiation recorded by the sensor is the result of interactions between the source energy and the atmospheric constituents between the sensor and the

target. The goal of infrared remote sensing is to determine characteristics of the source object by working backwards from the measured radiance at the sensor. This requires an understanding of the emissive characteristics of materials as well as the radiative transfer process by which energy propagates through the atmosphere.

## 1. The Planck Function

All materials with a temperature above absolute zero emit radiation. To describe the manner in which an object radiates energy, the concept of a perfect radiation emitter, or blackbody, has been adopted. The amount of radiation emitted by a blackbody is a function of the temperature of the blackbody and the wavelength of emitted energy. Figure 2.4 is a graph of the radiation characteristics of several blackbodies at various temperatures. As the temperature of a blackbody increases, the amount of emitted radiation also increases. The figure also shows that the radiation emitted from a blackbody is not constant across the electromagnetic spectrum, but rises to a maximum and then gradually declines. The wavelength at which this peak of emitted radiation occurs decreases as the temperature of the blackbody increases. The equation governing blackbody radiation is called the Planck Radiation Law and is presented as Equation 2.1.

$$\text{Equation 2.1} \quad B_{\lambda}(T) = \frac{C_1 \lambda^{-5}}{e^{\frac{C_2}{\lambda T}} - 1} \quad [\mu W/cm^2 \mu m sr]$$

$$C_1 = 1.19104 \times 10^{10} \quad [\mu W/cm^2 \mu m sr]$$

$$C_2 = 1.438769 \times 10^4 \quad [\mu m K]$$

$$\lambda = \text{wavelength} \quad [\mu m]$$

$$T = \text{temperature} \quad [K]$$

The emission characteristics of real materials are described by comparing the thermal emission of a real object to a blackbody radiating at the same temperature. The ratio of these quantities is the spectral emissivity of an object as defined in Equation 2.2.

Equation 2.2       $\epsilon_{\lambda} = \frac{L_{emitted}}{B_{\lambda}(T)}$

$L_{emitted}$  = emitted radiance

The spectral emissivity of a material also describes its ability to absorb electromagnetic energy according to Kirchoff's law which states, "...for equilibrium conditions the absorptivity of a sample is exactly equal to its emissivity."(Zissis, 1993)

## 2. Molecular Properties

Electronic, vibrational, and rotational transitions within atoms and molecules account for the absorption, emission, and reflection properties of materials. Spectral features in the visible and ultraviolet regions of the electromagnetic spectrum are the products of electronic processes. Within the infrared region, spectral features are the results of molecular vibrations and rotations.

In general, atomic gases produce discrete absorption and emission features. Table 2.3 shows the prominent absorption features of several important gases. The discrete nature of absorption by gases produces the distinctive features in atmospheric transmission described below.

Species	Wavelength( $\mu\text{m}$ )
CO	4.66
CO <sub>2</sub>	2.7, 4.2, 14.99
N <sub>2</sub> O	4.5,7.78,16.98
H <sub>2</sub> O	2.73,6.27,15
O <sub>3</sub>	9.01,9.59,14.18

Table 2.3. Prominent Absorption Features of Atmospheric Gases.  
After Anderson, et al, 1994, and Zissis, 1993.

Liquids and solids produce broad absorption features. The absorption features of solids and liquids within the 0.4 - 14.0  $\mu\text{m}$  region of the electromagnetic spectrum are due to electronic and vibrational transitions at resonant frequencies. Between 0.4 and 2.5

$\mu\text{m}$ , spectral features are generally caused by electronic energy transitions within atoms and molecules. Above 2.5  $\mu\text{m}$ , vibrational absorption resonances are the primary source of spectral features. For a more complete description of the optical properties of materials, see Anderson, et al (1994).

Liquid water has a high absorption coefficient and is essentially opaque above 2.5  $\mu\text{m}$ . Figure 2.5 shows the reflectance of water for the 2.0 to 14.0  $\mu\text{m}$  region (Anderson, et al, 1994). Within this region, the reflectance of water is very low, ranging from 0.5% to 4.0%. This low reflectance indicates that the majority of incident radiation is absorbed. A water layer as thin as 0.1 mm is enough to absorb almost all longwave radiation. As a result, even a thin layer of moisture on a target can significantly affect the amount of radiation emitted or reflected from it.

Silicate minerals exhibit strong spectral features in the LWIR region. The nature of Si-O bonds causes fundamental vibrational absorption resonances above 8.0  $\mu\text{m}$ . These resonances, called reststrahlen bands, appear as minima in emissivity spectra. Figure 2.6 displays examples of emissive spectra from four different silicate minerals (Zissis, 1993). The reststrahlen feature can be seen in all four spectra as a minimum in the 8.0 to 11.0  $\mu\text{m}$  region. The location of the reststrahlen feature is different for each mineral because of varying percentages of silicate. This information can be used to classify and discriminate between various minerals.

Vegetation displays near-blackbody qualities in the thermal infrared region. Early measurements indicated that vegetation displayed very little spectral information in this region. More accurate and extensive data has recently indicated that although the spectral variations may be small, significant spectral information is present (Anderson, et al, 1994). The emissivity of vegetation can be altered by water content and degree of senescence. Figure 2.7 is a plot the reflectance spectra of healthy and senescent grass (John Hopkins University, 1995). The difference in overall shape between these two spectra is evident.

### 3. Radiative Transfer

Spectral sensors record the amount of energy received from a particular direction. They commonly measure incident energy in terms of radiance. Radiance is the amount of power per unit area that is incident on a surface from a particular direction. In the infrared region of the spectrum, radiance measured at a sensor is a combination of energy emitted by the target object, energy emitted by the surrounding background, and energy emitted or absorbed by the atmosphere between the object and the sensor (Multispectral Users Guide, 1995). Figure 2.8 depicts the various paths along which energy from these sources energy may travel to a sensor. Path 1 represents the target source energy. As described by Equations 2.1 and 2.2, the energy emitted by an object is a function of its temperature and emissivity. Not all of the energy emitted by an object reaches the sensor. A fraction is absorbed by atmospheric constituents and some is scattered in directions away from the sensor. To account for these effects, an additional factor, atmospheric transmittance, is introduced. Atmospheric transmittance is a measure of how much radiation will propagate through the atmosphere to the sensor. The contribution of energy from path 1 is described by Equation 2.3.

$$\text{Equation 2.3} \quad L_1 = \tau_\lambda \epsilon_\lambda B_\lambda(T) \quad \left[ \mu W / cm^2 \mu m \text{ sr} \right]$$

$\tau_\lambda = \text{atmospheric transmittance}$

The second source of energy reaching the sensor represents thermal energy emitted by the atmosphere onto an object and reflected toward the sensor. The energy emitted by the atmosphere toward the target surface is called downwelling radiance. The percentage of downwelling radiance that reaches the sensor is found by multiplying the downwelling radiance by the reflectivity of the material and the transmittance of the atmosphere. Within the thermal region, the reflectivity of most materials is generally small and can be calculated by subtracting the emissivity of an object from one. The contribution of path 2 is described by Equation 2.4.

$$\text{Equation 2.4} \quad L_2 = \tau_\lambda (1.0 - \epsilon_\lambda) L_{\text{downwelling}} \quad [\mu\text{W}/\text{cm}^2 \mu\text{m sr}]$$

$$L_{\text{downwelling}} = \text{atmospheric downwelling radiance}$$

Finally, energy emitted by the atmosphere may travel directly toward the sensor as depicted by path 3. This upwelling radiance is a function of the atmospheric constituents and ambient air temperature. The contribution of upwelling radiance is described in Equation 2.5.

$$\text{Equation 2.5} \quad L_3 = L_{\text{upwelling}} \quad [\mu\text{W}/\text{cm}^2 \mu\text{m sr}]$$

$$L_{\text{upwelling}} = \text{atmospheric upwelling radiance}$$

Equations 2.3 through 2.5 can be combined into a single equation representing all of the electromagnetic energy measured by a sensor. This equation is the radiative transfer equation for LWIR remote sensing and is presented as Equation 2.6. A more complete discussion of infrared radiative transfer is given in Kidder and Haar (1995).

$$\text{Equation 2.6} \quad L_{\text{sensor}} = \tau_\lambda \epsilon_\lambda B_\lambda(T) + \tau_\lambda (1.0 - \epsilon_\lambda) L_{\text{downwelling}} + L_{\text{upwelling}}$$

$$[\mu\text{W}/\text{cm}^2 \mu\text{m sr}]$$

#### 4. Atmospheric Effects

As mentioned above, the atmosphere affects the radiance measured at the sensor in several ways. Atmospheric constituents can attenuate and scatter solar radiation in the visible portion of the spectrum. In the thermal infrared region, the molecules in the atmosphere emit radiation and serve as a diffuse source of energy. General path losses from the target to the sensor can also alter the radiance measurements at the sensor.

Figure 2.9 shows the transmittance of the atmosphere throughout most of the electromagnetic spectrum (Kidder and Haar, 1995). Several 'windows' in which a large percentage of source radiation will propagate are evident. These are largely defined by

absorption due to water vapor and CO<sub>2</sub>. The 8.0 to 14.0 μm window is punctuated by ozone absorption at 9.6 μm and by water vapor absorption throughout the band.

The goal of atmospheric compensation is to accurately determine atmospheric transmittance as well as upwelling and downwelling radiance. Several methods have been devised to determine these parameters. Atmospheric compensation methods range from the use of detailed atmospheric models to the use of experimentally collected data.

*a. Atmospheric Models*

The cumulative effects of atmospheric attenuation and scattering can be determined using radiative transfer models. Most atmospheric models accept a standard set of input parameters that describe the environmental state and produce output parameters such as upwelling radiance and transmittance. Multispectral and hyperspectral sensor applications commonly employ a low resolution atmospheric transmittance model (LOWTRAN) and a moderate resolution model (MODTRAN) (Anderson, et al, 1994; Zisis, 1993). To increase the flexibility of atmospheric modeling, Aerospace Corporation developed the Atmospheric Radiance and Transmittance Spectra model (ARTSPEC) which estimates atmospheric parameters in the 2.8 - 14.0 μm range (Burke, 1995). ARTSPEC gains its flexibility through the use of a large variety of environmental inputs. The environmental parameters used as inputs for these models are usually collected on-site with meteorological instruments or estimated using the acquired spectral data.

*b. Empirical Line Method*

The empirical line method has been used extensively in the visible, NIR, and SWIR regions of the spectrum to derive surface reflectance (Farrand, et al, 1994). The empirical line method is based on the following equation:

Equation 2.7       $L_{sensor} = \rho_{\lambda} A + B$        $[\mu W/cm^2 \mu m sr]$

$\rho_{\lambda}$  = surface material reflectance

$A$  = multiplicative term ( $\tau_{\lambda}$  and instrument gain)

$B$  = additive term (path radiance and instrument offset)

The empirical line method solves for the multiplicative and additive terms in each wavelength band by examining one light and one dark target within the scene. The reflectance spectra of the two target materials must be known. Target reflectances are typically determined through laboratory analysis or the use of field spectrometers. Figure 2.10 demonstrates the empirical line method for a single band. The slope of the line drawn between the two points is the multiplicative term,  $A$ . The vertical offset represents the additive term,  $B$ . The process is repeated for each band of a multi-band imager. The resulting additive and multiplicative terms for each band are then applied to the entire data set to derive reflectance spectra for every pixel in the scene.

*c. Plastic Ruler Atmospheric Compensation Technique*

The plastic ruler atmospheric compensation method was developed by Hackwell and Hayhurst (1995) to derive atmospheric parameters for infrared hyperspectral collections using in-scene data. The method is based on a simplified version of the infrared radiative transfer equation (Equation 2.6). When the emissivity of a material equals 1.0, Equation 2.6 simplifies to Equation 2.8.

Equation 2.8       $L_{sensor} = \tau_{\lambda} B_{\lambda}(T) + L_{upwelling}$        $[\mu W/cm^2 \mu m sr]$

This equation is similar to Equation 2.7 which forms the foundation of the empirical line method. The plastic ruler atmospheric compensation algorithm attempts to determine the slope,  $\tau_{\lambda}$ , and offset,  $L_{upwelling}$ , of a set of points representing in-scene data. The process is complicated by the fact that the amount of radiation emitted from each data point in the scene,  $B_{\lambda}(T)$ , is a function temperature. The temperature of each point

must be estimated or measured prior to the solution of the above equation. In addition, determining the slope and offset of a cluster of points extracted directly from collected data is more difficult than simply drawing a straight line because the points do not all represent scene elements with emissivities close to 1.0.

Figure 2.11 can be used to explain the plastic ruler algorithm. The figure is a scatter plot of data values in a single wavelength band taken from a SEBASS collection mission during WESTERN RAINBOW. For each data point, the surface temperature has been estimated and the amount of radiation emitted by a blackbody at this estimated temperature,  $B_\lambda(T)$ , has been calculated. Each point is then plotted on a scatter plot of measured radiance versus blackbody radiance. The plastic ruler method solves for the atmospheric transmittance and upwelling radiance by drawing a line through the upper bound of the scatter plot. The points within the upper bound represent scene elements with emissivities close to 1.0. These points satisfy the simplified radiative transfer equation presented as Equation 2.8. The plastic ruler method employs Kolmogorov-Smirnov statistics and noise data from the instrument to find this upper bound.

The initial assumption that the emissivity of each scene element equals 1.0 somewhere within its spectrum results in relative atmospheric transmittance and upwelling radiance values instead of absolute corrections (Hackwell and Hayhurst, 1995). Burke (1995) combined the plastic ruler method with their ARTSPEC atmospheric model to derive absolute atmospheric corrections. The results from the plastic ruler method were used to guide the ARTSPEC atmospheric model. The ARTSPEC model input parameters were varied until the model's results exhibited the same relative shape as the plastic ruler results. The actual ARTSPEC model results could then be used for atmospheric compensation or as scaling factors for the plastic ruler results.

### **C.    HYPERSPPECTRAL DATA ANALYSIS**

A variety of data analysis techniques have been developed to exploit hyperspectral data. Hyperspectral analysis algorithms have been developed to find

matches for a particular target spectra within a scene, to detect anomalous spectra within a scene, and to classify the materials within a scene based on spectral properties. Three representative algorithms and techniques were applied to the data collected by SEBASS at WESTERN RAINBOW. These techniques included the principal components transformation, the spectral angle mapper, and a spectral matched filter.

## **1. Principal Components Analysis**

Hyperspectral image data consist of a series of images, each representing the reflection or emission of radiation within a particular frequency band. Because of the narrow, contiguous nature of hyperspectral bands, a high degree of correlation exists between these spectral images (Santisteban and Munoz, 1977). The principal components transformation is a rotational transformation that projects the hyperspectral data into a new coordinate system which is based on the variance of the original data. When the transformation is applied to hyperspectral data, the spectral information of the original image is transformed into a new set of orthogonal bands. The result is a series of decorrelated images, called principal component images. The number of images equals the number of original spectral bands.

A pictorial representation of the principal components transformation is presented in Figures 2.12 and 2.13. This example is taken from Richards (1993). These figures demonstrate the process on a two-band data set. The two figures are scatter plots of several data points plotted as band intensity values. The data in Figure 2.12 exhibit a high degree of correlation between the bands. An increase in band 1 is almost sufficient to predict an increase in band 2. The goal of principal components analysis (PCA) is to rotate the data into a coordinate system in which the correlation between the bands is zero. Figure 2.13 is an illustration of such a rotation.

The PCA technique is accomplished through the Karhunen-Loeve transformation (Santisteban and Munoz, 1977). The transformation is a linear transformation which generates a new set of coordinates by weighting the original spectral bands. The first principal component maximizes the variance of the original data into a new band which is

a linear combination of measurements in the original spectral bands. The second and subsequent principal components each maximize the remaining variance in the data. The transformation is accomplished through Equation 2.9. The linear operator,  $G$ , is defined as the transposed matrix of eigenvalues of the scene covariance matrix. The decorrelation of the data is described by Equation 2.10. The new covariance matrix is a diagonal matrix of the eigenvalues of the original covariance matrix.

$$\text{Equation 2.9} \quad \bar{P}_i = G\bar{S}_i$$

$\bar{P}_i$  = vector of principal component values of  $i^{\text{th}}$  pixel

$G$  = linear transformation

$\bar{S}_i$  = spectrum of  $i^{\text{th}}$  pixel

$$\text{Equation 2.10} \quad C' = GCG'$$

$C$  = scene covariance matrix

$G$  = transposed matrix of eigenvectors of  $C$

$C'$  = diagonal matrix of eigenvalues of  $C$

The first principal component represents the largest data variance within the scene. The successive components contain less and less of the scene variance. As a result, the first few principal components will contain most of the information in the original data. The last few components will contain mostly noise. This type of transformation has been considered a data compression technique because it concentrates the original information contained in hundreds of bands of spectral data into 10 or 20 principal component bands.

Once the linear transformation matrix,  $G$ , has been generated, it can be applied quickly and efficiently to additional data sets through simple matrix multiplication. This efficiency makes PCA attractive from an operational perspective. Unfortunately, the transformation matrix is sensitive to changes in scene content. Another drawback of PCA

is that the quantification of what each principal component physically represents is difficult since the transformation is based strictly on variability of the data set.

## **2. Spectral Angle Mapper**

The spectral angle mapper (SAM) is a spectrum matching algorithm that labels scene elements based on their similarity to a particular target spectrum (Kruse, et al, 1993). The SAM algorithm chosen for this analysis is implemented in the Environment for the Visualization of Images (ENVI) data analysis software package. The algorithm compares the spectral data from an image to selected target or 'end member' spectra and produces a set of images in which intensity represents the similarity to each target spectrum. The algorithm also produces a classification image showing the best match for each pixel in a scene.

The SAM determines the similarity between spectra by calculating the "spectral angle" between them. It was developed for spectral data in the visible, NIR, and SWIR regions of the electromagnetic spectrum. The spectra are treated as vectors in a space with dimensionality equal to the number of spectral bands. Figure 2.14 illustrates the concept of "spectral angle" for a two-dimensional case. Each measurement is represented as a vector from the origin to a point plotted in band intensity space. A vector terminating close to the origin represents a point with little illumination while a vector terminating far from the origin represents a brightly illuminated point. In either case, the direction of the vector is characteristic of the material's spectral properties.

The SAM uses the angular separation between a target spectrum and a reference spectral vector to determine spectral similarity (Schowengerdt, 1994). This allows the SAM to perform equally well regardless of illumination and gain conditions. The angular separation between an unknown spectrum and the reference spectrum can be calculated by Equation 2.11.

Equation 2.11 
$$\alpha_i = \cos^{-1} \left( \frac{\bar{T} \cdot \bar{S}_i}{|\bar{T}| |\bar{S}_i|} \right)$$

$\alpha_i$  = spectral angle of  $i^{th}$  pixel

$\bar{T}$  = reference spectrum

$\bar{S}_i$  = spectrum of  $i^{th}$  pixel

The output of the SAM is a new image set with the number of images equal to the number of target reference spectra. Each image consists of the spectral angle separation between the pixels in the scene and a particular target spectral vector. Bright areas indicate close matches. The use of a minimum separation angle can be employed to classify spectra as a match to a particular reference spectra.

The SAM algorithm can be applied directly to radiance measurements in the reflective region of the electromagnetic spectrum. In the thermal infrared region, the data must be converted to emissivity or apparent emissivity prior to the application of the SAM algorithm. This is because the effects of temperature variations are not simply additive as in the case of illumination variations in visible, NIR, and SWIR data.

### 3. Spectral Matched Filter

The spectral matched filter (SMF) is another spectral matching technique. It was adapted from matched filter techniques used in the spatial and temporal domains. The SMF technique used for this analysis was implemented in the ENVI data analysis software package. As described by Billingsley, et al (1995), the SMF algorithm is a two-stage process. The first step characterizes the dominant spectral components in the scene and 'whitens' them. The second step is a search for a match to a spectral reference vector in the residual subspace.

The SMF uses scene spectral statistics and a spectral reference vector to calculate weighting factors which combine the appropriate spectral bands to attain the highest signal-to-clutter ratio (Stocker, et al, 1990). The SMF algorithm is implemented through Equation 2.12.

Equation 2.12  $y_i = \bar{b}^t C^{-1} \bar{x}_i$

$y_i$  = filtered intensity of  $i^{th}$  pixel

$\bar{b}$  = spectral reference vector

$C$  = background spectral covariance matrix

$\bar{x}_i$  = spectrum of  $i^{th}$  pixel

The SMF can also be viewed as a weighted combination of principal components as described by Stocker, et al (1990). This interpretation is presented in Figures 2.15 - 2.17. Figure 2.15 illustrates a Gaussian clutter density and an additive spectral signal,  $\bar{b}$ . Correlation between the two spectral bands causes the clutter density to be elongated along a major axis. Projections of the data beside each waveband axis demonstrate that the signal-to-clutter ratio in either band is not sufficient to detect the signal. A principal component transformation results in Figure 2.16. The transformation has enabled the spectral signal,  $\bar{b}$ , to become distinct from the clutter in the second principal component. The SMF gains a further increase in the signal-to-clutter ratio by forming the optimum weighted combination of principal components using a weight vector based on the reference spectrum. The result is illustrated in Figure 2.17.

The output of the SMF is a two-dimensional spatial image. Each point in the image is the result of an optimum weighted combination of spectral band measurements. High intensity pixels within the filtered image indicate the presence of the reference spectra. A thresholding algorithm can be used to identify likely targets.



### **III. THE DEVELOPMENT OF THE SPATIALLY ENHANCED BROADBAND ARRAY SPECTROGRAPH SYSTEM (SEBASS)**

Thermal remote sensing development has followed a progression toward higher spectral resolution in the drive toward identifying materials based on their emissive spectra. The thermal infrared multispectral scanner (TIMS) demonstrated that contiguous, moderately narrow bands could be used to discriminate between various minerals based on their spectral features (Richards, 1993). Bongiovi, et al (1995) demonstrated that hyperspectral LWIR measurements could detect fine spectral features and identify specific materials based on their spectral characteristics using data from Aerospace Corporation's Broadband Array Spectrograph System (BASS). BASS was a non-imaging spectrograph that operated in the MWIR and LWIR regions of the electromagnetic spectrum. The Spatially Enhanced Broadband Array Spectrograph System (SEBASS) was developed as a follow-on to BASS. SEBASS is an imaging hyperspectral sensor that was "... designed to explore the utility of infrared hyperspectral sensors for remotely identifying solids, liquids, gases, and chemical vapors in the 2.5 to 14.0  $\mu\text{m}$  'chemical fingerprint' spectral region." (Hackwell, et al, 1996)

#### **A. THERMAL INFRARED MAPPING SCANNER (TIMS)**

The Thermal Infrared Mapping Scanner (TIMS) was developed for remote sensing of non-renewable resources. TIMS is a six band, dispersive grating scanner developed by Daedalus Enterprises for the Jet Propulsion Laboratory (Richards, 1993). The spectral resolution of TIMS was designed to measure the depth and position of the reststrahlen band and other silicate spectral features useful in identifying rock and soil types. The spectral bandpass characteristics of TIMS are listed in Table 3.1.

Band Number	Spectral Bands ( $\mu\text{m}$ )
1	8.2 - 8.6
2	8.6 - 9.0
3	9.0 - 9.4
4	9.5 - 10.2
5	10.2 - 11.2
6	11.2 - 12.2

Table 3.1. TIMS Spectral Bands. From Richards, 1993.

Data from TIMS have demonstrated the ability of thermal spectral data to conduct terrain categorization and materials classification (Richards, 1993). In order to remove the temperature dependence of LWIR emitted radiation and focus on the emissivity characteristics of the materials within the TIMS field-of-view, a decorrelation stretch is often applied to the TIMS data. A decorrelation stretch is based on the principal components transformation. The processing technique "...causes the spectral differences between surface units to be displayed as color differences, while most of the temperature variation is displayed as intensity differences." (Kahle and Goetz, 1983)

An analysis of TIMS data collected over the Cuprite Mining District of Nevada by Kahle and Goetz (1983) is an excellent example of material classification using TIMS data. Figure 3.1 is a three-band color composite of the Cuprite Mining District from Kahle and Goetz. The discrimination between materials is based primarily on the free-silica content of the ground materials and its effect on their emissive spectra. Silicified rocks appear as bright orange. Clay-rich minerals are magenta and carbonate rocks have a green-blue tone.

## **B. THE BROADBAND ARRAY SPECTROGRAPH SYSTEM (BASS)**

BASS is a dispersive hyperspectral instrument capable of producing a complete 116-band spectrum from 2.5-14.0  $\mu\text{m}$  every 5 milliseconds (Bongiovi, Hackwell, and Hayhurst, 1995). The data generated by BASS demonstrated the utility of infrared spectral data and prompted the development of an imaging instrument based on the same design.

## 1. Instrument Design

BASS employs two spectrometers to cover the MWIR and LWIR regions of the electromagnetic spectrum (Bongiovi, Hackwell, and Hayhurst, 1995). The MWIR channel records radiation from 2.5 to 6.5  $\mu\text{m}$ . The LWIR channel records radiation from 6.5 to 14.0  $\mu\text{m}$ . Each channel employs a spherical-faced prism and a mirror to disperse and reimage the incoming radiation onto separate 58-element linear array photoconductors. The arrays are doped silicon 'blocked impurity band' photoconductors which have a high quantum efficiency and low noise when operated at temperatures below 10K. The optical layout of BASS is presented in Figure 3.2. Signals from the detectors are digitized and stored by a Macintosh II personal computer.

BASS has been flown aboard a DH-6 "Twin Otter" aircraft. The BASS cryostat is mounted on a platform that can be steered in the roll direction of the aircraft. A telescope with a focal length of one meter focuses the incoming radiation on BASS's field optics. The field-of-view of the telescope is one milliradian. From operating altitudes of 700 to 3000 ft, the ground sample distance (GSD) of BASS is 0.7 to 3.0 ft. Three cameras are mounted on the "Twin Otter" to assist the operator in steering BASS and to aid in post-mission analysis of collected spectra. One camera is a wide field-of-view color camera pointed forward at a 45° angle. A MWIR camera is located on the bottom the platform and provides a 8° field-of-view. A black and white camera with a 5° field-of-view is bore sighted with BASS through a beam splitter in the external telescope. Figure 3.3 is a schematic of the BASS "Twin Otter" configuration.

## 2. SMO Utility

An analysis of BASS hyperspectral data by Bongiovi, et al (1995) demonstrated the potential of LWIR data to locate and identify military targets. BASS was used to collect overhead LWIR hyperspectral data on several military vehicles in October of 1994. Data from the BASS collection was used to derive spectral indices for the military

vehicles. These indices were then applied to other data sets to determine BASS's ability to detect target vehicles within a scene.

Figure 3.4 shows a row of military vehicles that were used to derive the spectral templates. BASS data collected over this scene was converted to surface brightness temperatures after atmospheric compensation. The converted data was then used to derive four spectral templates: sand, limestone, vehicle 1, and vehicle 2. The two vehicle templates were representative of different types of paint observed on the vehicles. These templates are shown in Figure 3.5. The application of the spectral templates to new data sets results in response plots similar to Figures 3.6 and 3.7. Figure 3.6 depicts the response plots resulting from application of the spectral templates to the initial training scene. The arrows indicate a response to the presence of military vehicles. The application of the spectral templates to other data sets demonstrated an ability to locate target vehicles even when partially concealed by vegetation. Figure 3.7 is the response function of a tank concealed in trees.

### **C. THE SPATIALLY ENHANCED BROADBAND ARRAY SPECTROGRAPH SYSTEM**

The success of BASS led to the development of an imaging infrared instrument based on BASS's dispersive, two-channel design. Aerospace developed the follow-on instrument, SEBASS, with internal funds as a phenomenology research tool to further LWIR hyperspectral remote sensing research.

#### **1. Instrument Design**

The SEBASS optical layout is similar to that of BASS and is depicted in Figure 3.8. Radiation entering SEBASS is split into two spectrographs: one for MWIR (2.9-5.2  $\mu\text{m}$ ) and one for LWIR (7.8-13.4  $\mu\text{m}$ ) (Hackwell, et al, 1996). Each spectrograph focuses a dispersed image of the slit onto a two-dimensional array. The arrays are 128 by 128 element impurity band conduction arrays. One dimension of the array is spectral and the other is spatial. The second spatial dimension required for imaging is provided by the

movement of the sensor. Figure 3.9 displays this 'pushbroom' imaging concept. The figure also shows the spectral and spatial dimensions of SEBASS data.

The spectral resolution of SEBASS varies across the array due to the characteristics of longwave infrared radiation and the dispersion characteristics of the prisms. Figure 3.10 is a graph of the spectral resolution of the LWIR channel. SEBASS can achieve a resolution as fine as .035  $\mu\text{m}$  at the long wavelength edge of the array.

SEBASS's data system collects, digitizes and stores signals from the two focal planes. The focal planes operate at data rates of up to 100 frames per second and are digitized by 14-bit analog-to-digital converters. Data from each pass is stored in 128 megabytes of cache RAM until after a pass is completed. It is then dumped to a hard disk for later processing. The system is built around a Sun Sparc 20 host computer. SEBASS can be mounted aboard the Twin Otter aircraft in a flight configuration similar to that used during BASS flight experiments. SEBASS can employ two external telescopes which provide either a 1 milliradian or 3 milliradian field-of-view.

## 2. Data Format and Use

Prior to processing, raw SEBASS sensor data must be spectrally and radiometrically calibrated. Spectral calibration is the process of obtaining an accurate map of the wavelength band collected by each pixel in the array. Radiometric calibration is the process of converting instrument digital data to absolute radiance values.

Data produced by SEBASS are stored according to the following convention:

*DN(spectral, spatial, frame)*

*DN* = digital number

*spectral* = wavelength dimension (see Figure 3.9)

*spatial* = slit position dimension (see Figure 3.9)

*frame* = ground path dimension (see Figure 3.9)

*a. Spectral Calibration*

The wavelength calibration process for SEBASS's LWIR channel is performed using a set of polymer films with known absorption feature (Bongiovi, 1996). The transmittance spectrum of the filter is presented as Figure 3.11. A wavelength map for the array is created by locating the filter's prominent absorption features as they are imaged on the focal plane.

The polymer film is placed over the SEBASS aperture as the instrument images a blackbody at a known temperature. The blackbody is then imaged without the filter. The ratio of these two images is the transmittance spectrum for the filter. Figure 3.12 is an example of the spectrum of the filter as measured by SEBASS. The location of the absorption features on the array are used to generate a polynomial function which describes the wavelength for each pixel. The algorithm which generates the polynomial function relies on the fact that the dispersion of SEBASS's NaCl prism is a function of the square of wavelength and that the spatial curvature of the slit is a second order function. The final fit for Aerospace's LWIR channel wavelength calibration is presented in Equation 3.1.

Equation 3.1       $\lambda^2(x, y) = a_0(y) + a_1(y)x + a_2(y)x^2$        $[\mu m^2]$

$$a_0(y) = 57.0758 - 0.0216030y + 0.000100471y^2$$
$$a_1(y) = 1.03258 + 1.88537 \times 10^{-5}y + 9.25211 \times 10^{-8}y^2$$
$$a_2(y) = -0.000100671$$

$x$  = spectral dimension (see Figure 3.8)  
 $y$  = slit position dimension (see Figure 3.8)

These wavelength calibration equations generate a wavelength map for the LWIR channel. Due to the curvature of SEBASS's slit and dispersion through the prism, the center wavelength is not constant across the array. The final step in spectral calibration is the removal of this spectral curvature. This is accomplished through a

linear interpolation in which the wavelength map of SEBASS is interpolated to match the center column of the array.

**b. Radiometric Calibration**

The process for converting instrument digital number to actual radiance values is accomplished through the use of on-board blackbodies. During a flight, SEBASS collects data from two blackbodies which are at different temperatures. The calibration sources radiate a known amount of energy and are used to determine parameters for the radiometric calibration of SEBASS data.

The focal plane array employed in SEBASS exhibited a non-linear response function. To account for this effect, B. Johnson (1996) developed a non-linear calibration formula which is presented as Equation 3.2. The calibration files collected from the blackbodies are used to generate a series of coefficients ( $BG, \sigma, \tau$ ) which convert the instrument's digital values into measured radiance,  $L_m$ . The quantities  $\sigma$  and  $\tau$  are fixed parameters for the SEBASS instrument during a collection exercise. The  $BG$  parameter represents the background system noise which may vary from flight to flight.

Equation 3.2

$$\frac{DN}{Coadds} = \sigma(L_m + BG) + \tau(L_m + BG)^2$$

$L_m$  = measured radiance [ $\mu W/cm^2 \mu m sr$ ]

$BG$  = background radiance [ $\mu W/cm^2 \mu m sr$ ]

$\sigma, \tau$  = gain coefficients

$DN$  = instrument digital number

$Coadds$  = number of co-added measurements

The initial configuration of SEBASS exhibited a small degree of thermal drift. To account for this effect, the background radiance term,  $BG$ , for a particular data set is adjusted by interpolating between the two closest calibration measurements. This interpolation is accomplished through Equation 3.3.

Equation 3.3 
$$BG(t) = BG_1 + (BG_2 - BG_1) \left[ \frac{1 - e^{(-\alpha(t-t_1))}}{1 - e^{(-\alpha(t_2-t_1))}} \right]$$

$BG$  = background radiance [ $\mu W/cm^2 \mu m sr$ ]

$t$  = time [sec]

$\alpha = 0.038$

#### **IV. EXERCISE WESTERN RAINBOW**

The MASINT Hyperspectral Study (MHS) was initiated in 1993 to address the utility of hyperspectral imaging systems. The MHS program conducted a series of experiments focusing on the ability of hyperspectral imaging technology to address the following intelligence areas:

- Support to Military Operations (SMO)
- Nuclear Proliferation (MHS: Interim Progress Report, 1995)

The MHS program adopted a standardized experimental method for its hyperspectral collection exercises. The MHS exercises combine realistic, military scenarios with a succession of laboratory measurements, ground field measurements, and airborne collections.

During 1994 and 1995, the MHS program conducted two experiments to study the SMO capabilities of hyperspectral imagery. In September 1994, Exercise SOUTHERN RAINBOW was conducted at the Chicken Little facility at Eglin Air Force Base. A follow-on exercise, WESTERN RAINBOW, was conducted in October 1995 at the Yuma Proving Ground in Yuma, Arizona (MHS: Interim Progress Report, 1995). The primary objective of WESTERN RAINBOW was "... to measure the multi/hyperspectral and radar signatures of ground threat vehicles and backgrounds under various conditions of concealment, countermeasures, and lighting." (Operations Order, 1995)

##### **A. EXERCISE SCENARIO**

In order to provide a realistic environment for target detection and classification, a scripted scenario was used to guide the selection, placement, and camouflage of military targets used in WESTERN RAINBOW. Personnel from the Joint Camouflage, Concealment, and Deception (JCCD) group of the Office of the Secretary of Defense drafted the exercise scenario and directed the collection site preparations. The scenario

defined the placement of tactical military vehicles as well as their camouflage and concealment schemes. The JCCD efforts ensured that the deception schemes used current camouflage, concealment, and deception (CCD) equipment and techniques.

The scripted scenario for WESTERN RAINBOW described a decimated orange force defending critical mobile targets (CMTs) from a southward moving blue force (WESTERN RAINBOW: CCD Report, 1996). Two sites with multiple levels of CCD were prepared. A tank and artillery site (referred to as the JCCD site) was established to represent a forward defense position. A second site (referred to as the Arroyo site) represented the orange forces' CMTs.

The JCCD site consisted of four Soviet tanks and a mobile artillery piece. In the scenario, this site was established with the mission of defending the critical targets from the southward moving blue forces. Nine decoys of varying fidelity were placed just north of the five defending vehicles. These decoys were designed to have a greater signature visibility than the real targets in order to reduce the chance of effective aerial reconnaissance or targeting by the blue forces.

The Arroyo site represented the orange forces theater ballistic missile (TBM) assets and their associated close-in protection. Three Soviet tanks and a Soviet armored troop carrier were deployed to protect the two TBMs. The tactical vehicles were placed in defensive positions around the TBMs.

## **B. COLLECTION SITES**

The SMO portion of WESTERN RAINBOW consisted of three collection sites. Each collection site served a specific purpose within the overall collection plan. The Malpai target site served as an initial target and background signature collection site. This site was utilized for spectral ground truth collection and signature characterization. The JCCD tank and artillery site and Arroyo TBM site were established for realistic target detection analysis.

## 1. Malpai Site

The Malpai site consisted of an array of threat vehicles, camouflage schemes, decoys, and calibration panels. The layout of the targets within the Malpai site is depicted in Figure 4.1 (Boisjolie, 1996). The array was situated on a background of 'desert pavement' which consisted of small pebbles coated with a desert varnish. Vegetation was sparse and located in two washes that ran alongside the collection site. The site was established on 19 October and maintained for five days. The array was modified periodically by the addition of camouflage and the removal or addition of various tactical vehicles. These changes were documented for each collection mission.

An array of five Soviet T-72 tanks was centered within the target site. The tanks were oriented in various directions to allow for multiple sun-angle geometries. Two US tankers were placed to the west of the T-72 array. In order to provide data for thermal inertia and temperature analysis, one tank was filled with water while the other was left empty. Two sets of reflective calibration panels were placed within the array for the calibration of visible and NIR sensors. In the north part of the site, a series of JCCD camouflage treatments and decoys were placed. These included US and Soviet color panels, a special IR appliqué, prototype camouflage materials, and helicopter decoys. At the south end of the site, a series of threat vehicles were placed in the open. A general list of targets within the Malpai site is presented in Table 4.1.

Target	Bumper #
T-72	199
T-72	934
T-72	922
T-72	910
T-72	933
2S3	5521
T-80 surrogate	001
T-80 surrogate	002
LAV (green)	5217
LAV (desert camouflage)	82
M series 5000 gal tanker (empty)	C138
M series 5000 gal tanker (filled with water)	C243
George	
Calibration panels	
Calibration panels	
Calibration pool (filled with water)	
Apache helicopter decoy (2 1/2 dimension mural)	
OH-58 helicopter inflatable decoy	
PRC net	
Bomb crater decoy	
DOD LCSS arctic net	
US panel of colors	
Soviet panel of colors	
Prototype fox hole camouflage	
Special IR appliqué	
Prototype ULCAN	
Prototype tank mat	

Table 4.1. Malpai Target Descriptions. After Boisjolie, 1996.

## 2. JCCD Tank and Artillery Site

The JCCD tank and artillery site employed multiple threat vehicles and decoys with varying levels of CCD. The site consisted of three rows of targets which were placed within washes running from the southwest to the northeast. The layout of the JCCD site is depicted in Figure 4.2 (Boisjolie, 1996). The washes contained sparse vegetation consisting of small bushes and trees. The JCCD site was maintained from 19 October through 24 October.

Two of the target lines contained decoys which varied in quality from high fidelity, specially constructed mock-ups to field expedient decoys constructed from available scraps found within the target site. Additional deception devices such as corner

reflectors, heating pots, and fake tank tracks were used to enhance the decoys. A full description of each decoy is included in Table 4.2.

Target	Label in Figure 4.3	Additional Description
M-19 aluminum matting tank decoy	Decoy 1, Line 1	No camouflage
Sheet metal tank decoy	Decoy 2, Line 1	Partially covered by LCSS desert camouflage netting
M-19 aluminum matting tank decoy	Decoy 3, Line 1	Covered with AFCENT camouflage netting
T-72 mural	Decoy 4, Line 1	LCSS army woodland camouflage netting placed beside mural, heated thermal reflector
M-1 turret mural	Decoy 5, Line 1	LCSS army woodland camouflage netting underneath, fresh cut vegetation
2S3 sled decoy	Decoy 1, Line 2	Covered with AF ULCAN desert camouflage netting, propane heaters
2S3 sled decoy	Decoy 2, Line 2	Covered with LCSS army woodland camouflage netting
Scrap metal tank decoy	Decoy 3, Line 2	Covered with West German woodland camouflage netting, propane heaters
M-1 mural	Decoy 4, Line 2	East German camouflage netting placed in front

Table 4.2. JCCD Decoy Line Descriptions. After Boisjolie, 1996.

The real threat vehicles were deployed within the southern wash. These vehicles were camouflaged and placed in both full and partial defilade. The full dress for each vehicle is outlined in Table 4.3.

Target	Bumper #	Label in Figure 4.3	Additional Description
2S3 mobile artillery	5521	Artillery	Camouflage with cut live and dead vegetation
T-72	910	Tank 4	Camouflage with live & dead vegetation and dirt
T-72	199	Tank 3	Full defilade, covered with sandbags and LCSS desert camouflage netting
T-72	934	Tank 2	Camouflage with dead vegetation and soil
T-72	933	Tank 1	Partial defilade, UK desert camouflage netting, UK thermal blanket

Table 4.3. JCCD Vehicle Target Line Description. After Boisjolie, 1996.

### 3. Arroyo Site TBM Site

The Arroyo site was a simulation of a TBM site and its associated defensive weapons. The site had a moderate amount of vegetation. The Arroyo site was established on 21 October and maintained until 23 October. The layout for the Arroyo site is presented in Figure 4.3 (Boisjolie, 1996). The targets included two TBMs, three defensive tanks, and a personnel carrier. All of the targets within the Arroyo utilized some kind of camouflage treatment. The complete description of the CCD treatments for each target are listed in Table 4.4.

Target	Bumper #	Label in Figure 4.4	Additional Description
T-80 surrogate	002	Tank 1	AF woodland ULCAN camouflage netting
T-80 surrogate	001	Tank 2	WSMR just-in-time netting
T-72	922	Tank 3	Partial defilade, Israeli ULCAN netting
MT-LB	PMI-904	Tank 4	Partial defilade, SSSC space frame
TBM 1	TBM 1	TBM 1	Canvas, LCSS tri-color desert camouflage netting
TBM 2	TBM 2	TBM 2	Woodland Eglin ULCAN netting

Table 4.4. Arroyo Target Description. After Boisjolie, 1996.

### C. GROUND COLLECTION EQUIPMENT

The ground sensors employed in WESTERN RAINBOW provided an extensive data set of background and target spectra. The complete ground sensor suite is listed in Table 4.5. As indicated in the table, the electromagnetic spectrum from visible to LWIR was covered. Instrumentation capable of collecting MWIR and LWIR data during the exercise included the Johns Hopkins University (JHU) micro fourier transform imaging radiometer (uFTIR) and the Environmental Institute of Michigan's (ERIM) Bomem MB-100 FTIR (Operations Order, 1995). In addition, JHU performed laboratory MWIR and LWIR measurements of material samples with a Nicolet FTIR spectrometer and a Beckman grating spectrometer.

Instrument	Spectral Range ( $\mu\text{m}$ )	Spectral Resolution ( $\text{cm}^{-1}$ )
GER Mark IV	0.35-2.5 (875 bands)	0.005
JHU micro-FTIR	3-5.5, 7.5-14	6
Bomem MB-100 FTIR	3-15 (128 bands)	1-4
Nicolet	2-15	4
Beckman	.4-2.5	2nm visible, 10 nm SWIR

Table 4.5. WESTERN RAINBOW Ground Sensors. After Operations Order, 1995.

### D. AIRBORNE COLLECTION EQUIPMENT

The airborne collection assets involved in WESTERN RAINBOW covered the electromagnetic spectrum from visible to LWIR and included both multispectral and hyperspectral sensors. The sensors are listed in Table 4.6. The assets capable of LWIR remote sensing included Aerospace Corporation's SEBASS and the EG&G's Daedalus multispectral scanner (Daedalus MSS) (Operations Order, 1995). The Daedalus MSS is a multispectral scanner with 12 bands. One channel can be configured for MWIR imaging and one channel can be configured for LWIR imaging.

Instrument	Spectral Range( $\mu\text{m}$ )	Number of Spectral Bands	Ground Sample Distance (feet)
HYDICE	.4-2.5	210	2.5 - 10
Daedalus MSS	.4 - 12	12 (8 vis-NIR, 2 SWIR, 1 MWIR, 1 LWIR)	0.5
SEBASS	7-14	128	1-3

Table 4.6. WESTERN RAINBOW Airborne Sensors. After Operations Order, 1995.

## **V. EXPERIMENT OBSERVATIONS**

The WESTERN RAINBOW experiment was conducted from 18 - 24 October, 1995 at the United States Army Proving Ground in Yuma, Arizona. Airborne SEBASS data collection flights over the SMO target areas were conducted from 20 - 24 October. The site preparations, ground truth observations, and airborne sensor operations were coordinated to ensure that the target areas were well documented for post-exercise analysis. This chapter presents the author's observations of the exercise. The chapter begins with a description of the Yuma, Arizona collection environment. The second section describes the performance of the SEBASS sensor. The final section describes the hyperspectral data collected by SEBASS and the procedures used to prepare it for analysis.

### **A. YUMA PROVING GROUND OBSERVATIONS**

The Yuma Proving Ground was an excellent environment for the exercise. The area has predictable weather conditions and low humidity. The airspace over the site is restricted. This allowed sensor aircraft to maneuver in the absence of commercial traffic. The average elevation was about 850 feet.

#### **1. Collection Sites**

The isolation of the exercise area provided an environment in which the collection sites could be established and camouflaged without interference. The desert background consisted of sand, rock fragments, and small brush. The rock fragments were darkened with a distinctive desert varnish. Figure 5.1 is a picture of the JCCD area displaying the general background of the Yuma Proving Ground.

The collection sites were prepared by the JCCD personnel according to the scenario described in Chapter IV, Exercise WESTERN RAINBOW. The camouflage and

concealment preparations were realistic and simulated actual operating conditions. The site preparations and changes were well documented and photographed.

Ground traffic in the collection sites was kept to a minimum with the exception of the Malpai site which was used extensively for ground sensor collections. In addition, traffic in the JCCD site was limited to ground truth personnel in order to provide a "blind test" of sensor performance.

## **2. Weather Conditions**

The weather conditions were consistent throughout the exercise and were characterized by hot, dry days. The surface temperature during the exercise ranged from lows of about 20° C at night to as high as 54° C during the day. Wind conditions were generally good throughout the exercise. Only one day of operations had to be canceled because of low visibility caused by wind. Meteorological data such as wind speed, surface temperature, air temperature, and humidity were collected by ground truth personnel.

## **B. SEBASS PERFORMANCE**

The Aerospace SEBASS instrument was flown aboard a Twin Otter aircraft in a configuration similar to Figure 3.3. The author observed both collection and post-mission processing of SEBASS data. The SEBASS flights were flown at 0600, 1000, and 1400 local time on various days during the exercise. Each flight consisted of several runs over the various collection sites. Coordination between the aircraft and on-going ground operations was accomplished through daily briefings and radio contact.

### **1. Flight Operations**

The SEBASS flights over the Arroyo, JCCD, and Malpai collection sites were performed from an altitude of 2,500 feet. This altitude produced images with a ground pixel size of 2.5 feet. The swath width of each data set was approximately 320 feet.

The small swath width of SEBASS contributed to difficulties in getting a good image of all of the targets within a collection site. SEBASS was installed aboard the aircraft without roll stabilization. As a result, wind gusts caused targets to shift in and out of the instrument's field-of-view as the aircraft rolled. In addition, the lack of ground markers and on-board positioning equipment made it very difficult for the pilot to fly directly over a particular set of targets and keep them within SEBASS's small field-of-view. The additional cameras aboard the aircraft and the sensor operator's ability to steer the instrument partially alleviated this problem. White panel markers and ground-to-air voice communications were used on later flights to help steer the pilot over a particular target area.

## 2. Sensor Performance

Exercise WESTEN RAINBOW was the first operational use of SEBASS. The data collected served as the first image data recorded by the instrument outside of the laboratory. The instrument performed extremely well throughout the exercise and maintained a noise-equivalent spectral radiance (NESR)  $1.2 \times 10^{-6} \text{ W/cm}^2\mu\text{m sr}$ .

Several artifacts were noticed in the collected data. Intensely bright objects created a ghost image of themselves approximately ten lines ahead of their actual location. Figure 5.2 shows an example of this artifact. Each T-72 in the figure has a ghost image offset by several scan lines. The problem was caused by the reflection and diffraction of incoming radiation as it interacted with the edge of the imaging slit. The ultimate effect of the ghost problem was a mixing of scene radiance from each line with the line ten scans ahead of it. This artifact did not have a significant effect on the results of this study. A second problem identified during the exercise was the thermal drift mentioned in Chapter III, Section C. The thermal drift was initially detected and characterized using data collected during WESTERN RAINBOW. Finally, the gain of one of the four amplifiers in SEBASS varied from flight to flight. Although these problems have since been corrected in the instrument, they affect all of the data collected during WESTERN RAINBOW to some degree.

### C. GROUND TRUTH OBSERVATIONS

The collection of ground truth target and background spectra was accomplished by ERIM and John Hopkins University personnel using the equipment listed in Table 4.5. The ERIM collection operations were performed using an elevated platform. The John Hopkins University collections were performed using the micro-FTIR, Nicolet, and Beckman spectrometers.

The John Hopkins University micro-FTIR employed in the field recorded measurements in radiance values. These measurements were converted to apparent emissivity for spectral analysis of the SEBASS data. The conversion process began with the estimation of the surface temperature of each sample. The sample surface temperature was estimated by calculating the brightness temperature within each wavelength band. Brightness temperature was calculated by inverting Equation 2.1 and setting the surface temperature equal to the maximum brightness temperature measured within the bandwidth of the instrument. This estimation is based on the assumption that the emissivity maximum occurs somewhere between 8.0 and 13.0  $\mu\text{m}$  and is close to 1.0. The apparent emissivity of the material was calculated through application of Equation 2.2.

Ground truth spectra were available on several targets and camouflage schemes. The available spectra and their source are listed in Table 5.1 and depicted graphically in Figures 5.3 and 5.4. For those materials for which ground truth spectra were not available, the author sampled spectra directly from SEBASS images of the Malpai training scene. The Malpai-derived spectra are listed in Table 5.2. Figure 5.5 depicts some examples of spectra extracted from SEBASS data.

Target	Source	Designator	Additional Description
Desert Varnish	JHU	MAL1048_JHU	
Sand Beneath Desert Varnish	JHU	DUST1110_JHU	
Desert Panorama	JHU	DSRT1606_JHU	
T-72 Tank	JHU	T1326_JHU	
T-80 Surrogate	JHU	MBT1152_JHU	
Woodland Camouflage	JHU	WOOD1347_JHU	British/German
LCSS Desert Camouflage	JHU	LC1531_JHU	Desert Tricolor
LCDD Woodland Camouflage	JHU	LC1322_JHU	Woodland Pattern
Tan Camouflage	JHU	TAN1305_JHU	AF Desert Ullan

Table 5.1. Ground Truth Spectra from WESTERN RAINBOW.

Target	Source
Desert Varnish	SEBASS - 20oct95_1000/mal5.dat
Disturbed Desert Varnish	SEBASS - 20oct95_1000/mal5.dat
Tank Tracks in Desert Varnish	SEBASS - 20oct95_1000/mal5.dat
Vegetation	SEBASS - 20oct95_1000/mal5.dat
Prototype Foxhole Cover	SEBASS - 20oct95_1000/mal5.dat
IR Applique	SEBASS - 20oct95_1000/mal5.dat

Table 5.2. Target Spectra Derived from SEBASS Data Collected Over Malpai Site.

#### D. HYPERSPECTRAL OBSERVATIONS

Data from WESTERN RAINBOW was supplied to the author by the Office of Research and Development, Aerospace Corporation, and John Hopkins University. The amount of image data from SEBASS was extensive. Each SEBASS image is approximately 140 megabytes. As many as 14 images were collected during a flight. The

author screened the SEBASS data set and selected particular collection flights for processing and analysis.

## 1. Hyperspectral Image Data

Data from the Malpai, Arroyo, and JCCD sites were analyzed to determine if thermal spectral data would provide an ability to detect military targets under various degrees of concealment. The Malpai site was used as an initial training scene. It served as a source of target spectra and as a tool with which to select how the principal components transformation would be applied to later data sets. The JCCD and Arroyo scenes were then analyzed to determine if the various targets could be detected.

The selection of which Arroyo and JCCD scenes to analyze was driven by the requirement to maximize the possibility of an image set containing all of the targets within a collection site. The data were also screened to determine which data sets were not adversely affected by the amplifier gain problem. The images listed in Table 5.3 were selected for analysis.

Date	Time	Collection Site	Data Set Name
20-Oct	1000	Malpai	20oct95_1000/mal5.dat
23-Oct	1000	JCCD - Line 1	23oct95_1000/jccd3.dat
23-Oct	1000	JCCD - Line 2	23oct95_1000/jccd1.dat
23-Oct	1000	JCCD - Vehicle Target Line	23oct95_1000/jccd4.dat
23-Oct	1000	Arroyo	23oct95_1000/arroyo5.dat

Table 5.3. SEBASS Data Sets Selected for Analysis.

## 2. Data Preparation

The raw SEBASS data were processed into several standard data formats. The steps involved in the data preparation process are depicted in Figure 5.6.

**a. *Spectral and Radiometric Calibration***

The spectral and radiometric calibration procedures described in Chapter III, Section C were applied to the raw data to convert the data into appropriate units. The spectral curvature of the data was removed in this step through linear interpolation.

The effect of the varying gain of the fourth amplifier was mitigated through a procedure proposed by B. Johnson (1996) of Aerospace Corporation. The output of the fourth amplifier was compared to that of its adjacent amplifier outputs. A multiplication factor was then derived to bring the output of the errant amplifier down to the level of the other amplifiers. This procedure was based on the assumption that the gain of the fourth amplifier was constant across the focal plane array and the taps from the array were staggered enough to allow noise and material spectral characteristics to be averaged out. The SEBASS data was corrected for gain effects prior to radiometric calibration.

**b. *Generation of a Simulated, FLIR Image***

The radiometrically and spectrally calibrated data was then used to generate a simulated, single-band FLIR. This image was generated by averaging the radiance values measured in each band. It served as the standard image with which to compare the results from the analysis of the spectral data.

**c. *Atmospheric Correction***

Atmospheric correction was a two step process. The plastic ruler atmospheric correction procedure was used to determine relative atmospheric transmittance and upwelling radiance. These results were then scaled using Aerospace Corporation's ARTSPEC atmospheric model.

The plastic ruler algorithm outlined in Chapter II, Section B was modified slightly to account for the effects of employing the algorithm to a scene composed almost entirely of desert sand. The plastic ruler algorithm works well in areas with large amounts of vegetation because vegetation has a relatively flat emissive spectrum which is close to 1.0 throughout the LWIR region. Unfortunately, the desert environment in Yuma

has very sparse vegetation and most of the pixels within each image were desert sand. The emissive spectrum of desert sand has a characteristic reststrahlen minimum between 8.0 and 10.0  $\mu\text{m}$ . As the plastic ruler algorithm attempts to fit a line through the upper bound of a scatter plot composed almost entirely of sand measurements, it produces an artificially low transmittance in the 8.0 to 10.0  $\mu\text{m}$  region. To solve this problem, the author screened the data to exclude those pixels that exhibited a strong reststrahlen feature. This screening was performed by comparing the brightness temperature of each pixel between 9.45 and 10.0  $\mu\text{m}$  and excluding those pixels whose difference exceeded a particular threshold. The author also found that a large percentage of the desert vegetation exhibited a high degree of senescence. If a large percentage of senescent vegetation was used to generate the atmospheric parameters, the spectral characteristics of senescent vegetation described in Figure 2.7 could also adversely affect the results. To prevent this from occurring, pixels exhibiting a large degree of senescence were excluded by comparing the brightness temperature between 10.65 and 11.5  $\mu\text{m}$ .

The plastic ruler atmospheric compensation algorithm was implemented in IDL routines and is included as Appendix B. Figures 5.7 to 5.9 depict the results of the algorithm for SEBASS data collected over the Malpai site at 1000 local time on 20 October 1995. Figure 5.7 depicts a region of the scene and the two screening stages in which the pixels representing healthy vegetation are selected. The image sequence shows the pixels which satisfied the threshold check at each screening stage. Figure 5.8 depicts the results of the plastic ruler algorithm if no screening has taken place. The first graph is the transmittance spectrum of the atmosphere. The second graph is the upwelling radiance emitted by the atmosphere and received by the sensor. The effect of the sand pixels can be seen as a dip in atmospheric transmittance between 9.0 and 10.0  $\mu\text{m}$ . Figure 5.9 depicts the results of the plastic ruler algorithm after the input data has been screened to include only healthy vegetation.

The results of the plastic ruler algorithm were then compared with the results of Aerospace Corporation's ARTSPEC atmospheric model. The plastic ruler algorithm uses the collected data to generate relative atmospheric parameters. The ARTSPEC atmospheric model was used to convert the plastic ruler results into true

atmospheric transmittance and upwelling radiance. The comparison was performed using a series of routines written by Burke (1995). The routines were originally written for the BASS instrument and were modified by the author to work with SEBASS data. The routines alter the input parameters of the ARTSPEC model until the model's output atmospheric profile matches the shape of the results from the plastic ruler algorithm. Figure 5.10 depicts the results of the ARTSPEC fitting procedure on the atmospheric parameters generated from the Malpai data. It shows the ARTSPEC model results as a solid curve and the scaled plastic ruler algorithm results as a dotted curve.

The scaled atmospheric transmittance and upwelling radiance parameters were then applied to the calibrated data sets to remove the effects of the atmosphere. This was done by inverting Equation 2.8.

#### *d. Conversion to Apparent Emissivity*

The atmospherically corrected data were then converted into apparent emissivity using the same procedure that was applied to the JHU radiance data as described in Section C above. Figure 5.11 compares the apparent emissivity of desert varnish extracted from the Malpai data with JHU ground truth data collected from the same area. The two ground truth spectra represent the range of values observed in spectral measurements taken from several different desert varnish samples.

### **3. Hardware and Software Configuration**

The author used a UNIX-based, UltraSparc Sun workstation for data analysis. The three hyperspectral analysis algorithms were implemented in the ENVI hyperspectral data analysis software package. ENVI was used to perform the principal components analysis, spectral angle mapper analysis, and spectral matched filter analysis.



## **VI. DATA ANALYSIS**

The four data sets identified in Chapter V were analyzed using principal components analysis, the spectral angle mapper, and a spectral matched filter to determine whether thermal spectral data can be used to detect targets in a military scenario. The analysis process began with an intensive study of the Malpai training scene. This training data was used to establish a standard method of applying the hyperspectral analysis algorithms.

### **A. MALPAI COLLECTION SITE - 20 OCTOBER 1995**

The Malpai site consisted of an array of target vehicles and CCD materials. As described in Chapter IV, the Malpai targets were placed on a surface of desert varnish (see Figure 4.1). The background of desert varnish was substantially different from the targets placed on the site. As a result, all of the targets were easy to detect throughout the electromagnetic spectrum. This made the site an excellent location for ground truth data collection and sensor characterization.

#### **1. Data Processing**

The Malpai data selected for analysis were collected at 1000 local time on 20 October. The raw SEBASS data were prepared using the procedures outlined in Chapter V, Section D. The atmospheric parameters used to convert the radiance measured by SEBASS to source radiance at the ground were derived through the use of the plastic ruler algorithm and presented above in Figure 5.10 as examples of the atmospheric compensation process. During the data preparation process, raw SEBASS data was converted into the following data formats:

- Simulated FLIR image - single-band thermal image
- Temperature image - single-band image of estimated surface temperature
- Radiometrically calibrated data - radiance at sensor
- Atmospherically corrected data - radiance at source
- Emissivity data - apparent emissivity

## **2. Single-band Images**

Two single-band images were generated as outputs of the data preparation process. The simulated FLIR image was created by averaging the radiance received by the sensor in each of the 128 wavelength channels. The second single-band image was composed of data values representing the estimated surface temperature of each pixel.

The simulated FLIR image of the Malpai scene is presented as Figure 6.1. The FLIR image is essentially a thermal image of the scene. The bright areas represent materials emitting the most electromagnetic energy. Almost all of the targets within the Malpai collection site were distinguishable from the desert varnish because of the high temperature of the desert surface. Some man-made materials, such as the calibration panels and several elements within the JCCD arrays, differed in temperature from the other man-made objects and were also easy to distinguish. On the other hand, the vegetation and tanks appeared to emit the same amount of energy and would be hard to differentiate if they were collocated.

The single-band temperature image of the data depicted the same information as the simulated FLIR image. For comparison, the temperature image is presented as Figure 6.2. Once again, almost all materials on the training site could be detected using temperature differences alone. Several sample temperatures have been identified to demonstrate the thermal variation within the target site. The dark desert varnish heats up quickly and appeared as a bright surface in this late morning image. It provided a good contrast to the cooler T-72 tanks. The high thermal inertia of the tanks caused them to heat up more slowly. The two US tankers in the lower left corner were used to determine whether thermal sensors can detect the status of military support vehicles. The tanker on

the left was hotter than the tanker on the right by 8° K. The low thermal inertia of the empty tanker caused it to heat up quickly in the morning sun.

### 3. Principal Components Analysis

The PCA of the Malpai collection site served two purposes. The analysis was used to determine how the results would vary as the transform was applied to the radiometrically calibrated data, the atmospherically corrected data, and the emissivity data. It was then used to characterize the various targets within the site.

#### *a. Radiance Data Sets*

The radiometrically calibrated data and the atmospherically corrected data are both in radiance units,  $\mu W/cm^2 \mu m sr$ . The calibrated data represents the radiance measured at the sensor while the atmospherically corrected data represents radiance emitted at the surface. PCA was performed on both of these radiance data sets to determine if the atmospherically corrected data would provide substantially different results from the radiometrically calibrated data.

The results of applying the principal components transformation to the two data sets are presented in Figures 6.3 and 6.4. The figures portray how the variance in the original data is represented in principal component data space. Figure 6.3 is a graph of the eigenvalues of each principal component (PC) of the radiometrically calibrated and atmospherically corrected data. The figure shows that the transformation produced similar results when applied to the two data sets. The non-traditional approach of using a logarithmic horizontal axis hides the break in slope found in log-linear plots. In these data, the break occurs at PC band 12. Figure 6.4 presents the same information as a percentage of original scene variance contained in each PC. The figure shows that over 90% of the variance within the original image is contained in the first PC. Each subsequent PC contains less and less of the information contained in the original data. After the tenth PC, the remaining components contain less than 0.01 % of the original variance of the data.

The first PC typically is a weighted average of all of the bands of an instrument. In this case, the first PC produces an output similar to the simulated FLIR image. Figure 6.5 compares the simulated FLIR image to the first PC of the calibrated data and the first PC of the atmospherically corrected data. The three images are virtually identical. The fact that the first PC contains 90% of the original variance in the data and represents the temperature variations within the scene is a result of the strong relationship between temperature and emitted radiation in the LWIR region of the electromagnetic spectrum.

The second, third, and fourth PC images of the two types of radiance data were also similar. Beginning with the fifth PC, the component images of the two data sets began to differ. Figure 6.6 presents a comparison of the fifth PC image of the radiometrically calibrated data with that of the atmospherically corrected data. The T-72 tanks were easily detected in both images, but were highlighted differently because of the statistical differences between the two data sets caused by removal of atmospheric effects. Despite the alteration in the appearance of the individual images above PC number four, PCA analysis of the two data sets yielded the same amount of information.

***b. PCA Results on Calibrated Data Set***

The author chose to perform the full PCA on the radiometrically calibrated data rather than the atmospherically corrected data. Both data sets produced similar results and the use of the calibrated data eliminated any adverse effects a possible mischaracterization of the atmosphere might have on the results of the analysis.

As mentioned above, the first PC of the radiometrically calibrated data was virtually identical in appearance to both the simulated FLIR image and the surface temperature image. The first PC image exploited the temperature variations within the scene allowing materials to be detected based on their surface temperature, thermal inertia properties, or internal heat sources.

The second PC provided a large amount of information about the scene which was not present in the simulated FLIR or first PC image. Figure 6.7 presents the simulated FLIR image alongside the second PC image of the T-72 array. The weighting factors for this component highlighted materials which differed from the desert varnish

background. As a result, materials with high emissivities in the 8.0 to 9.0  $\mu\text{m}$  region where the reststrahlen band is located appeared bright. Tank tracks, desert surface variations, and T-72 array were all clearly visible.

The third PC produced some additional discrimination capabilities and allowed targets to be differentiated from the background more clearly. A portion of the third PC image is presented in Figure 6.8. The image on the left is the original third PC image. A brightness threshold has been applied to produce the image on the right. The thresholding highlighted specific targets which were emphasized by the transform. The image clearly provided a means of differentiating between man-made and natural objects within the scene. The tanks, decoy materials, and calibration panels could easily be isolated from the background.

Although the second and third PC images were useful in discriminating between man-made objects and the desert background, they did not provide much information to differentiate between different types of man-made materials. Several of the higher components provided this capability. Figure 6.9 depicts the eighth PC image with and without thresholding. The calibration panels, foxhole cover, and bomb crater decoy were easily distinguishable from both the background and the T-72 tanks.

Each of the various PC images of the radiometrically calibrated data provided different information. Figure 6.10 displays how each spectral band was weighted to generate the first, second, and eighth PCs. The figure graphically demonstrates that the first PC is essentially a weighted average of the spectral bands. The second PC emphasizes spectral measurements within the reststrahlen band of the desert sand. The determination of what the weighting factors of the eighth PC represent is not as straightforward. Since the eighth PC differentiated between elements in the JCCD array, the weighting function appears to exploit specific spectral differences between these materials. Figure 6.11 is a composite image formed by combining these three PCs into a single red-green-blue image. The figure characterizes many of the elements within the scene. The use of PC number eight aided in the discrimination between the decoy materials, the calibration panels, and the T-72 tanks. In the composite image, the desert varnish is magenta and the background vegetation is yellow. Various man-made objects

vary in color from orange in the case of the T-72 tanks to green and blue in the case of the JCCD decoy materials.

*c. Principal Components Analysis on Emissivity Data Set*

The principal components transformation was then applied to the emissivity data to determine how the conversion to emissivity would effect the results. While the eigenvalues of the emissivity data followed the same pattern exhibited by the eigenvalues of the radiance data sets, the percentage of variance contained within each component data did not drop below 0.01 % until after the 40<sup>th</sup> PC. Although this was a dramatic difference from the PCA of the radiance data, the PCs of the emissivity data represent variations within the data after the removal of the temperature variations across the scene. Since temperature variations represent up to 90% of the scene variance, removing this information increases the proportion of remaining variance contained in each PC. If the first PC is removed from the results of the radiometrically calibrated or atmospherically corrected data, the variance graphs exhibit a similar shape. This effect is shown in Figure 6.12. The figure is a comparison of the percentage of variance contained in each PC of the transformed emissivity data and the transformed radiometrically calibrated data after the removal of the first PC. The graph shows that the first few PCs of the emissivity data contain more information than the corresponding PCs in the calibrated data. But, above the tenth PC, the calibrated data retains much more information within each PC.

Figure 6.13 is a shows the weighting functions used to generate the first, second, and fifth PCs of the emissivity data. The first component resembled the second component of the radiance data and highlighted materials which have high emissivities within the reststrahlen band of the desert sand (see Figure 6.10). The results of this particular weighting are shown in Figure 6.14. The higher components once again provided a means of distinguishing between various man-made materials within the scene. The information contained in the fourth and fifth PC images allowed for excellent discrimination between the tanks, the various decoy materials, and the calibration panels. Figure 6.15 is the fifth PC image. The bright T-72 tanks were easy to distinguish from the JCCD materials and calibration panels.

A color composite of the second, fourth and fifth PC images is presented as Figure 6.16. Within the image, the T-72s appear yellow, the vegetation is orange, and elements of the JCCD array are blue-green. Tank tracks are highlighted in dark blue or magenta. Because this image is based entirely on emissivity data, it has no thermal component and would produce the same results regardless of illumination conditions. This image characterized the scene well, but the composite image generated from the radiometrically calibrated data (Figure 6.11) contained more information. The tanks tracks, vegetation, and JCCD materials were more distinct in Figure 6.11. The temperature component of the radiance data provided some additional discrimination capabilities.

#### **4. Spectral Angle Mapper Analysis**

The spectral angle mapper was applied to the emissivity data generated from the Malpai collection site. As described in Chapter II, Section C, the SAM compares the emissive spectra within a data set to a library of reference spectra. The Malpai training set provided an initial opportunity to see how well the ground truth spectra matched the data collected by SEBASS. It also served as the starting point for the development of a spectral library which would be used on the data collected over the JCCD and Arroyo sites. The ground truth spectra collected by John Hopkins University served as the primary source of reference spectra. The library was augmented with spectra extracted from the Malpai Collection Site data.

##### ***a. SAM Analysis Using Ground Truth Spectra***

The initial SAM analysis of the Malpai collection site utilized only ground truth spectra collected by John Hopkins University (see Table 5.1). The ground truth data included two target vehicle spectra. The T1326\_JHU spectrum was collected from the center T-72 in the five tank array. The MBT1152\_JHU spectrum was collected from one of the T-80 surrogate tanks.

The first SAM trial demonstrated that the ground truth spectra provided a good match to some of the materials in the scene. The algorithm was run with a spectral

angle threshold of 0.03 radians. The results are presented as Figure 6.17. All of the military vehicles were detected as one of the two target vehicle types and displayed as either red or blue. The algorithm also detected many of the tracks left by the vehicles as they were moved into position. The algorithm did not correctly identify the vegetation, some of the lighter sand, and portions of the tank tracks. The vegetation was misclassified as Air Force desert camouflage and displayed as orange. Portions of the vehicle tracks were misclassified as T-80 targets and portrayed as blue. Various JCCD materials were misclassified due to the lack of appropriate reference spectra. These materials were prototype materials and did not correspond well to the ground truth camouflage materials.

***b. SAM Analysis Using Ground Truth and Extracted Spectra***

To improve classification accuracy, the reference library was expanded to include spectra extracted from the Malpai data. Spectra representing the desert varnish, the lighter desert sand, vegetation, and a disturbed desert surface resulting from vehicular traffic were extracted from known locations within the Malpai scene. Since, the foxhole camouflage and IR appliqué exhibited very distinctive spectral characteristics and did not correspond to any of the ground truth camouflage materials, they were also added to the reference library. The full reference library consisted of the materials listed in Tables 5.1 and 5.2.

The use of the expanded reference library improved the results of the SAM analysis dramatically. The vegetation, variations in desert background, and JCCD materials were classified with much greater accuracy. The false alarms involving misclassification of the desert background and vegetation were also eliminated. Figure 6.18 is a portion of the resulting classification image using a spectral angle threshold of 0.03 radians. The tank tracks, portrayed in orange, were clearly distinct from the lighter sand and desert varnish. The vegetation was also clearly identified. But, the improvement in background classification and the reduction in false alarms was achieved at the cost of easily locating all of the threat vehicles. Only four of the T-72s were positively classified as being either T-72 or T-80 targets. The remaining T-72 had only seven pixels correctly classified as matching the T-72 spectrum.

## 5. Spectral Matched Filter Analysis

The SMF identifies spectra within a scene that closely match an input reference spectrum. The algorithm was applied to the Malpai data to determine how well each of the target T-72s matched the ground truth spectra. It was also used to conduct a quick terrain classification of the scene. Reference spectra for the SMF were taken from the same reference library generated for the SAM analysis.

The SMF was first employed to detect the military target vehicles using the T-72 and T-80 spectra. The slight difference between the T-72 and T-80 spectra was evident in the SMF results. Figure 6.19 is a portion of the SMF results for the Malpai data. The colors have been reversed in the figure to better highlight the SMF results. The dark areas represent spectra which match the T-72 and T-80 reference spectra. The image on the left is the product of a matched filter using the T-72 spectra. Only three of the five vehicles are positively detected, but the vehicles that were detected were well defined and distinct from the background. The image on the right is the result of the T-80 trail. All of the T-72 tanks were detected within the image, but the signal-to-clutter ratio was much lower making them harder to distinguish from the background. Although not portrayed in the figure, the two T-80 targets at the bottom of the collection site were strongly highlighted in T-80 filtered image. In both images, the vegetation was not highlighted indicating that the spectra from these targets were sufficiently distinct to distinguish them from vegetation. When reference spectra were extracted from the CCD materials at the north end of the site, the SMF accurately classified the materials.

Terrain classification using the SMF also worked well. The vegetation within the washes was accurately classified using the extracted vegetation spectra. The use of a single desert varnish spectrum allowed several desert features to be characterized according to how much they deviated from the reference spectrum. In fact, the use of the desert varnish spectrum produced a more extensive vehicle traffic assessment than use of the spectrum extracted directly from a particular tank track. Figure 6.20 displays the results of application of the SMF with desert varnish as the reference spectrum. The tank tracks are dark because they differ from the desert varnish which has a deeper reststrahlen emissivity minimum.

## **B. JCCD COLLECTION SITE - 23 OCTOBER 1995**

The JCCD collection site consisted of three rows of vehicles as described in Chapter IV, Section B. Two of the rows contained decoy targets and a third row contained actual threat vehicles. The SEBASS collection mission conducted at 1000 local time on 23 October included flight lines directly over all three rows.

### **1. Data Processing**

The SEBASS data was prepared using the same procedures outlined in Chapter V, Section D. Atmospheric parameters were calculated for each of the three passes. The collection runs over the Vehicle Target Line contained much more vegetation than the passes over the two decoy lines. As a result, the atmospheric parameters derived from the Vehicle Target Line were much more reliable and compared more favorably with the ARTSPEC model. Since all three data sets were collected in a span of 20 minutes over the same area, the parameters derived from the Vehicle Target Line data were applied to all three data sets. The atmospheric parameters are presented in Figure 6.21. The ARTSPEC model results are depicted as a dotted line and the scaled plastic ruler results are presented as a solid line.

### **2. JCCD Decoy Line One - 23 October 1995**

The first JCCD decoy line consisted of five decoys. The targets included murals depicting T-72 and M-1 tanks as well as decoys constructed of scrap materials. The CCD preparations of the five decoys were described in Figure 4.2 and Table 4.2.

#### ***a. Single-band Images***

The simulated FLIR image of Decoy Line One is presented as Figure 6.22. Decoy One is easily detectable in the FLIR image due to its rectangular structure and the hot spot directly in the center of the target. Its shape and thermal properties also allow the decoy to be differentiated from a true tank. Figure 6.23 is a comparison of the FLIR

image of Decoy One with a FLIR image of a T-72 from the Malpai data. Spatially the two targets appear very distinct. In addition, the temperature of the decoy varied from 308° K in the center to 299° K on the outer edges. Although the real T-72s also exhibited a temperature variation between the turret and body, the turrets were cooler than the body during this time of day due to the thermal inertia of their armor plating.

*b. Principal Components Analysis*

Principal components analysis was performed on the radiometrically calibrated data and apparent emissivity data. All five decoys were detected during the PCA analysis of the radiometrically calibrated data. Analysis of the emissivity data also resulted in the detection of the five decoys.

The results of the PCA of the radiometrically calibrated were similar to the results of PCA of the Malpai data. The first PC image was identical in appearance to the FLIR and surface temperature images and represented temperature variations within the scene. The second PC highlighted tank tracks, vegetation, and targets which differed from the majority background which in this case was the light sand. This PC image is presented as Figure 6.24. Decoy One, Decoy Four, and Decoy Five appeared as bright objects. In addition, various tracks and trails provided an indication of vehicular traffic and served as clues to the possible location of other targets and decoys within the scene. Although Decoy Three was not directly identifiable, the edge of a camouflage net was clearly evident. Thresholding was applied to an enlarged portion of the image to more clearly differentiate the edge of the camouflage netting from the general background. The higher order PC images provided additional information about the decoys.

A color composite of the first three PC images was used to combine the information contained in three components. The first three PC images were selected to characterize the desert background and highlight any man-made objects. The image is presented as Figure 6.25. Four of the decoys could be detected and the general JCCD background was characterized. Although Decoy Two was detected in the third PC image, its small size made it difficult to detect in the composite image. In the figure, the desert varnish appears as magenta. Light sand, disturbed sand, and tank tracks appear as various shades of blue-green. The vegetation is light green-orange. Decoy One is bright green.

The other four decoys are yellow-white. Table 6.1 summarizes the color index produced by this particular combination of PC images.

Color	Material
Yellow-White	Decoy/Target
Green-Orange	Vegetation
Magenta-Red	Desert Surface (Desert Varnish)
Blue	Tank Tracks

Table 6.1. Color Index for Principal Component Image Using PC Bands One, Two, and Three from Radiometrically Calibrated Data.

*c. Spectral Angle Mapper Analysis*

The spectral angle mapper was applied to the emissivity using the reference library generated during the SAM analysis of the Malpai data. The first run employed a spectral threshold of 0.03 radians. The resulting classification image is presented as Figure 6.26. The algorithm detected four of the five decoys. Decoy One highlighted in black because it was constructed out of aluminum matting which has a spectrum which does not resemble any of the input spectra. The cyan cluster above Decoy One is a ghost image of the decoy caused by the reflection and diffraction artifact identified in Chapter V, Section B. Decoy Three and Decoy Five employed various types of woodland camouflage and were classified as LCSS woodland camouflage. Decoy Four was classified as similar to the prototype foxhole camouflage. The decoy was a visual mural of a T-72 placed on top of woodland camouflage. No matches were found for T-72 or T-80 spectra. The algorithm had some problems classifying the background. It misclassified some of the tank trails as vegetation. Decreasing the spectral angle threshold to 0.01 radians produced similar results.

To determine the extent of the misclassification problem involving the vegetation reference spectrum and the tank tracks, a SAM trial was run with the extracted vegetation spectrum excluded. This second trial correctly identified the vehicle tracks

and light sand. It revealed that much of the sand within the wash had been classified as vegetation.

*d. Spectral Matched Filter Analysis*

The SMF analysis of Decoy Line One focused on detecting the various targets within the scene. The algorithm was initially run with the T-72 and T-80 spectra as inputs to determine if any targets could be quickly classified as threat vehicles. The various camouflage schemes were then used as reference spectra for detection of any CCD efforts. Finally, the desert varnish spectra was used to determine whether any vehicle tracks could be identified.

The T-72 and T-80 spectra reference produced detections of Decoy One and Decoy Four. Both of these detections had low signal-to-clutter ratios and were based in large part on the large difference these spectra had from the background. The LCSS woodland camouflage spectrum produced detections of all of the decoys except Decoy Five. The resulting filtered image is presented as Figure 6.27. To increase the contrast of the detected targets, high response values have been coded as dark gray. Decoy One was highlighted even though it was not camouflaged. Decoy Two was covered with a LCSS desert camouflage and incorrectly classified as a woodland camouflage match. Decoy Three employed an AFCENT woodland camouflage which appeared to be similar to the LCSS woodland camouflage. Decoy Four employed the LCSS woodland camouflage and had very high signal-to-clutter ratio. The use of the German woodland camouflage spectrum as a reference spectrum produced similar results. When the SMF was applied with the prototype foxhole camouflage as the reference, the algorithm detected Decoy Four with a very high signal-to-clutter ratio indicating that the decoy was a good match for the spectrum.

The application of the tank track spectrum and the vegetation spectrum produced good ground characterization results. When the extracted vegetation spectrum was used in the SMF algorithm, all of the decoys near vegetation were easily detected because they were marked by dark patches within the bright vegetation. Use of the tank track spectrum revealed the tracks leading to Decoy Five. This was the only indication of the fifth decoy produced by the SMF.

### 3. JCCD Decoy Line Two - 23 October 1995

The second JCCD decoy line consisted of four decoy targets. The targets included two high fidelity mobile artillery mockups, a field expedient decoy constructed of scrap material, and a mural of an M-1 tank. Figure 4.2 and Table 4.2 describe the CCD preparations of the four decoys.

#### *a. Single-band Images*

The simulated FLIR image of JCCD Decoy Line Two is presented as Figure 6.28. Decoy One is easily detectable in the FLIR image due to its rectangular structure and the hot spot within the camouflage. The target's linear shape differentiates it from the rounded, irregular vegetation in the wash. As was the case with the previous data, the surface temperature image (not shown) was similar to the simulated FLIR image.

#### *b. Principal Components Analysis*

Principal components analysis was performed on both the radiometrically calibrated data and apparent emissivity data. The PCA analysis of the radiometrically calibrated data resulted in the detection of Decoys One, Decoy Two, and Decoy Four. Analysis of the emissivity data resulted in the detection of the all four decoys.

The PCA results of the radiometrically calibrated data were similar to the results of the Malpai data. The second PC highlighted tank tracks, vegetation, and targets which differed from the desert sand. Figure 6.29 demonstrates how the second PC image highlighted Decoy One and Decoy Four. The portion of the image in which Decoy Four was located has been enlarged to further demonstrate the detection capabilities of this PC. The third PC image highlighted Decoy Two and Decoy Four.

A color composite of the first three PC images is presented as Figure 6.30. This image illustrates the detection of three of the decoys. The resulting image is similar to the three-band composite of Decoy Line One presented as Figure 6.25. The color index is similar to that listed in Table 6.1. The desert background is magenta. Tracks and disturbed sand are blue. The vegetation is a light orange-green. Decoy One is also green,

but has a darker hue and a rectangular outline. Decoy Two and Decoy Four are yellow-white. Decoy Three, although not directly detectable, may be located at the base of the tracks highlighted in the image on the right.

The analysis of the emissivity data provided an opportunity to detect Decoy Three. The decoy was detected in the third and fourth PCs. Figure 6.31 is a subset of a color composite of the first three PC images of the emissivity data. It is a portion of the decoy line containing Decoy Three and Decoy Four. Although the background colors within this image differ from those in Figure 6.30, the decoys still appear as white.

*c. Spectral Angle Mapper Analysis*

The spectral angle mapper was applied to the emissivity data using the same reference library generated during the SAM analysis of the Malpai data. The first run employed a spectral angle threshold of 0.03 radians. Only Decoy Four was identified. Decoy Four was a mural of an M-1 with an East German woodland camouflage net in front. The algorithm classified it as a combination of LCSS woodland camouflage and Air Force desert camouflage. The slight misclassification was due to the lack of ground truth on the East German camouflage. Once again, much of the desert sand including some of the tank tracks was incorrectly classified as vegetation. The algorithm produced similar results when run with a smaller spectral angle threshold of 0.01 radians.

The analysis was repeated with a spectral library that excluded the extracted vegetation spectrum. The results are presented in Figure 6.32. In order to separate the T-72/T-80 targets from the Air Force desert camouflage, the Air Force desert camouflage is portrayed as black in this image. Despite a few false alarms, Decoy One, Decoy Two, and Decoy Four were detected. Decoy One was correctly identified as being covered with Air Force desert camouflage. Decoy Two was classified as a combination of T-72 and Air Force desert camouflage spectra. It was actually a mobile artillery decoy covered by a woodland camouflage net. Decoy Three was not clearly detected even though the German camouflage employed on the target was one of the ground truth spectra used in the reference library. Decoy Four was classified as a combination of T-72, Air Force desert camouflage, and LCSS woodland camouflage. It was actually a mural of an M-1 tank next to an East German camouflage net. A spatial filter was then

applied to remove some of the false alarms. Although this reduced the number of small false alarms, several tank-sized false alarms still remained. An example of the spatially filtered output displaying Decoy Two, Decoy Four, and several false alarms is presented as Figure 6.33.

*d. Spectral Matched Filter Analysis*

The SMF analysis of JCCD Decoy Line Two detected all four decoys using several of the ground truth camouflage spectra. Decoy Two, Decoy Three, and Decoy Four were detected using the LCSS and West German woodland camouflage spectra. The resulting filtered image is presented as Figure 6.34. Dark pixels represent data which closely match the input reference spectrum. All three of these decoys employed some form of woodland camouflage. In a separate application of the SMF with the Air Force desert camouflage spectra, the large net over Decoy One was classified. Application of the T-72 and T-80 spectra did not produce any significant target detections.

**4. JCCD Vehicle Target Line - 23 October 1995**

The final JCCD line consisted of the five threat vehicles. The targets included four T-72 tanks and one mobile artillery piece. Figure 4.2 and Table 4.3 describe the CCD preparations of the targets. These targets were camouflaged using earth, sand bags, and cut vegetation. Only one of the targets employed camouflage material as its primary CCD effort.

*a. Single-band Images*

The simulated FLIR image of JCCD Vehicle Target Line is presented in Figure 6.35. The target line was a wash with a moderate amount of vegetation. The SEBASS target run included Tanks One through Four. The engine of Tank Four was operated during the morning. The heat generated in the engine allowed the FLIR and surface temperature images to detect the tank. The temperature of the hottest part of the tank was 325° K. No other vehicles were detected in the single-band images.

*b. Principal Components Analysis*

The PCA performed on the radiometrically calibrated data and apparent emissivity data produced similar results. Only one target was detected. Tank One was first detected in the third PC image of the radiometrically calibrated data. It was detected in the second PC of the emissivity data.

A color composite of the first three PC images is presented as Figure 6.36. This image highlights Tank One and characterizes of the general JCCD background. The colors for this image are similar to those listed in Table 6.1. The desert background is magenta. Tracks and disturbed sand are blue. The vegetation in this image is a more distinct green. The one detected target is yellow-white.

*c. Spectral Angle Mapper Analysis*

The spectral angle mapper was applied to the emissivity data using the reference library generated during the SAM analysis of the Malpai data. The first run employed a spectral angle threshold of 0.03 radians. The algorithm detected the desert camouflage over Tank One as being similar to Air Force desert camouflage. The vehicle was actually camouflaged with a United Kingdom desert camouflage pattern. The algorithm also detected a set of tank tracks that passed through the wash. Figure 6.37 is the classification image generated after the algorithm was run with a smaller spectral angle threshold.

*d. Spectral Matched Filter Analysis*

The spectral matched filter analysis of the JCCD Target Vehicle Line produced one detection based on CCD efforts. No T-72 or T-80 targets were detected. The camouflage employed on Tank One was identified in several filtered images. The two forms of desert camouflage, Air Force desert camouflage and LCSS desert camouflage, detected the United Kingdom desert camouflage over the target. The prototype foxhole camouflage spectrum also produced a good detection. Of the three camouflage spectra that detected the target, the Air Force desert camouflage filter achieved the highest signal-to-clutter ratio indicating that the camouflage employed by

the tank resembled it the closest. The results of the SMF analysis using the Air Force camouflage are presented in Figure 6.38. The image is scaled such that darker pixels represent matches to the target spectrum. The figure illustrates the detection of Tank One.

### **C. ARROYO COLLECTION SITE - 23 OCTOBER 1995**

The Arroyo site contained two TBM targets and four threat vehicles. The threat vehicles were arranged in a protective perimeter around the high value targets. The site layout is depicted in Figure 4.3. The CCD measures employed on each target are listed in Table 4.4.

#### **1. Data Processing**

The data collected over the Arroyo Collection Site was prepared using the same procedures outlined in Chapter V, Section D. The Arroyo site had a moderate amount of vegetation. As a result, the plastic ruler atmospheric compensation method performed well. The scaled atmospheric parameters and results of the ARTSPEC model are presented in Figure 6.39.

#### **2. Single-band Images**

The simulated FLIR image of Arroyo collection site is presented as Figure 6.40. The SEBASS collection mission flew directly over the two TBM assets. One of the TBMs was visible in the both the FLIR image and the surface temperature image. The large shape of TBM One in relation to the surrounding vegetation made it a clear target. A structure just north of the road in the bottom of the image is another possible target. It corresponds to the location of Tank Four which was covered with a thermal space frame. The other targets in the scene were not be detected in either the FLIR or surface temperature image.

### **3. Principal Components Analysis**

Principal components analysis of the radiometrically calibrated data and emissivity data resulted in the detection of the two TBMs and Tank Four. The first component of the radiance data resembled the FLIR and temperature images. The second highlighted vegetation, tracks within the sand, and man-made objects. The PC images provided some interesting information concerning TBM One. The camouflage over TBM One was composed of desert camouflage with some woodland camouflage patches. These patches were visible in the different principal component images. Figure 6.41 shows a portion of the second and third principal component images in which TBM One is visible. The variations within the camouflage netting as well as the boundary between the camouflage and the desert varnish are clearly visible. Analysis of the emissivity data resulted in detection of the same three targets.

### **4. Spectral Angle Mapper Analysis**

The spectral angle mapper was applied to the emissivity data using the same reference library generated during the SAM analysis of the Malpai data. The resulting classification image of this trial is presented as Figure 6.42. A spectral angle threshold of 0.03 radians was employed. The algorithm identified the two TBMs and Tank Four. Tank Four and TBM Two were classified as resembling the prototype foxhole camouflage and are portrayed in purple. Examination of the spectra of these targets revealed that their emissive spectra matched that of the foxhole camouflage very closely. TBM One was classified as employing a combination of desert and woodland camouflage. Various tracks and trails were identified and indicated that a lot of vehicle traffic had occurred on the site. Several LCSS woodland camouflage false alarms were noted within some of the vegetation. In addition, an area of disturbed desert sand in the lower right corner of the figure was misclassified. The algorithm classified it as a T-72/T-80 target. Examination of the spectra in this area revealed that it did not match the other desert surface spectra very well. Therefore, the SAM algorithm chose the closest spectra which was the T-72 target spectra.

Based on the results of the JCCD analysis, the SAM was applied once again without the extracted vegetation spectrum to see the results of any possible misclassification of the desert sand. This second trial reduced the amount of desert sand within the wash that was classified as vegetation. It also revealed that some of the woodland camouflage over TBM One had been classified as vegetation. The same three targets were detected, but TBM One identified with a higher confidence level.

## **5. Spectral Matched Filter Analysis**

Application of the SMF resulted in the characterization of both TBM emplacements and Tank Four. The combination woodland and desert camouflage of TBM One was detected using the LCSS woodland and desert camouflages. Figure 6.43 is the resulting filtered image. The darker pixels represent matches to the target spectra. The difference in appearance of the camouflage between the two filtered images was caused by use of patches of woodland camouflage within the desert camouflage. Tank Four and TBM Two were easily detected using the prototype foxhole camouflage. The camouflage scheme employed by these two targets appears to be based on the same chemical composition.

## **D. TARGET DETECTION RESULTS**

The results of the various algorithms are presented below in Table 6.2. The targets and decoys are labeled as detected if they were picked out of the background by the algorithm. A target or decoy is labeled as characterized if specific materials or characteristics about the target were identified. This included cases where a material so closely matched a particular ground truth spectra that the materials must be related. For example, no ground truth was available for the camouflage materials employed over TBM Two and Tank Four in the Arroyo site. The spectra of these materials matched that of the prototype foxhole camouflage very closely and indicated that the materials must be

related. In this case, a match between the foxhole camouflage and the CCD material was considered a characterization.

Target	FLIR	PCA (radiometrically calibrated data)	PCA (emissivity Data)	SAM	SMF
<b>JCCD Line 1</b>					
Decoy 1	Detected	Detected	Detected	Detected	Detected
Decoy 2	Not Detected	Detected	Detected	Not Detected	Detected
Decoy 3	Not Detected	Detected	Detected	Characterized	Characterized
Decoy 4	Not Detected	Detected	Detected	Characterized	Characterized
Decoy 5	Not Detected	Detected	Detected	Characterized	Not Detected
<b>JCCD Line 2</b>					
Decoy 1	Detected	Detected	Detected	Characterized	Characterized
Decoy 2	Not Detected	Detected	Detected	Detected	Characterized
Decoy 3	Not Detected	Not Detected	Detected	Not Detected	Characterized
Decoy 4	Not Detected	Detected	Detected	Characterized	Characterized
<b>JCCD Target Vehicle Line</b>					
Tank 1	Not Detected	Detected	Detected	Characterized	Characterized
Tank 2	Not Detected	Not Detected	Not Detected	Not Detected	Not Detected
Tank 3	Not Detected	Not Detected	Not Detected	Not Detected	Not Detected
Tank 4	Detected	Not Detected	Not Detected	Not Detected	Not Detected
<b>Arroyo</b>					
TBM 1	Detected	Detected	Detected	Characterized	Characterized
TBM 2	Not Detected	Detected	Detected	Characterized	Characterized
Tank 4	Detected	Detected	Detected	Characterized	Characterized

Table 6.2. Results of Hyperspectral Analysis of SEBASS Data Collected 20 October 1995 at 1000 and 23 October 1995 at 1000.



## VII. SUMMARY AND CONCLUSIONS

The first operations of a thermal infrared imaging spectrometer were conducted on 20 - 24 October 1995. Analysis of the LWIR spectral data collected resulted in the successful detection of military targets. Targets were detected through principal components analysis of the radiometrically calibrated SEBASS data. Analysis of processed SEBASS resulted in the classification and characterization of targets and background materials.

SEBASS performed well during the exercise. Instrument characterization and calibration efforts allowed spectral analysis to be conducted using ground truth spectra collected by other instruments at different times. Although several instrumental artifacts were discovered during the analysis of the WESTERN RAINBOW data, they did not severely degrade the sensor's ability to collect meaningful data. These artifacts were dealt with in software corrections. The proposed solution for the amplifier gain variation worked well. The thermal drift and nonlinear response of the focal plane were effectively characterized through the use of multiple calibration measurements.

The plastic ruler atmospheric compensation method was designed to operate on data which includes a large amount of near-blackbody materials. The sparse vegetation within the WESTERN RAINBOW collection sites significantly impacted the algorithm's results. The small number of near-blackbody pixels caused the projection of spectral features from the majority elements in the scene, such as sand, into the derived atmospheric parameters. The parameters then passed these features onto the apparent emissivity spectra. In addition, the author found that the routine was very sensitive to changes in the number of bins used for the statistical determination of the transmittance and upwelling radiance parameters. Changes in binsize as small as 5 or 10 pixels produced changes in the fine structure of the resulting atmospheric transmittance and upwelling radiance profiles. Again, these errors were propagated through to the derived emissivity spectra as the data were converted to radiance at the ground.

Principal component analysis demonstrated that SEBASS was capable of collecting thermal spectral data with sufficient spectral and radiometric resolution to

detect and discriminate military targets. The analysis revealed that the data collected by SEBASS were not only capable of discriminating between the majority background and man-made materials, but were also capable of discriminating between classes of man-made materials. The analysis showed a modest increase in noise introduced by the conversion from radiance to apparent emissivity.

The spectral angle mapper and spectral matched filter demonstrated that the conversion to apparent emissivity produced accurate classification results when ground truth spectra were used as reference spectra. This was an important result because atmospheric compensation and the derivation of apparent emissivity introduced additional artifacts which may have obscured or altered characteristic spectral features. The classification algorithms demonstrated the successful detection of various camouflage materials. They also were successful in categorizing the major terrain features of the desert including vegetation, desert varnish, disturbed sand, and roads and trails. Of the two, the spectral matched filter produced the best results. The spectral angle mapper had difficulty distinguishing between several of the camouflage materials and the T-72 target spectra. It also had difficulty correctly classifying the lighter desert sand and vegetation. It is believed that overestimation of surface temperatures resulted in slope variations in the derived emissivity spectra. In the case of the above materials, these variations produced variations in spectral reference angle and resulted in misclassification.

The spectral matched filter performed better than the spectral angle mapper. The process used to convert radiance units to apparent emissivity often overestimated surface temperature. This caused slope variations in derived emissivity spectra. It is believed that the spectral angle mapper misclassifications were caused by these slope variations which were larger than the characteristic spectral features of many of the materials within the a scene.

The capability demonstrated by SEBASS during Exercise WESTERN RAINBOW has many implications to military remote sensing at a time when battlefield awareness has become a dominant factor in warfare. The results of this analysis indicate that an infrared spectral sensor can satisfy several key military intelligence needs such as target detection

and terrain categorization. A thermal spectral sensor like SEBASS can detect and discriminate between targets under all lighting conditions based on spectral differences alone. It can also serve as a cueing sensor performing anomaly detection over a large area. Finally, infrared spectral information has the capability to identify specific target materials.



## APPENDIX A. FIGURES

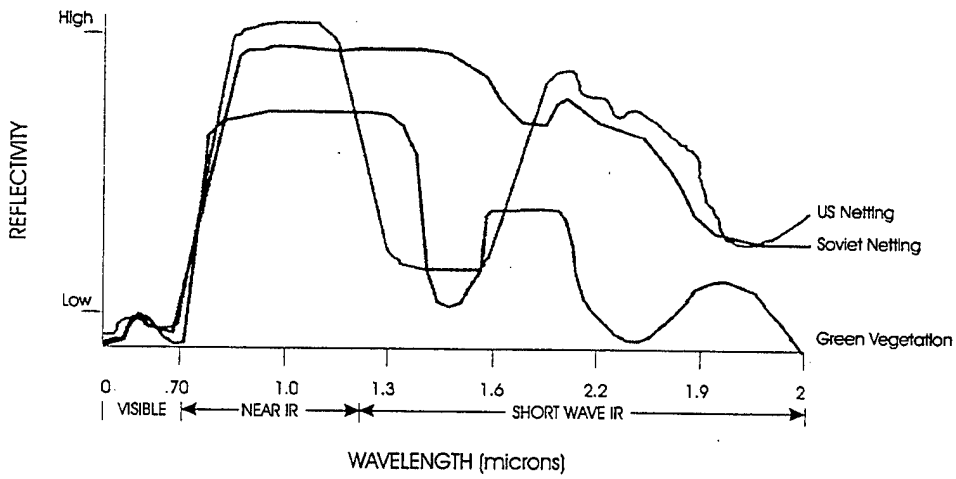


Figure 2.1. US and Soviet, Camouflage and Healthy Green Vegetation Comparisons.  
From Multispectral Users Guide, 1995.

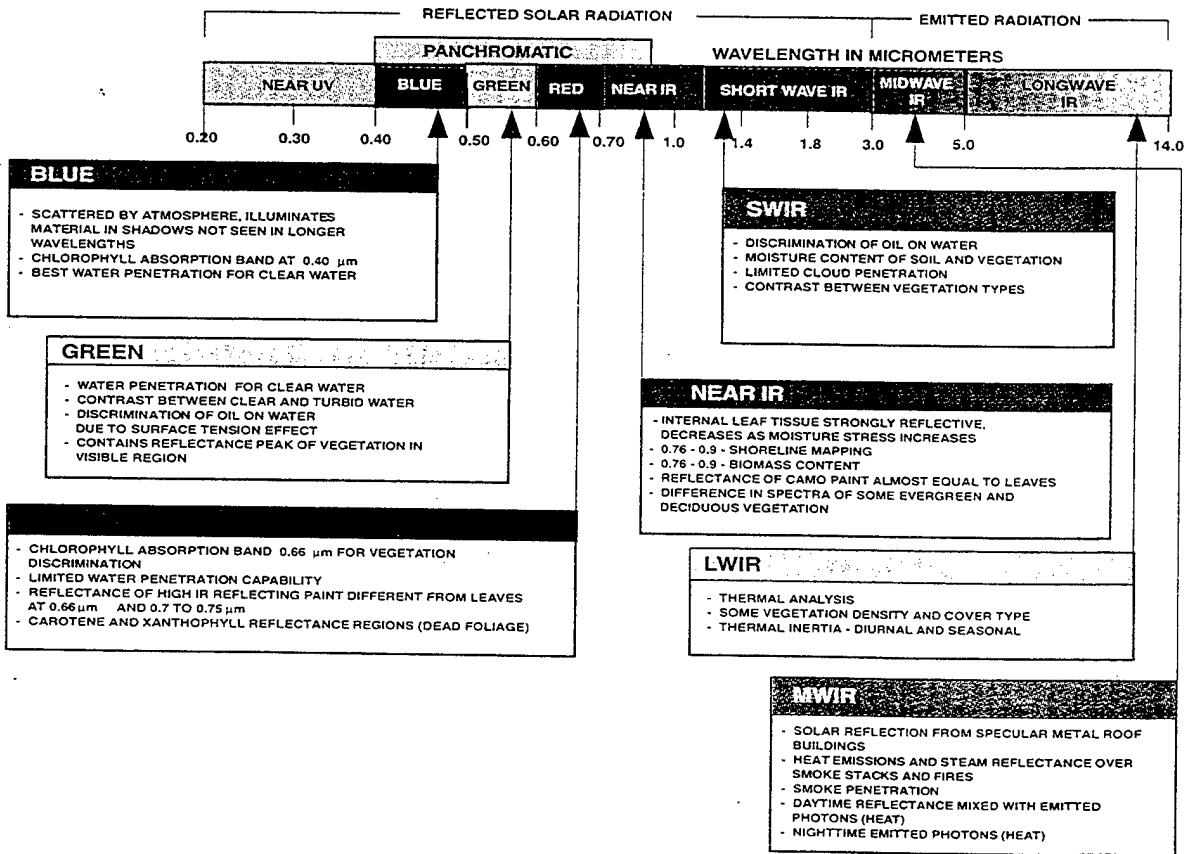


Figure 2.2. Characteristics of Spectral Regions. From Multispectral Users Guide, 1995.

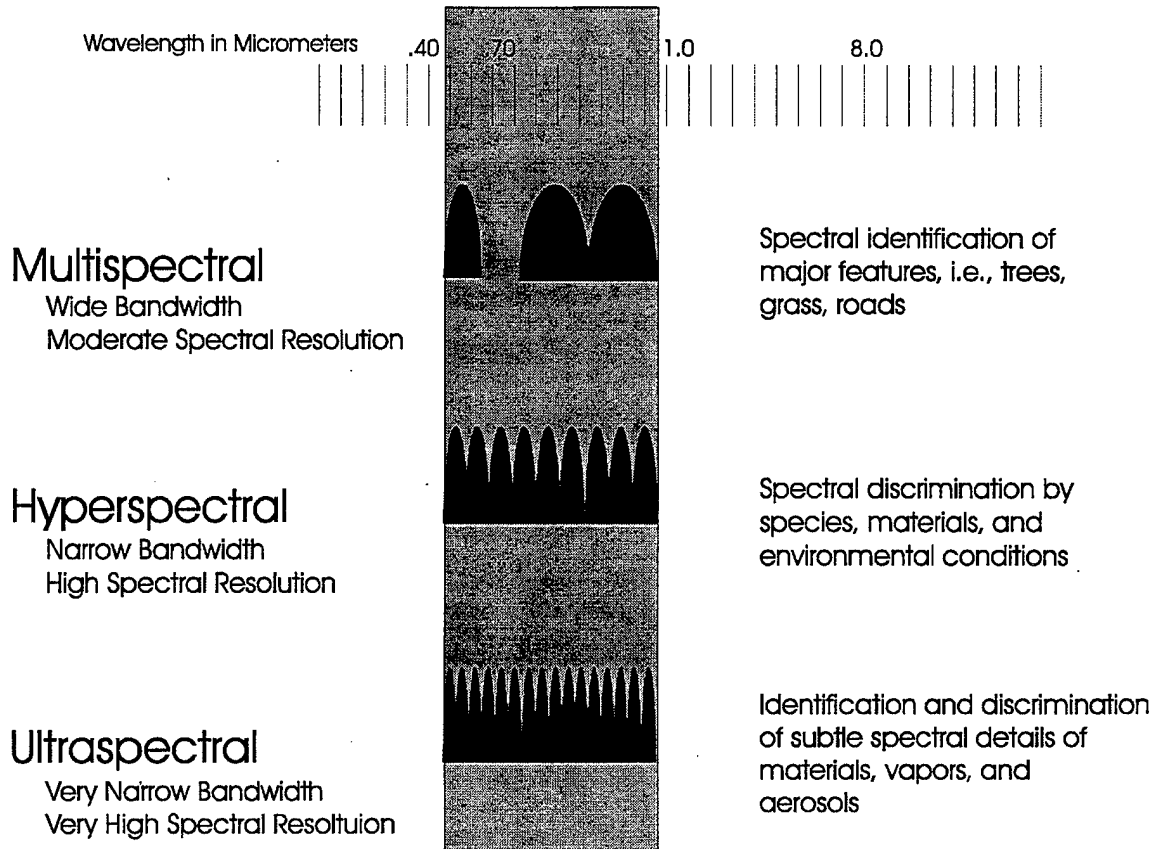


Figure 2.3. Classes of Spectral Imaging Sensors. From Multispectral Users Guide, 1995.

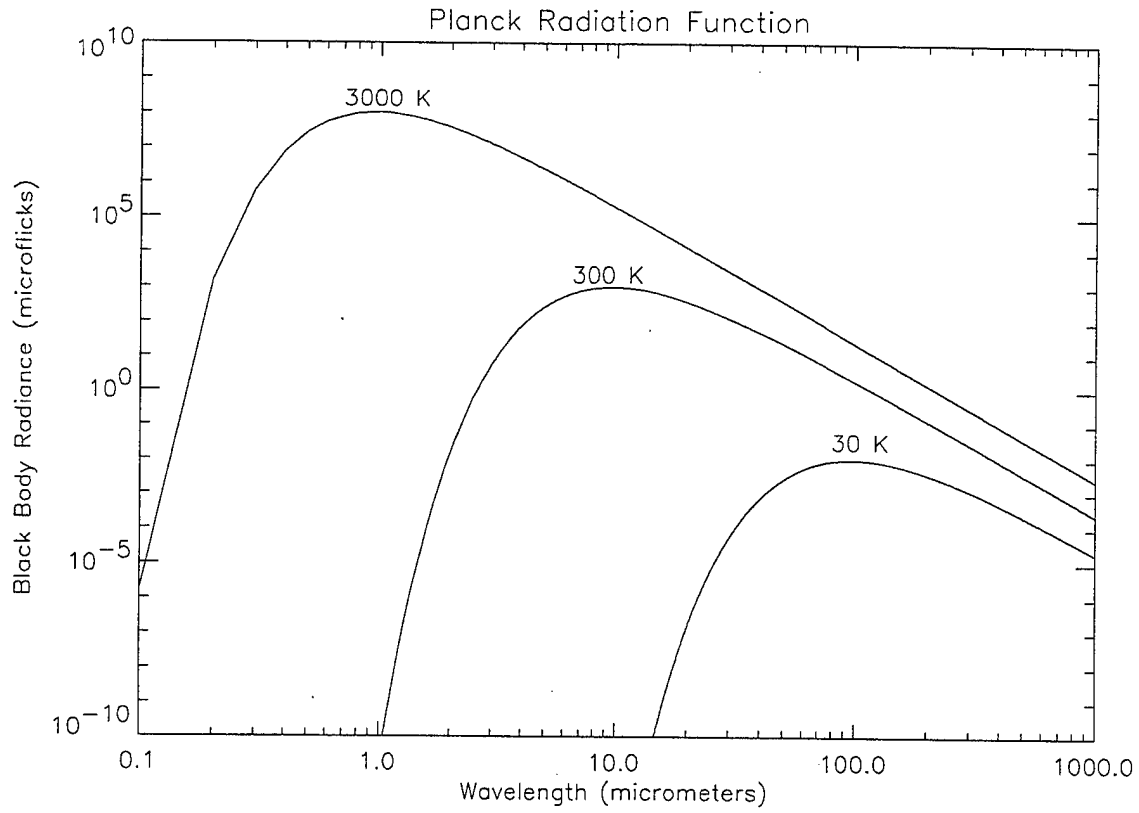


Figure 2.4. Planck Radiation Function.

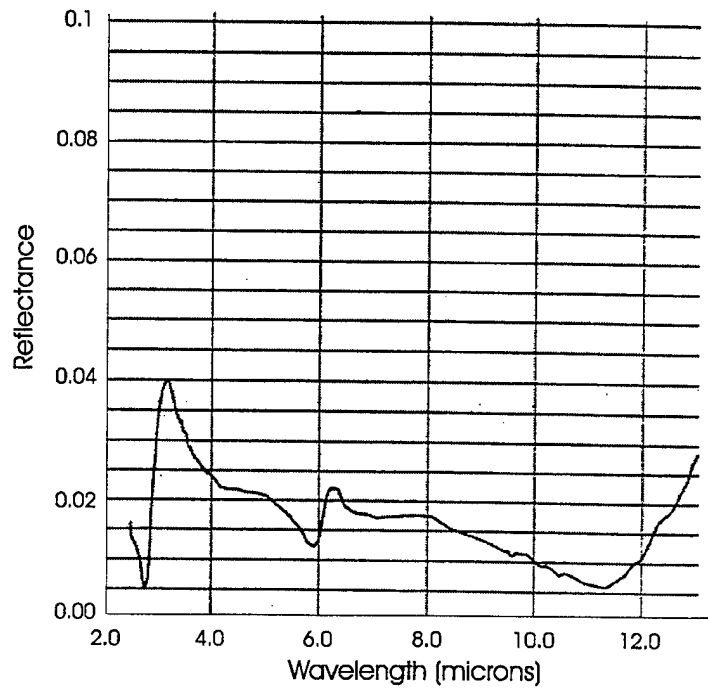


Figure 2.5. Reflectance of Pure Water. From Anderson, et al, 1994.

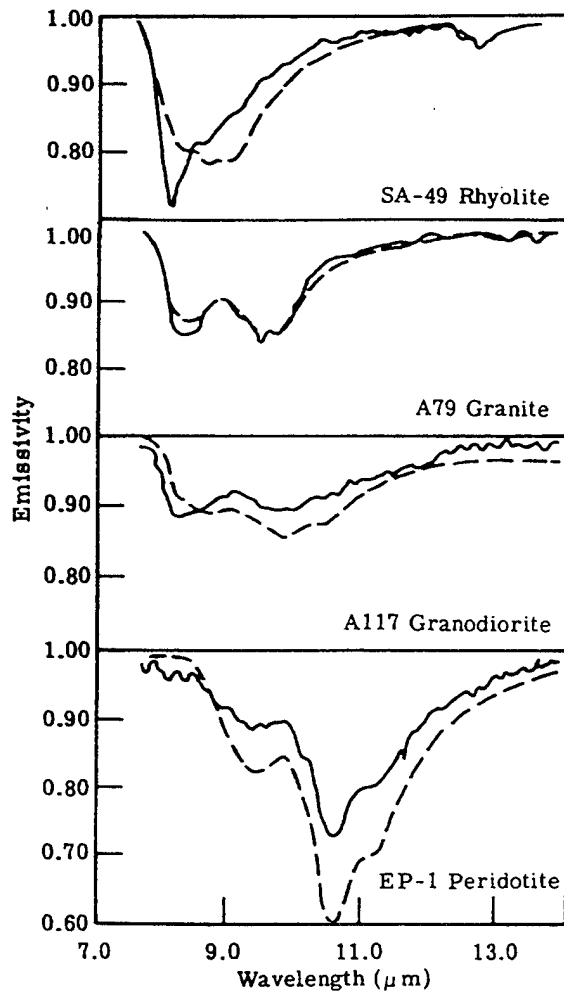


Figure 2.6. Emissivity of Several Minerals. From Zissis, 1993.

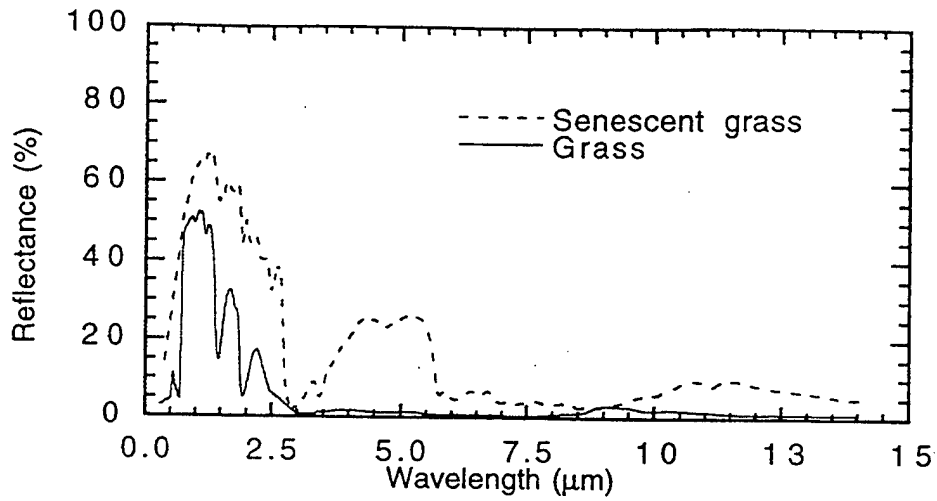


Figure 2.7. Reflectance Spectra of Healthy and Senescent Grass. From John Hopkins University, 1995.

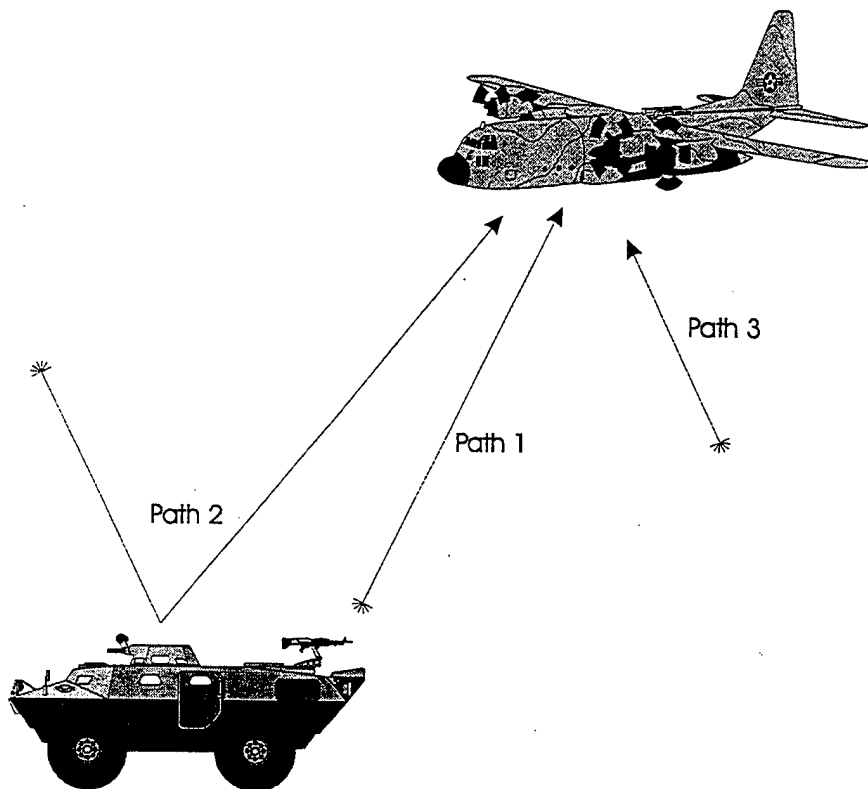


Figure 2.8. Sources of LWIR Radiation. After Multispectral Users Guide, 1995.

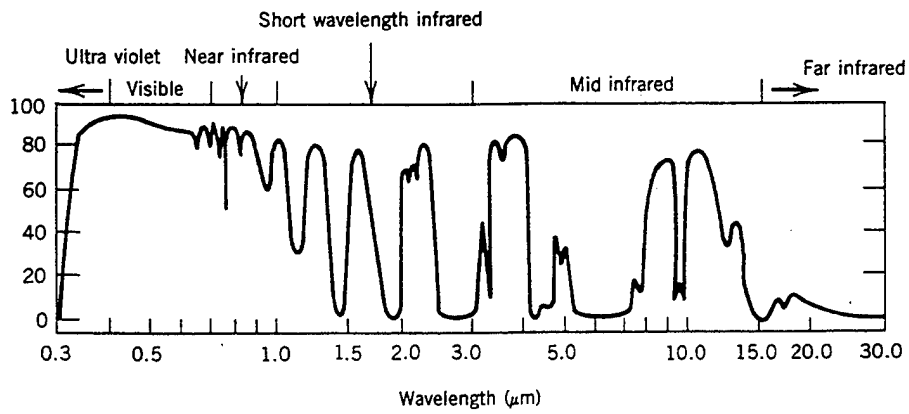


Figure 2.9. Atmospheric Transmission Characteristics. From Elachi, 1987.

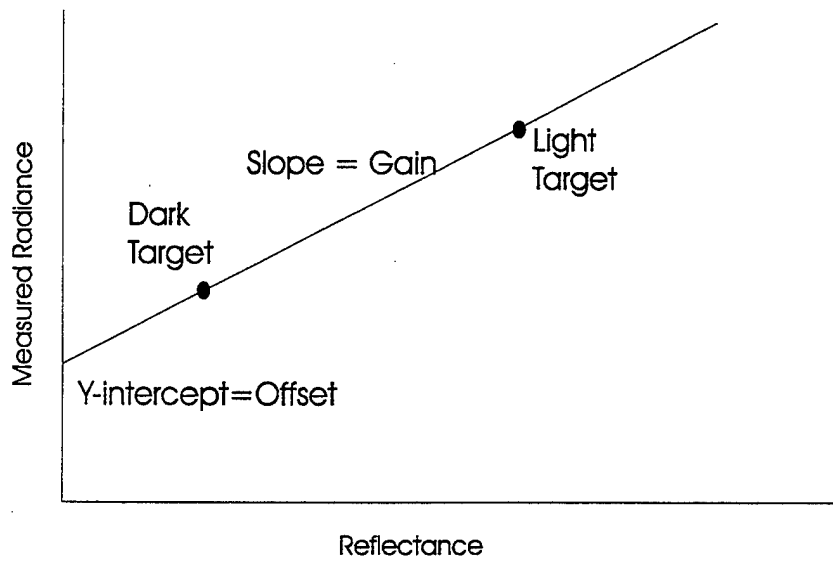


Figure 2.10. Empirical Line Method. After Farrand, 1994.

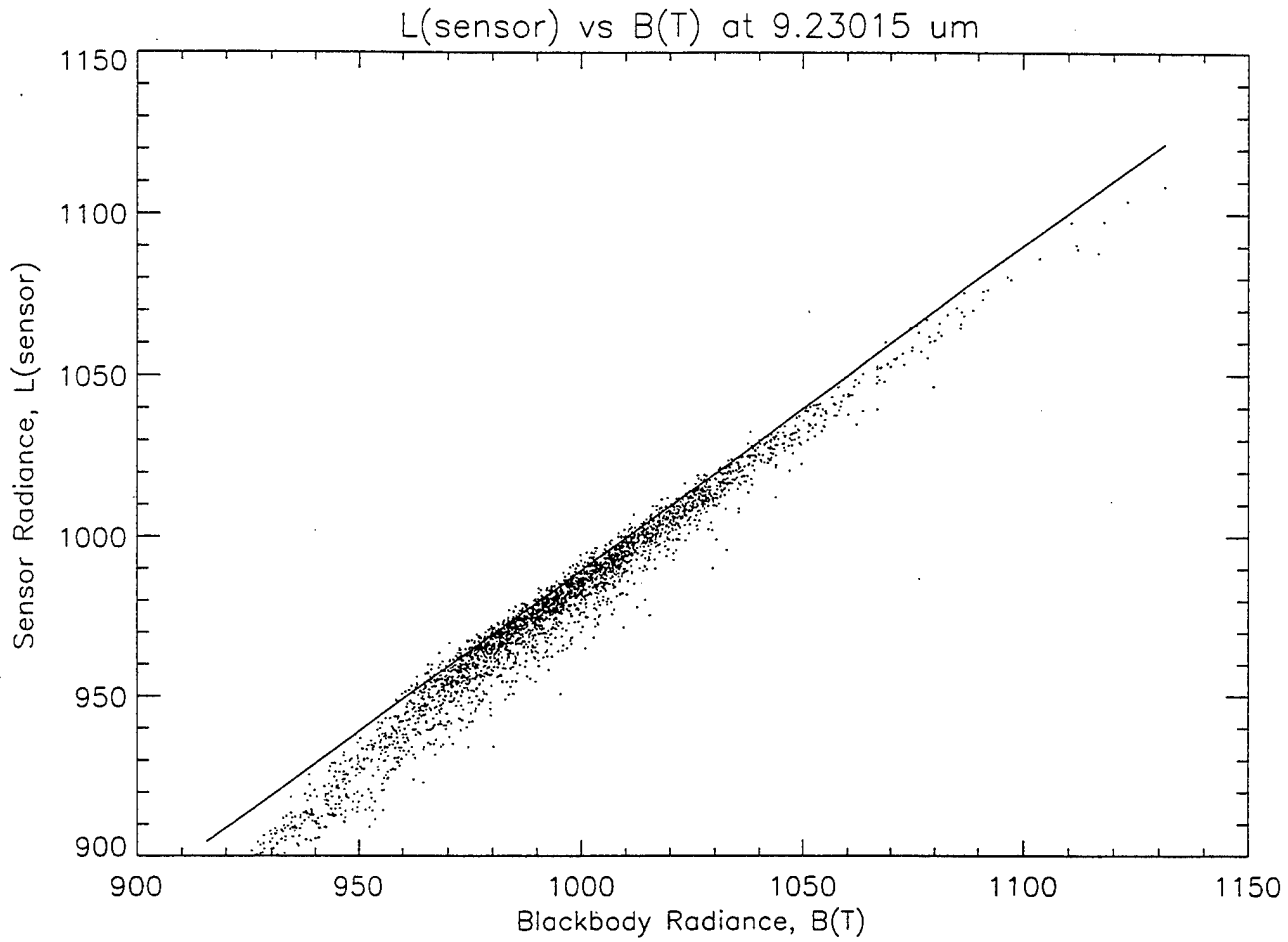


Figure 2.11. Scatter Plot of Measured Radiance vs. Blackbody Radiance for a Single Band.

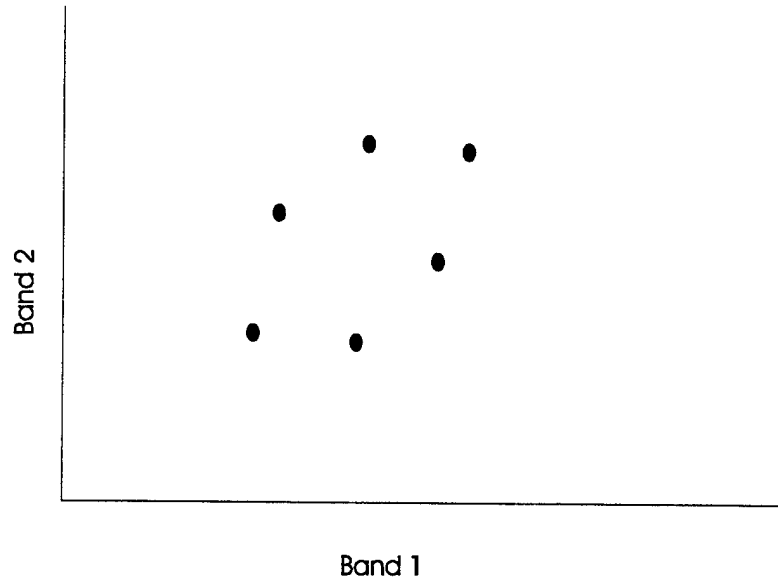


Figure 2.12. Scatter Plot of Two-dimensional Data Showing High Correlation. After Richards, 1993.

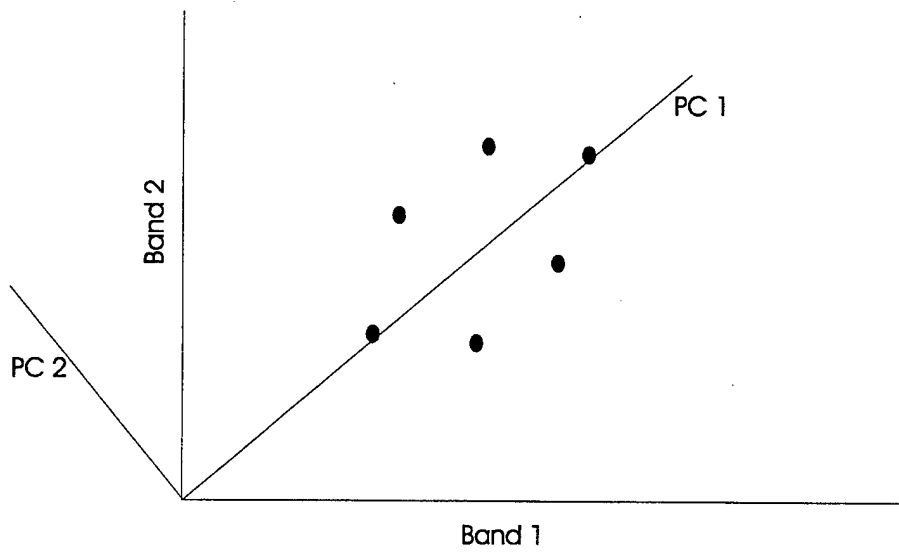


Figure 2.13. Illustration of Coordinate Rotation. After Richards, 1993.

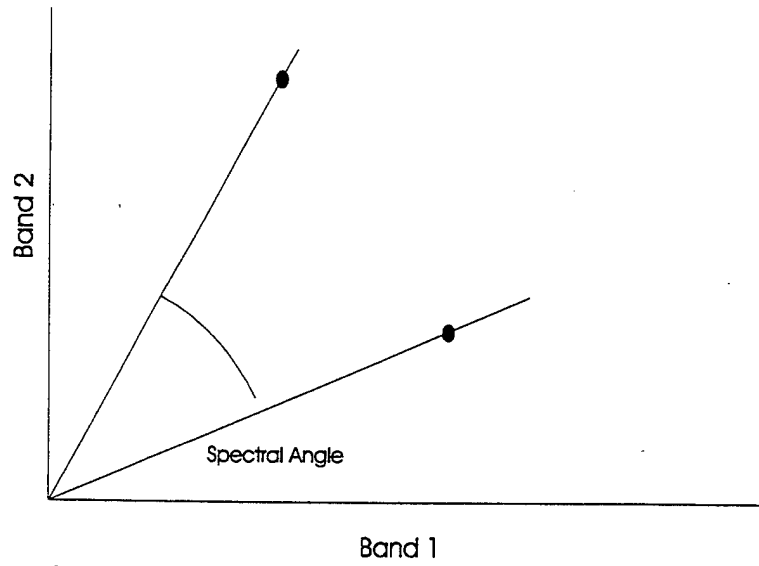


Figure 2.14. Illustration of Spectral Angle. After Kruse, et al, 1993.

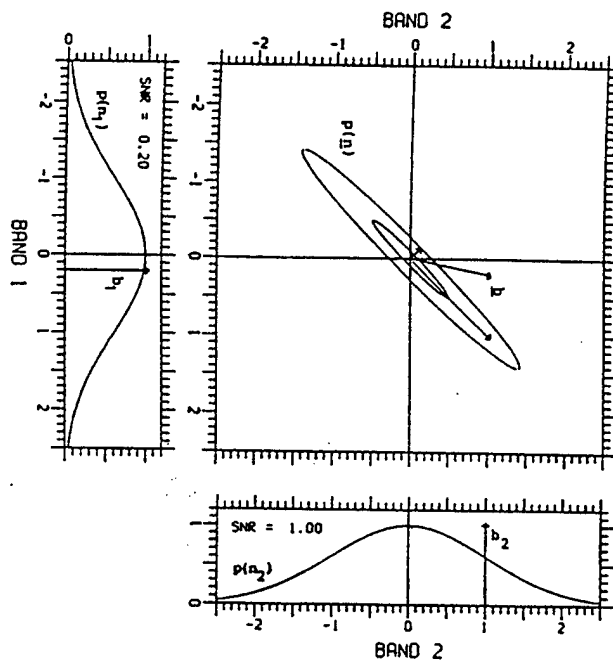


Figure 2.15. Orientation of Signal Vector,  $\bar{b}$ , and Clutter Density in Two-Dimensional Band Space. From Stocker, et al, 1990.

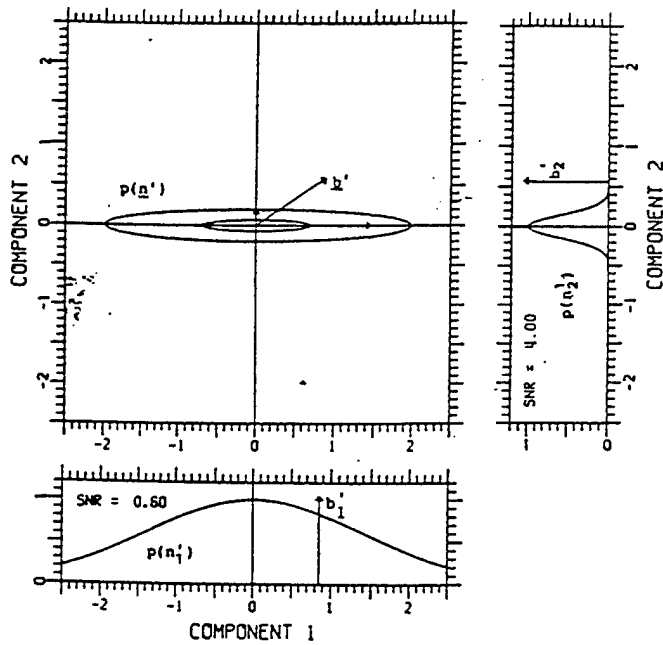


Figure 2.16. Orientation of Signal Vector,  $\bar{b}$ , and Clutter Density Principal Component Space. From Stocker, et al, 1990.

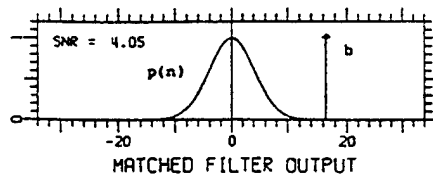


Figure 2.17. Weighted Combination of Components from Figure 2.16 Which Maximizes Signal-to-Clutter Ratio. From Stocker, et al, 1990.

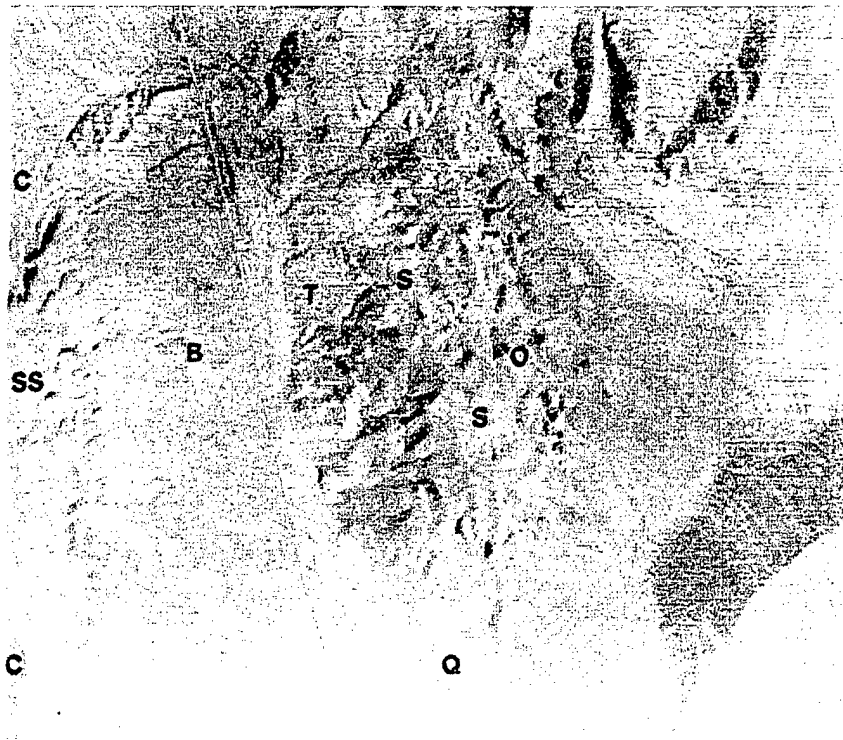


Figure 3.1. TIMS Image of Cuprite Mining District Processed with Decorrelation Stretch. Abbreviations: B basalt, C carbonates, O opalized units, Q small blue fan, S silicified rocks, SS harkless siltstone, T unaltered tuffs. From Kahle and Goetz, 1983.

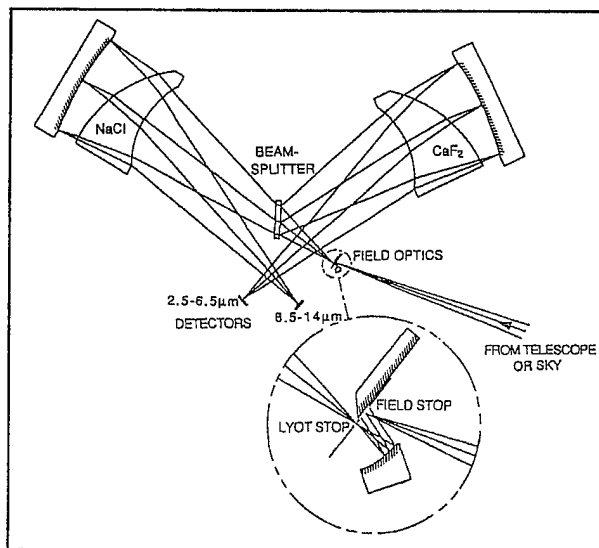


Figure 3.2. Optical Layout of BASS. From Bongiovi, Hackwell, and Hayhurst, 1995.

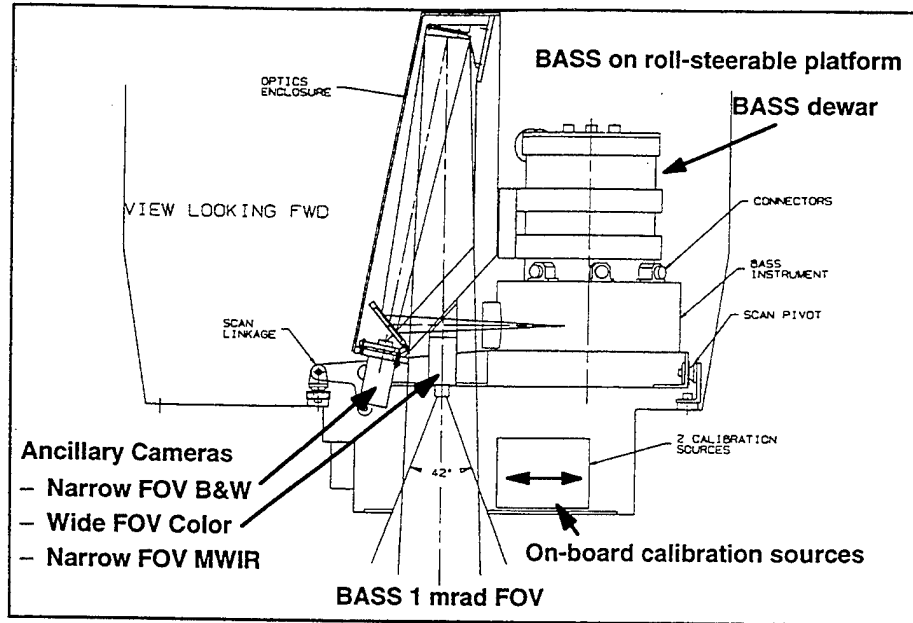


Figure 3.3. BASS Twin Otter Configuration. From Bongiovi, Hackwell, and Hayhurst, 1995.

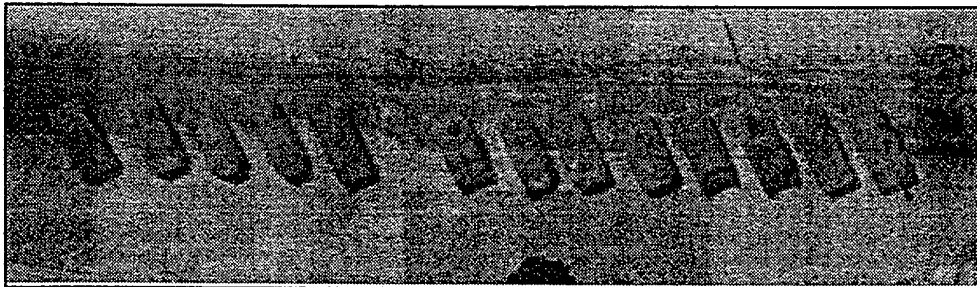


Figure 3.4. Target Line of Military Vehicles. From Bongiovi, Hackwell, and Hayhurst, 1995.

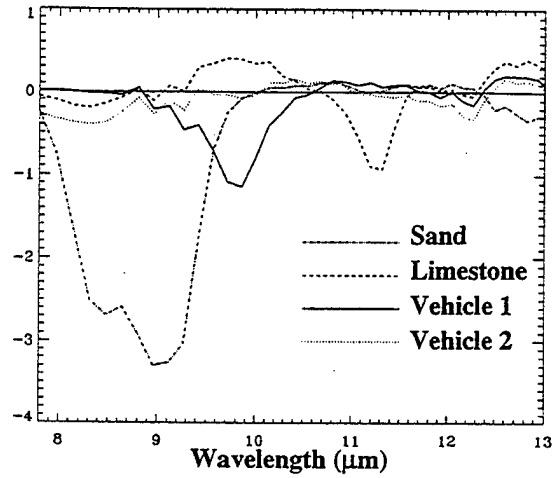


Figure 3.5. Spectral Templates of Target Materials. From Bongiovi, Hackwell, and Hayhurst, 1995.

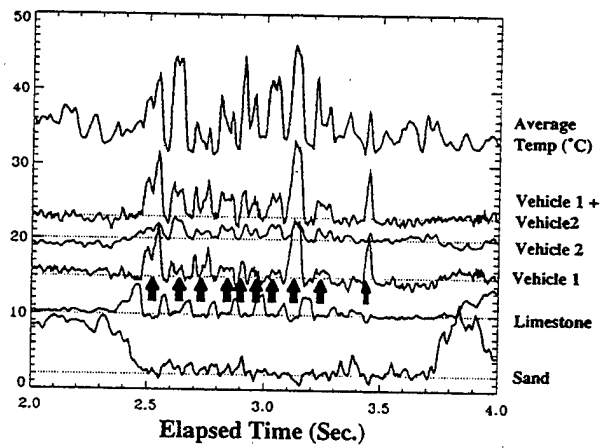


Figure 3.6. Response Plot for Initial Training Scene of Military Vehicles. From Bongiovi, Hackwell, and Hayhurst, 1995.

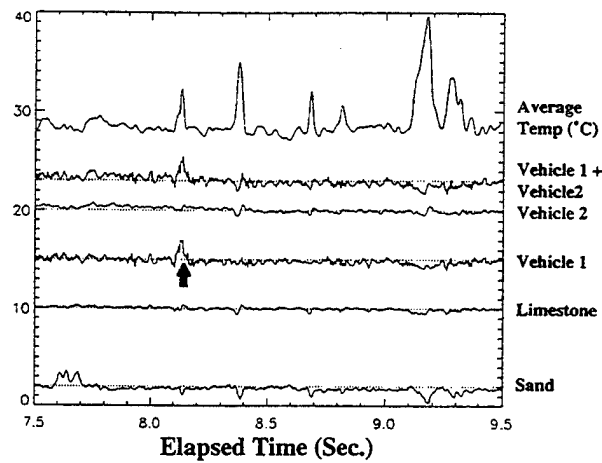


Figure 3.7. Response Plot for Tank Concealed in Trees. From Bongiovi, Hackwell and Hayhurst, 1995.

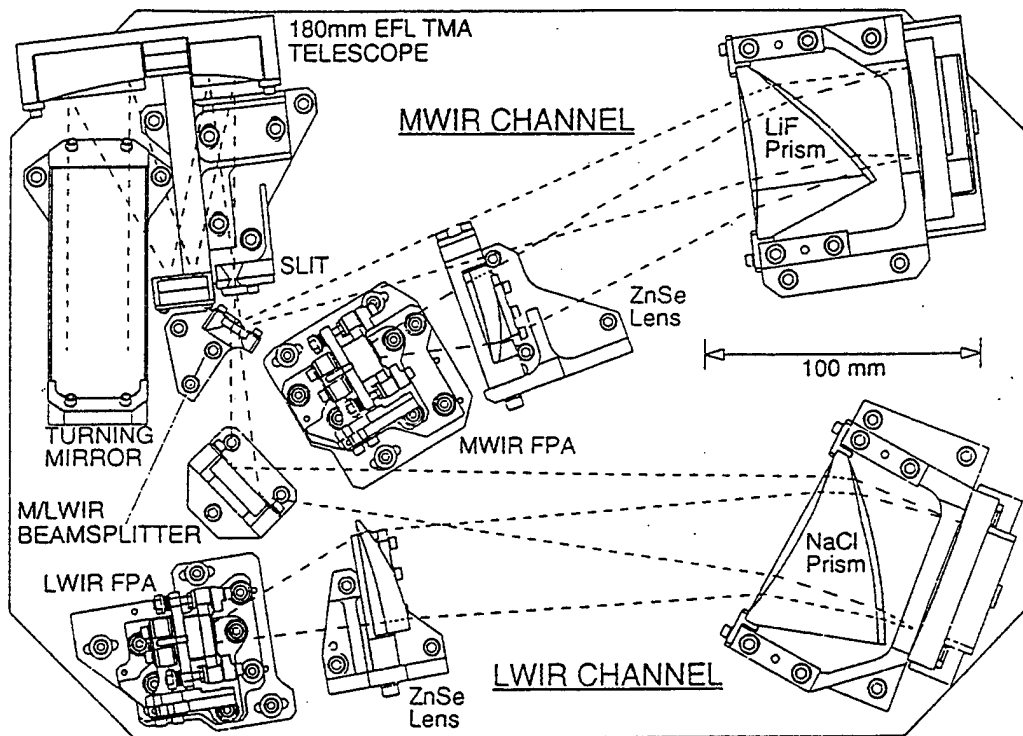


Figure 3.8. Optical Layout of SEBASS. From Hackwell, 1995.

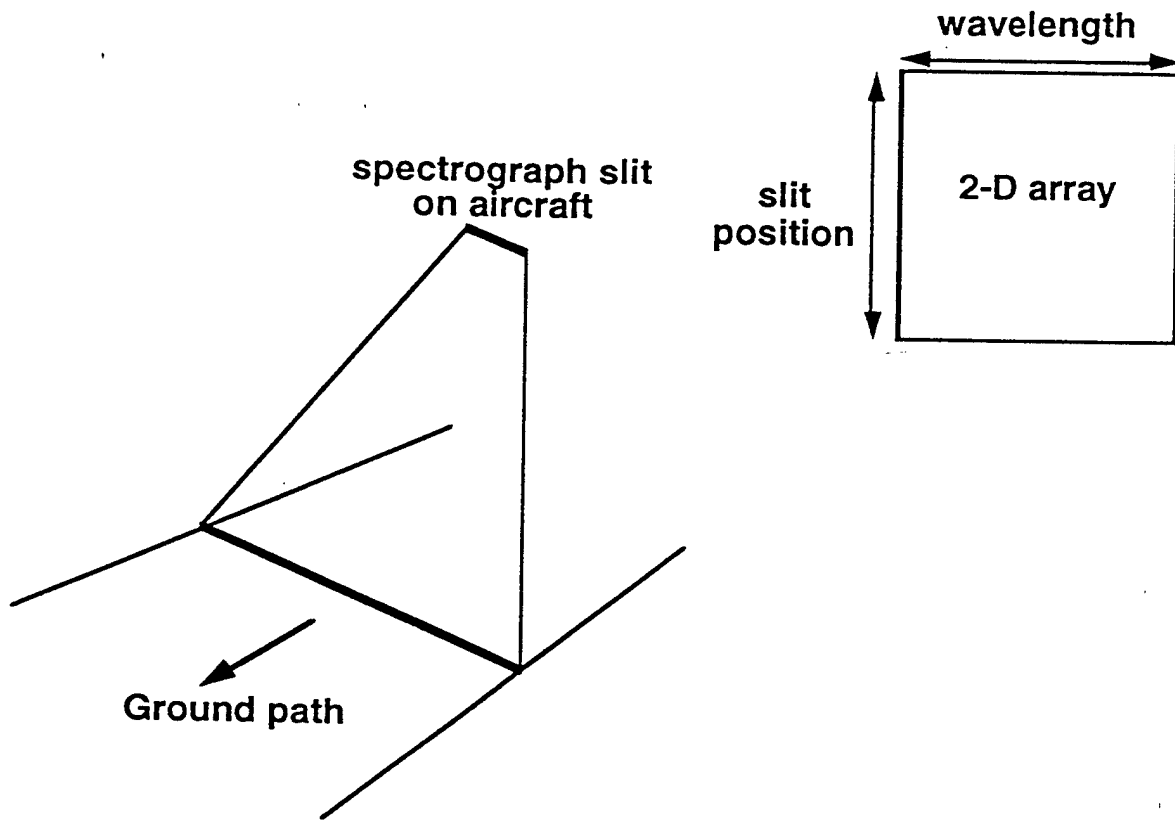


Figure 3.9. Diagram of SEBASS Pushbroom Imaging. From Hackwell, 1995.

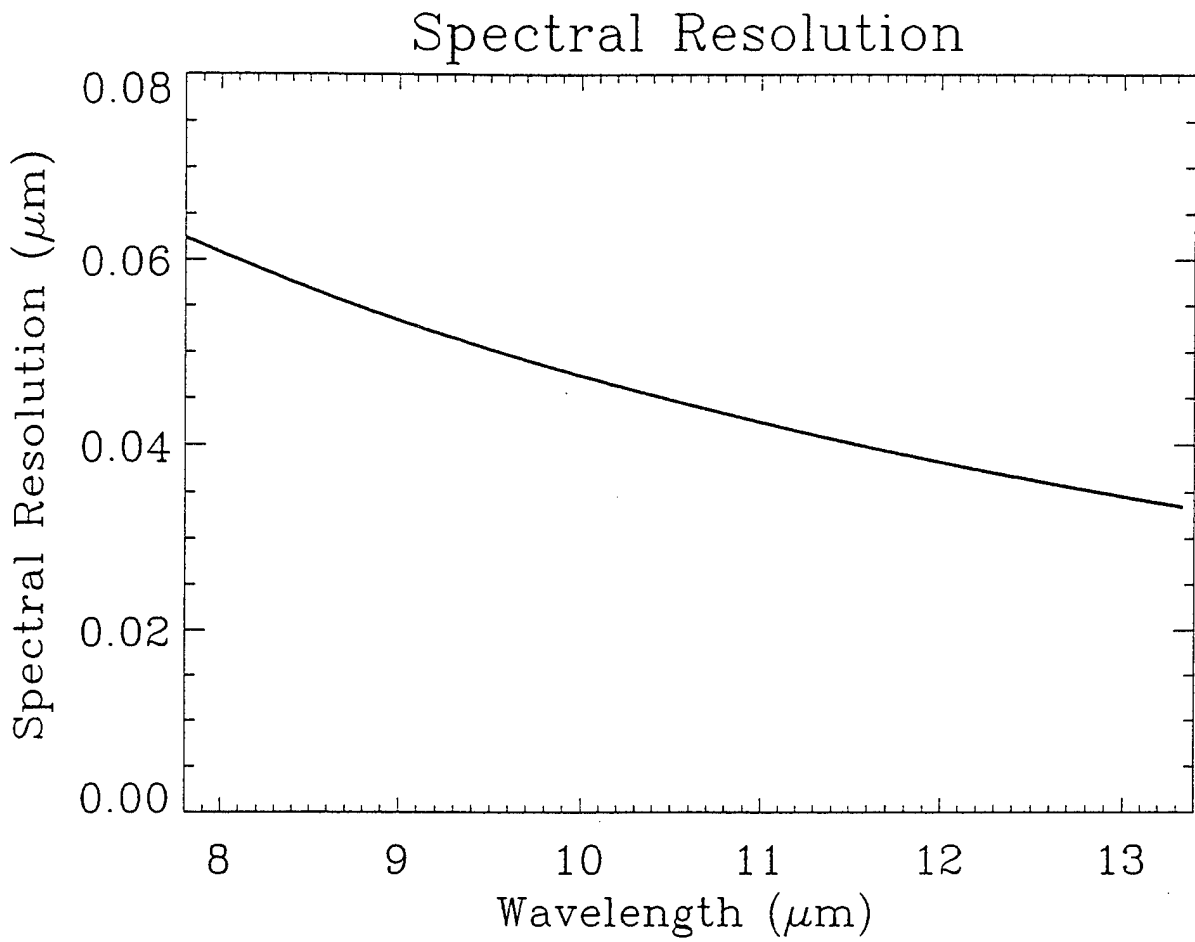


Figure 3.10. Spectral Resolution of SEBASS LWIR Channel. From Hackwell, 1995.

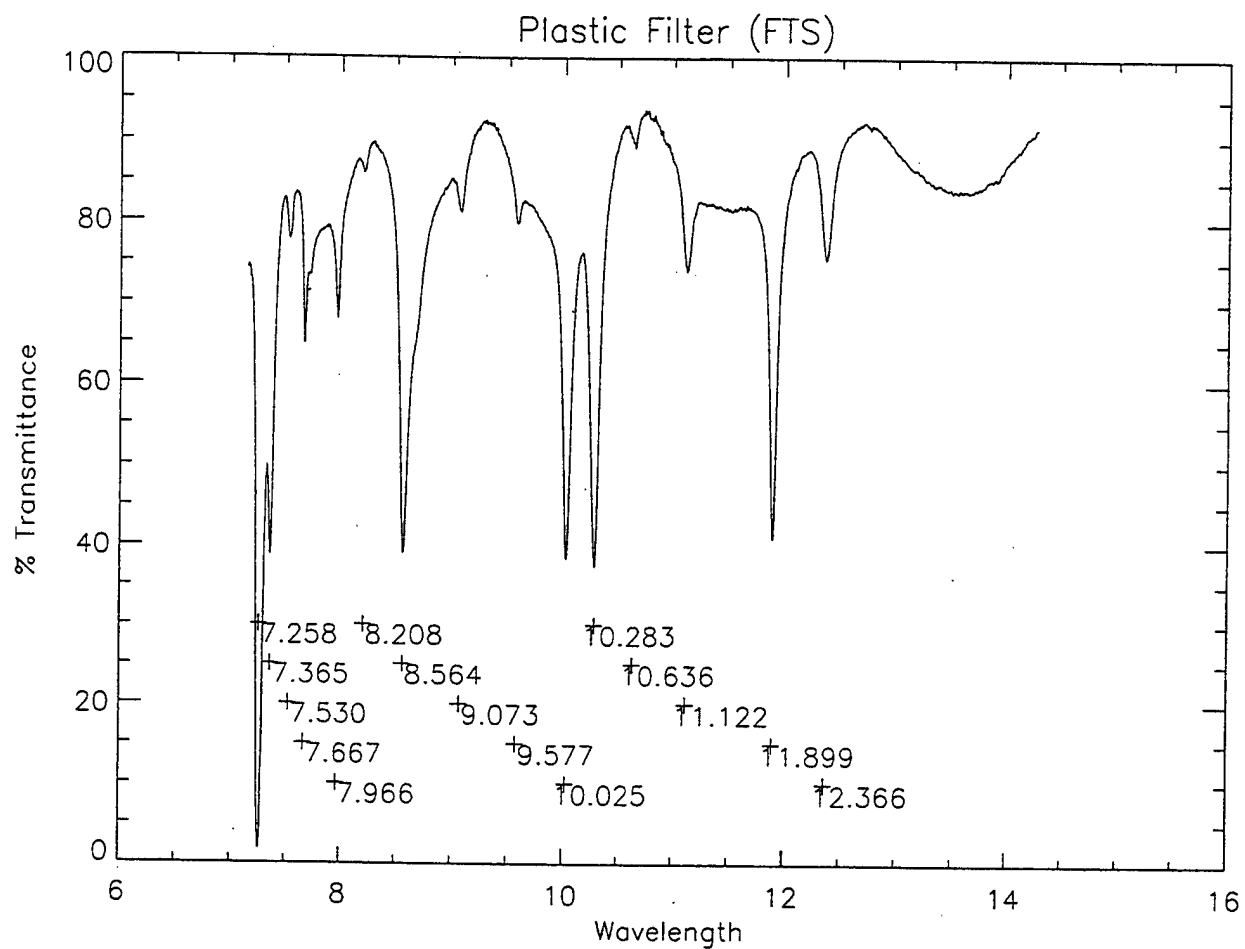
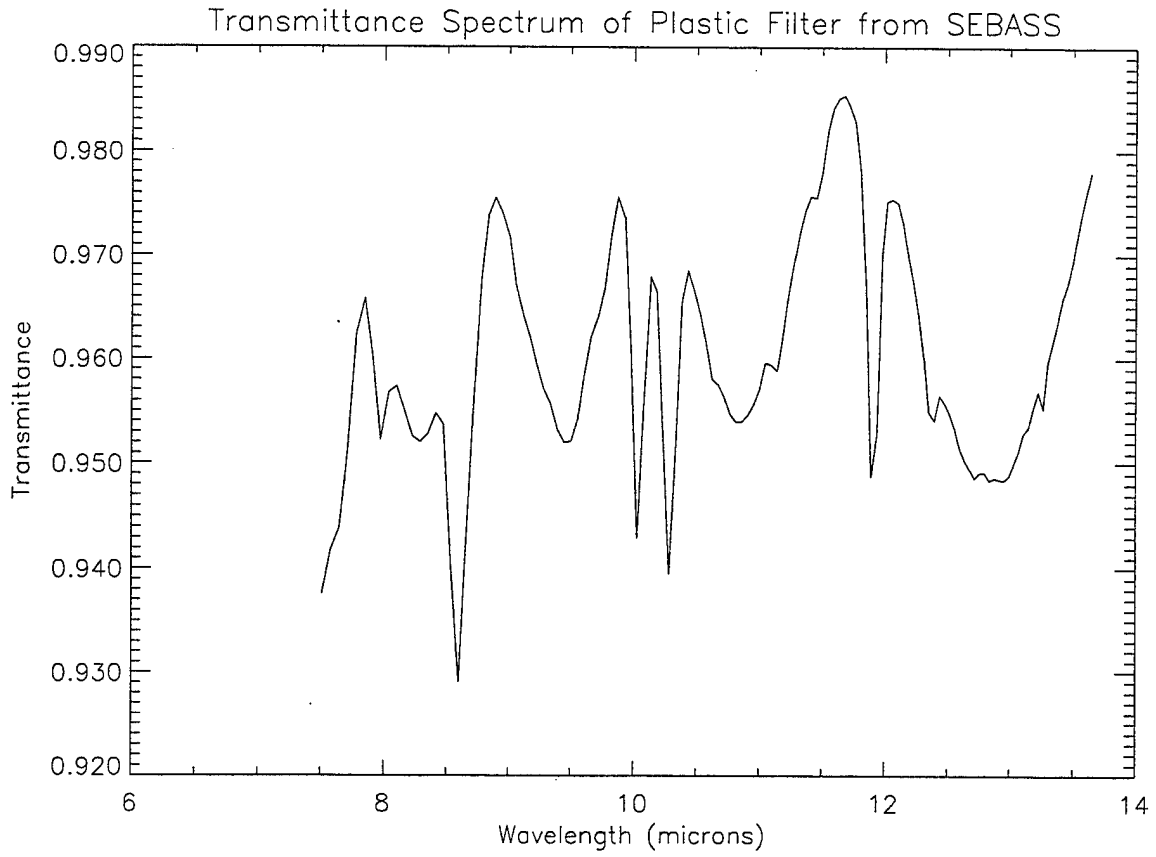


Figure 3.11. Transmittance Spectrum of Polymer Film Used for Calibration. From Bongiovi, 1996.



**Figure 3.12. Transmittance Spectrum of Polymer Film as Measured by SEBASS.**

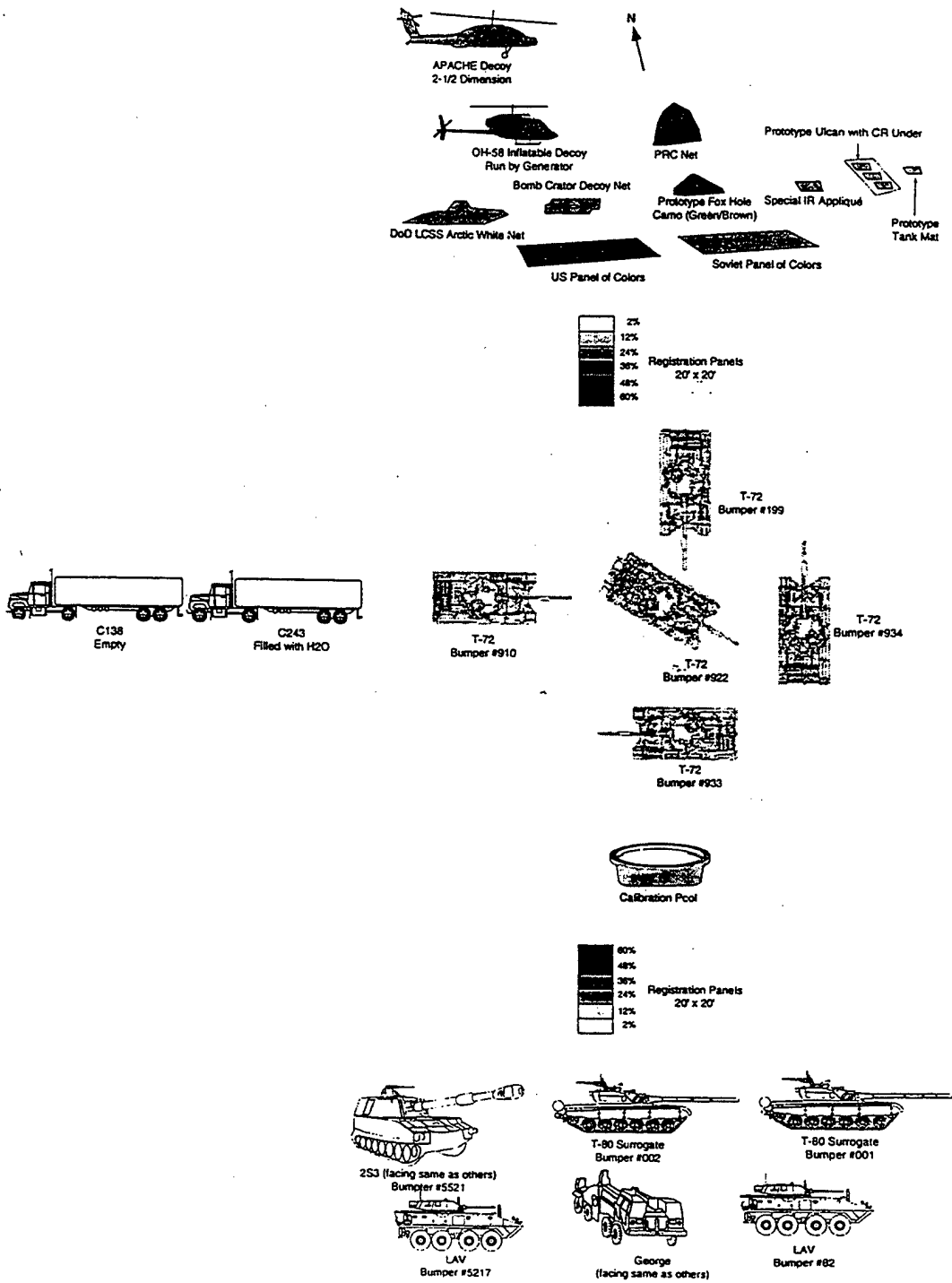


Figure 4.1. Diagram of Malpai Collection Site. From Boisjolie, 1996.

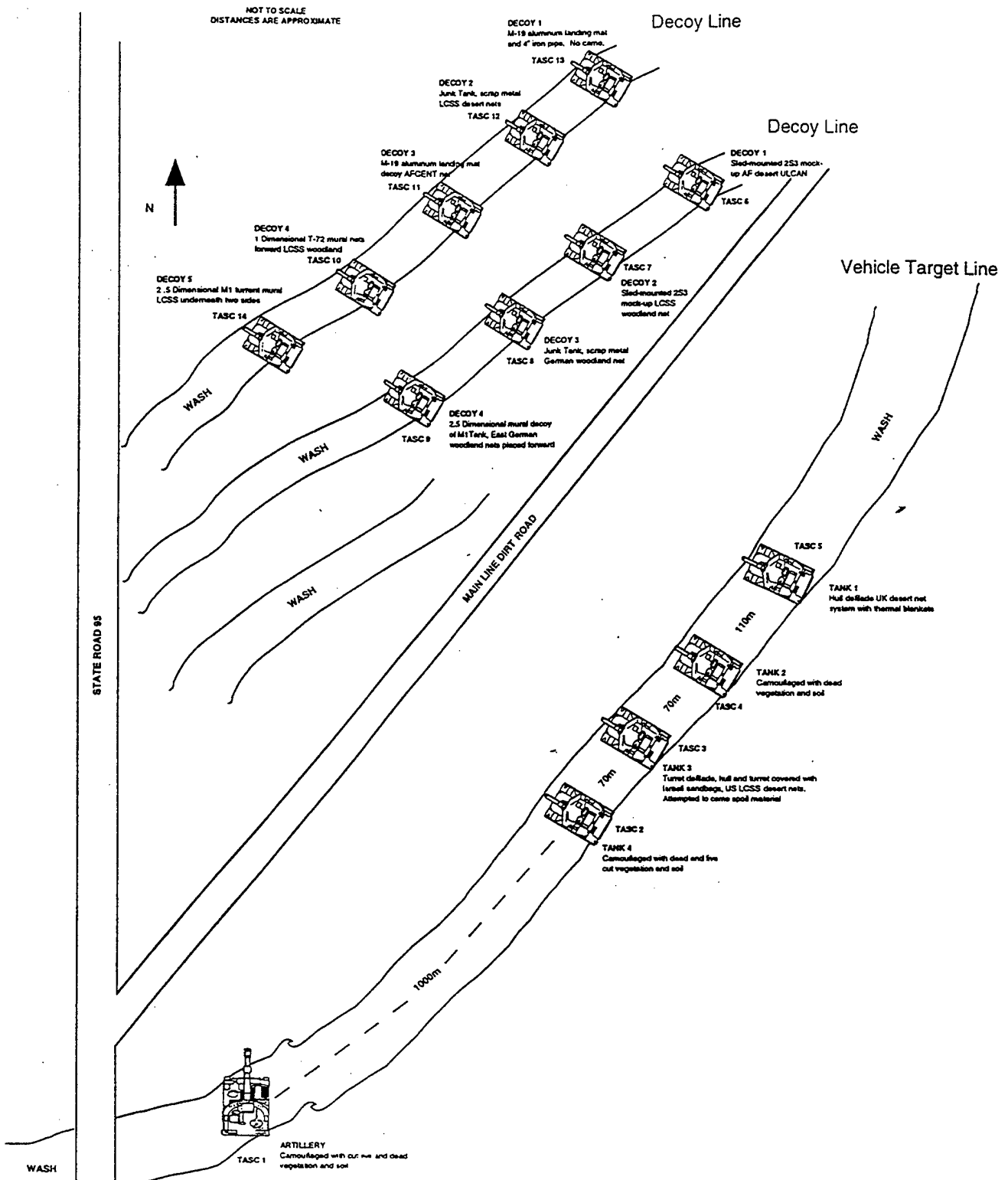


Figure 4.2. Diagram of JCCD Collection Site. From Boisjolie, 1996.

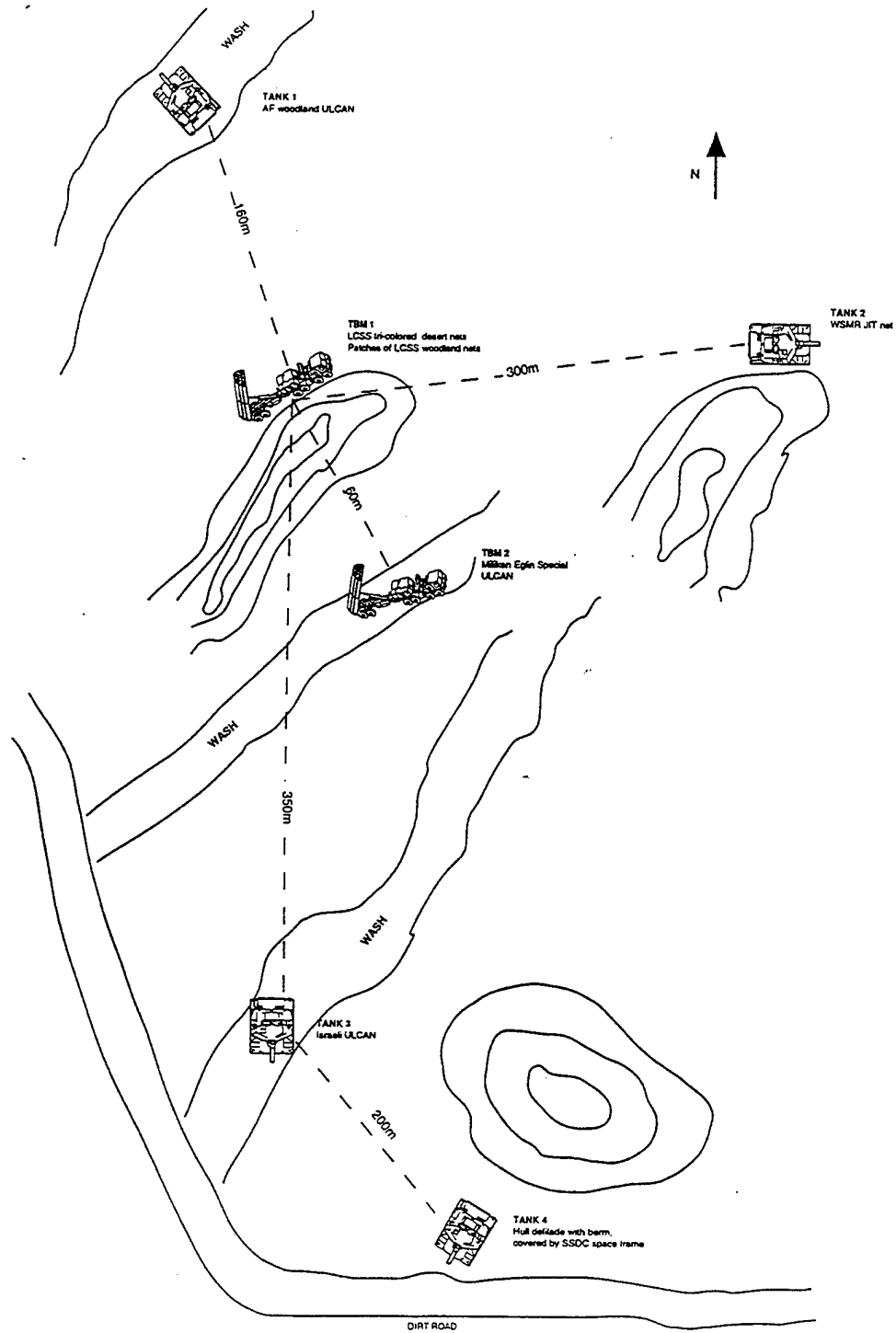


Figure 4.3. Diagram of Arroyo Collection Site. From Boisjolie, 1996.

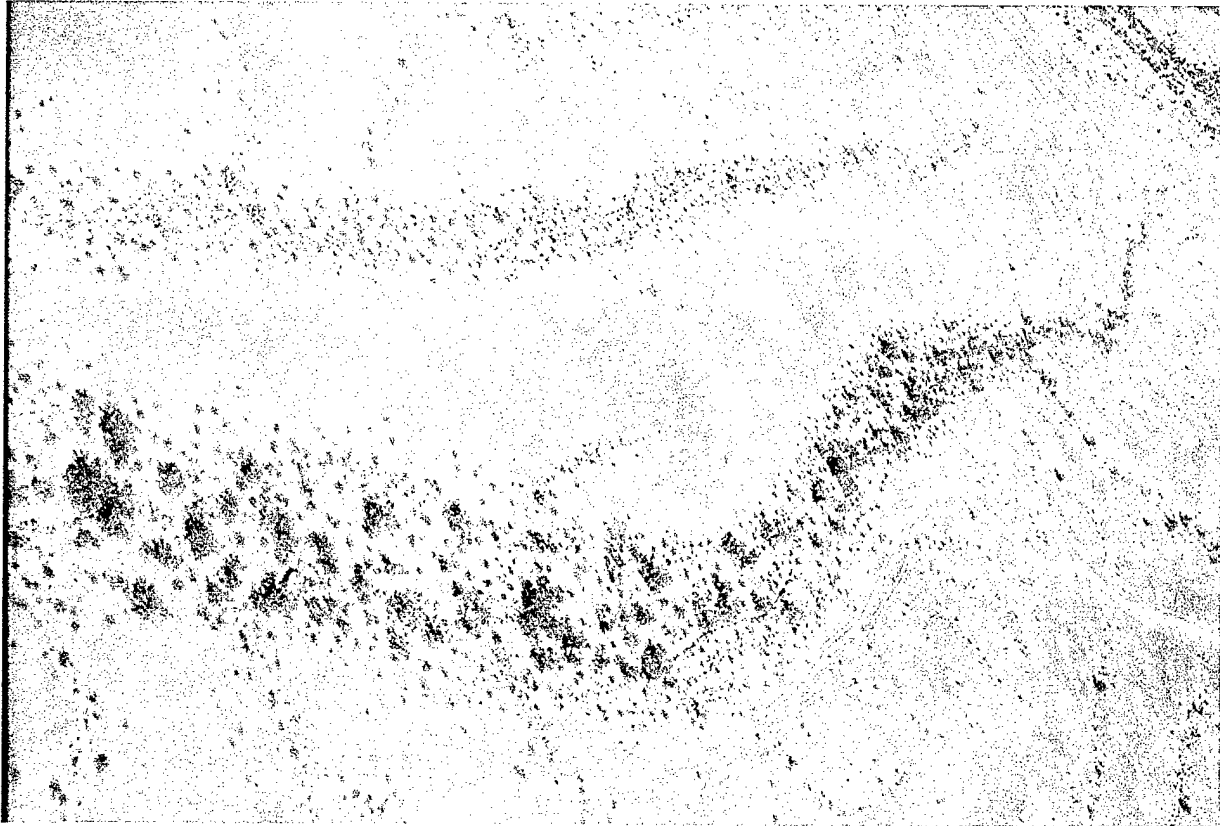


Figure 5.1. Photo of JCCD Collection Site. From WESTERN RAINBOW Photo CD, 1996.

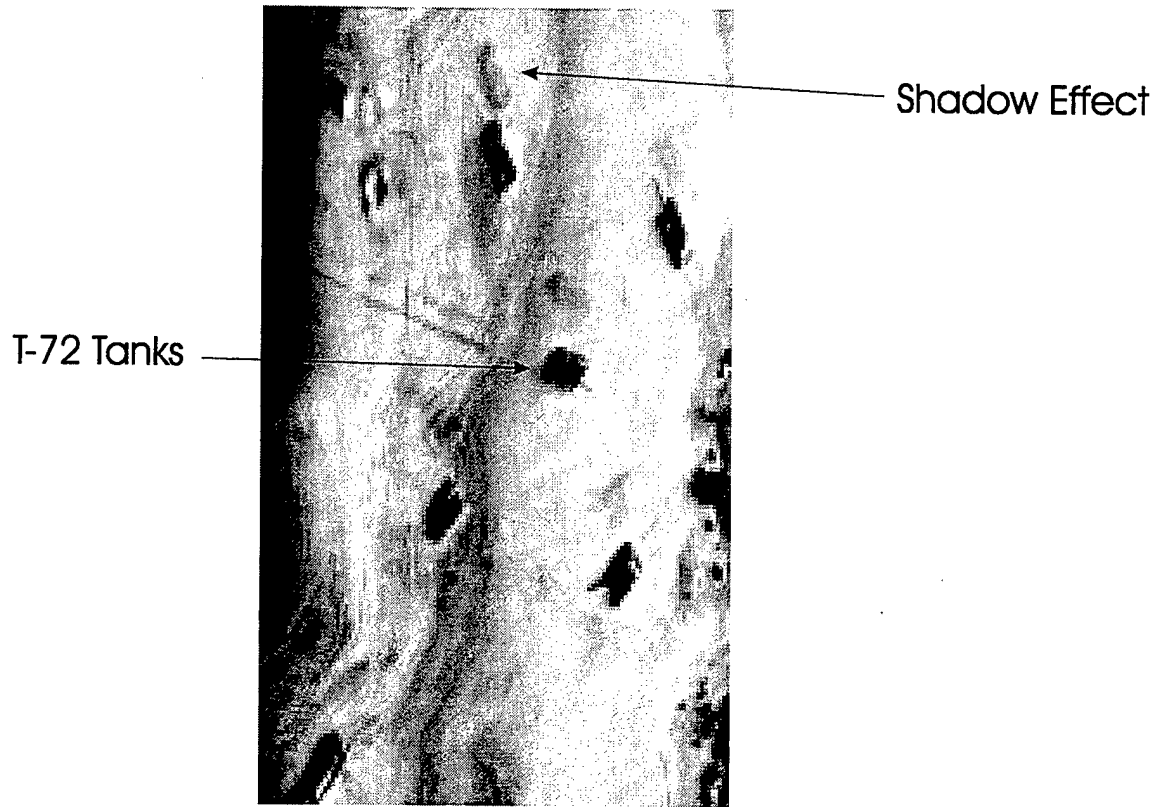


Figure 5.2. Example of SEBASS Shadow Artifact in Malpai Data Set.

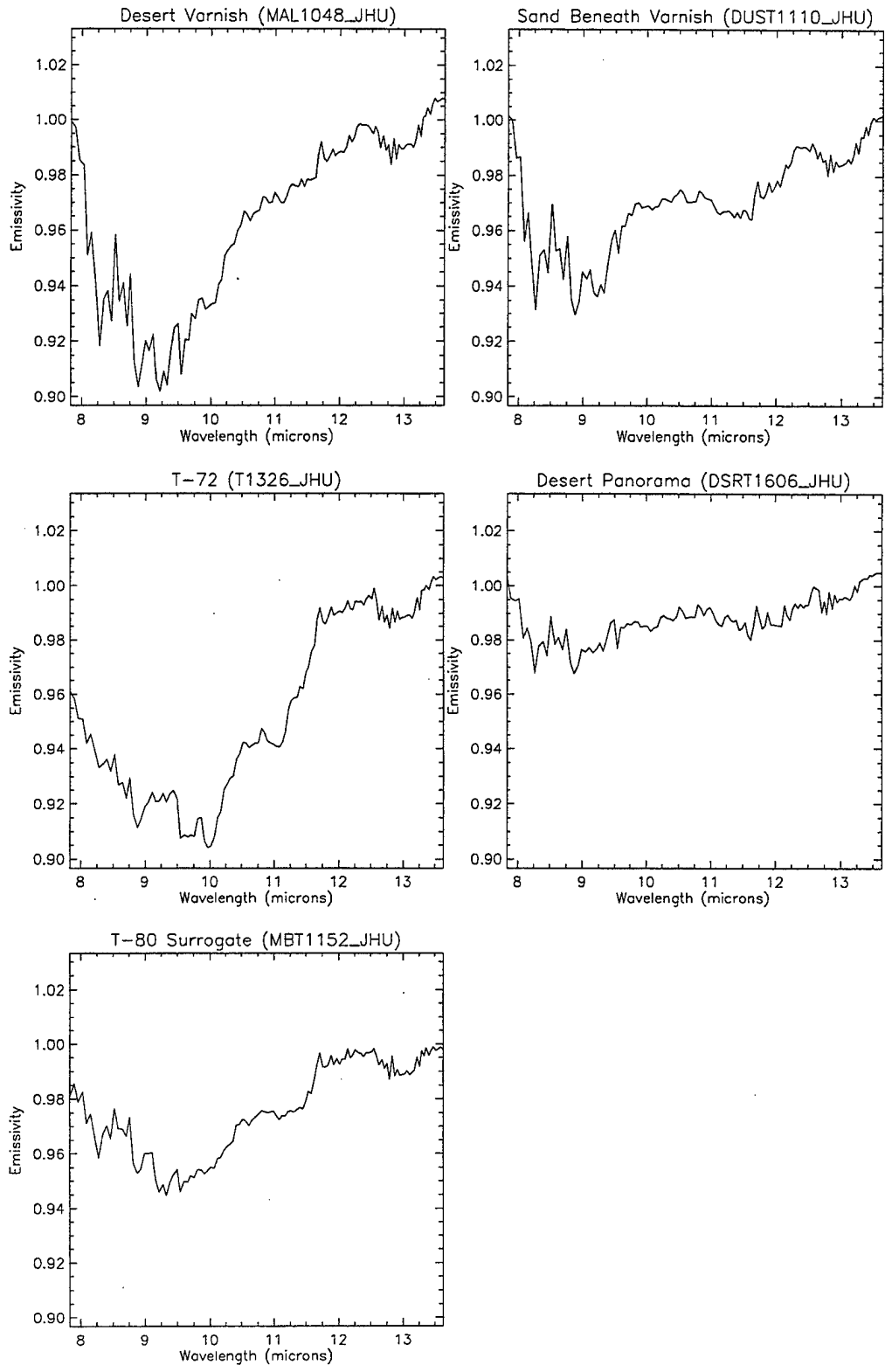


Figure 5.3. John Hopkins University Ground Truth Spectra.

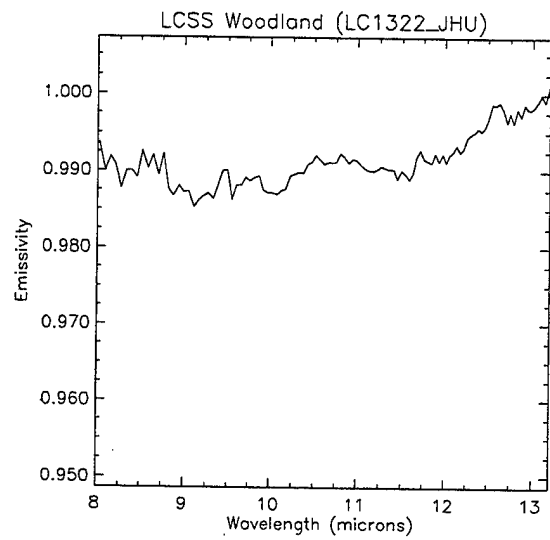
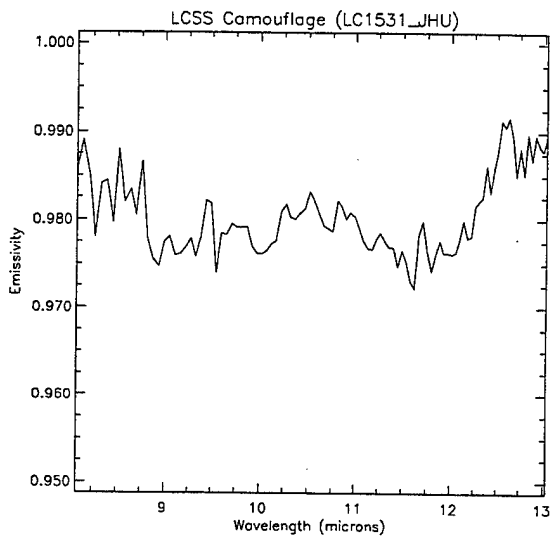
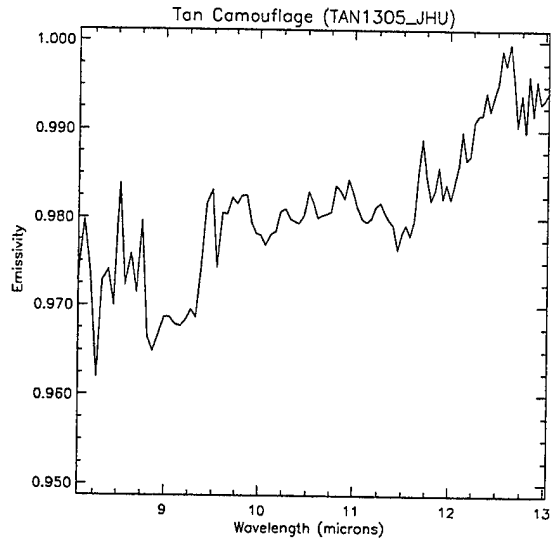
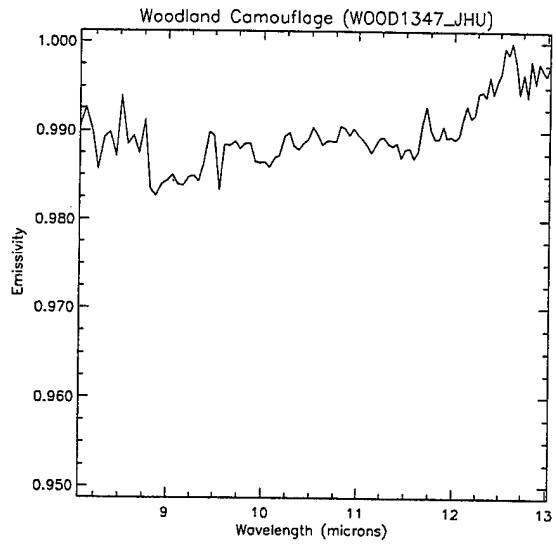


Figure 5.4. John Hopkins University Ground Truth Spectra (continued).

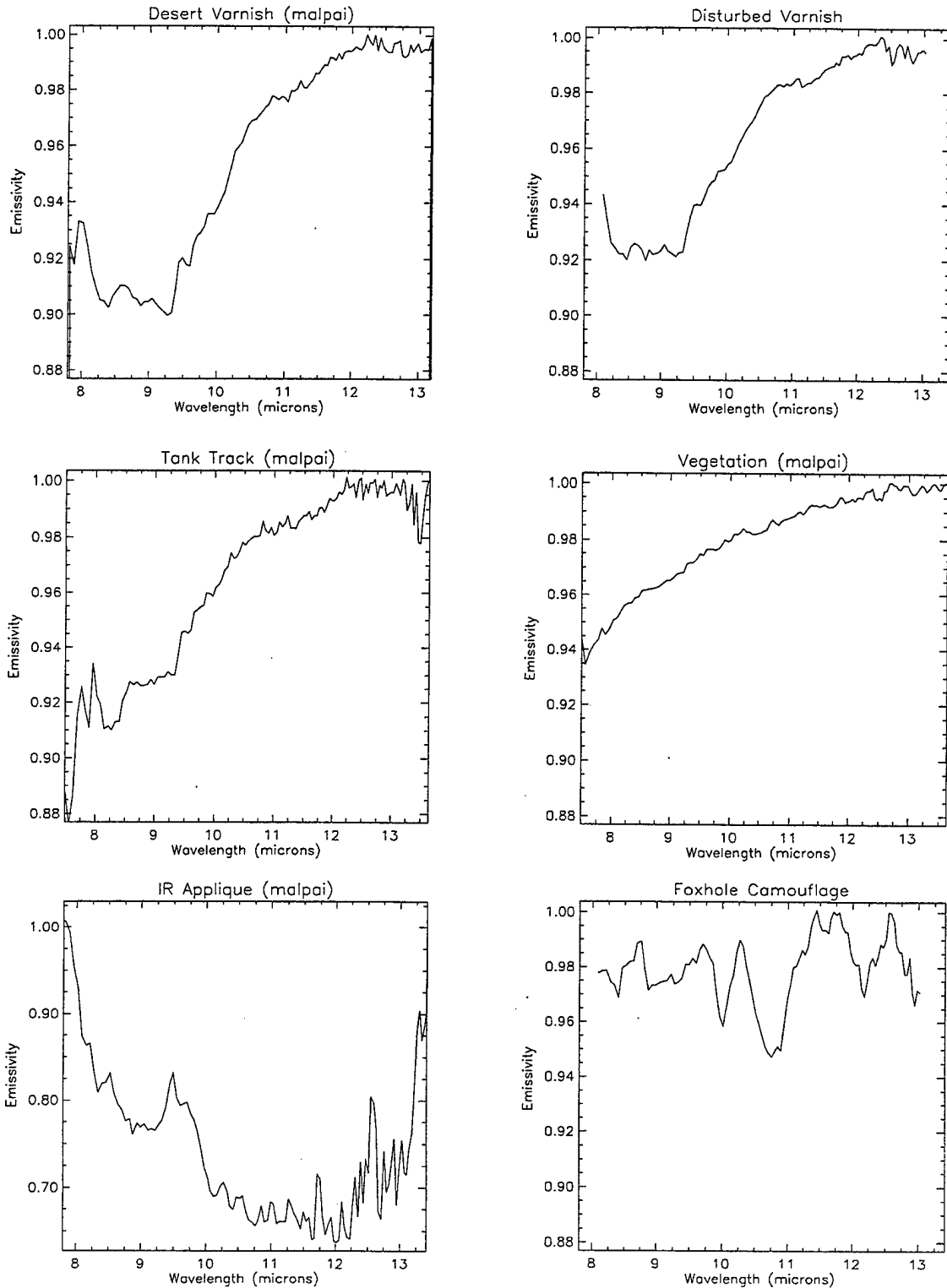


Figure 5.5. Spectra Extracted from SEBASS Data of Malpai Collection Site.

# Raw SEBASS Data

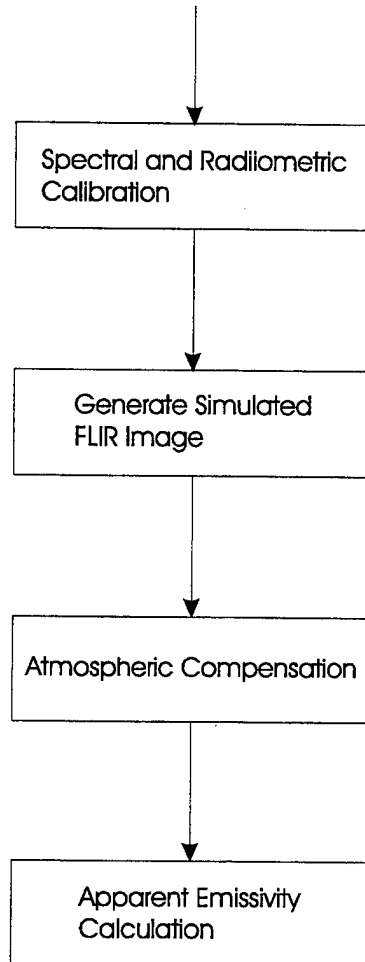
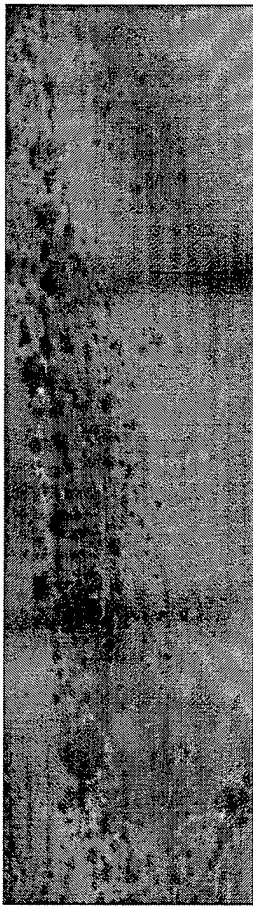
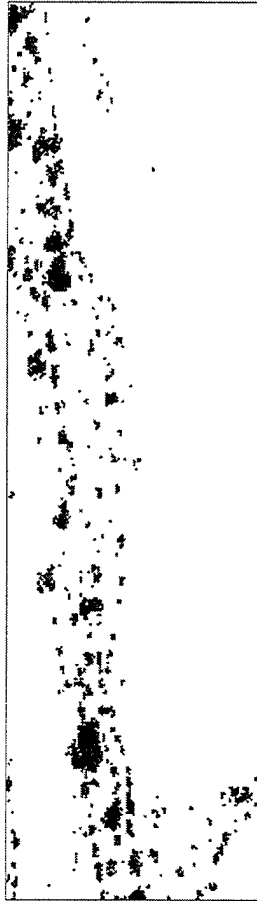


Figure 5.6. SEBASS Data Preparation Process.

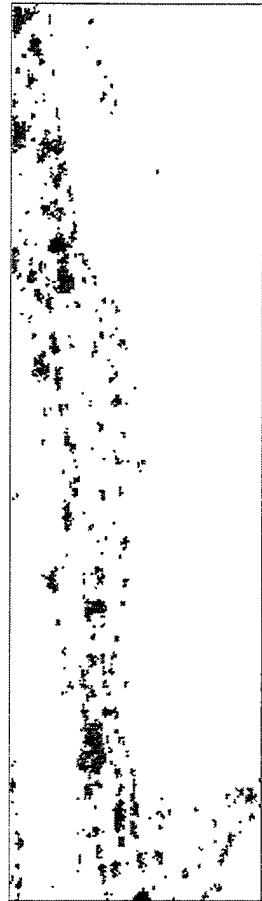


Window



All Vegetation

/sun\_data26/SEBASS/20oct95\_1000/mal5.cal



Healthy

Figure 5.7. Screening Process of Data Prior to Application of Plastic Ruler Algorithm.

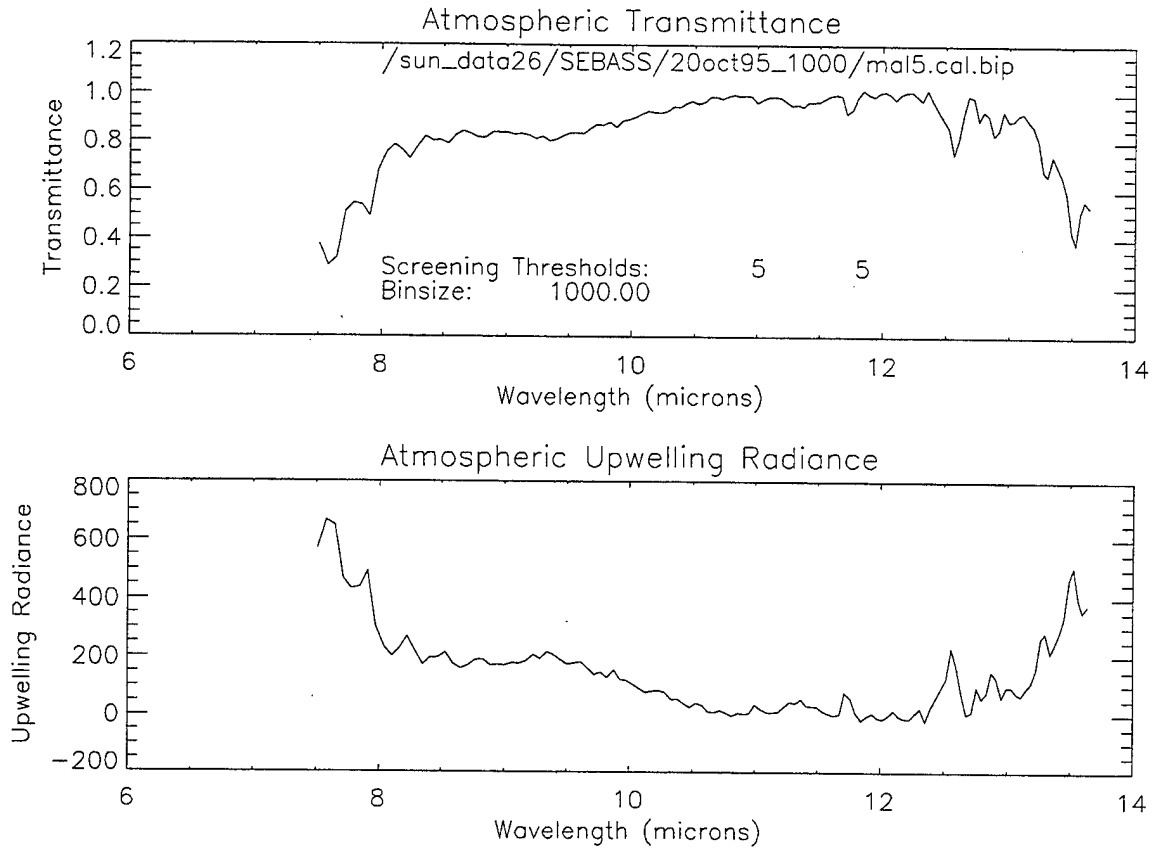


Figure 5.8. Results of Plastic Ruler Algorithm (Without Screening) on SEBASS Data Collected Over Malpai Site.

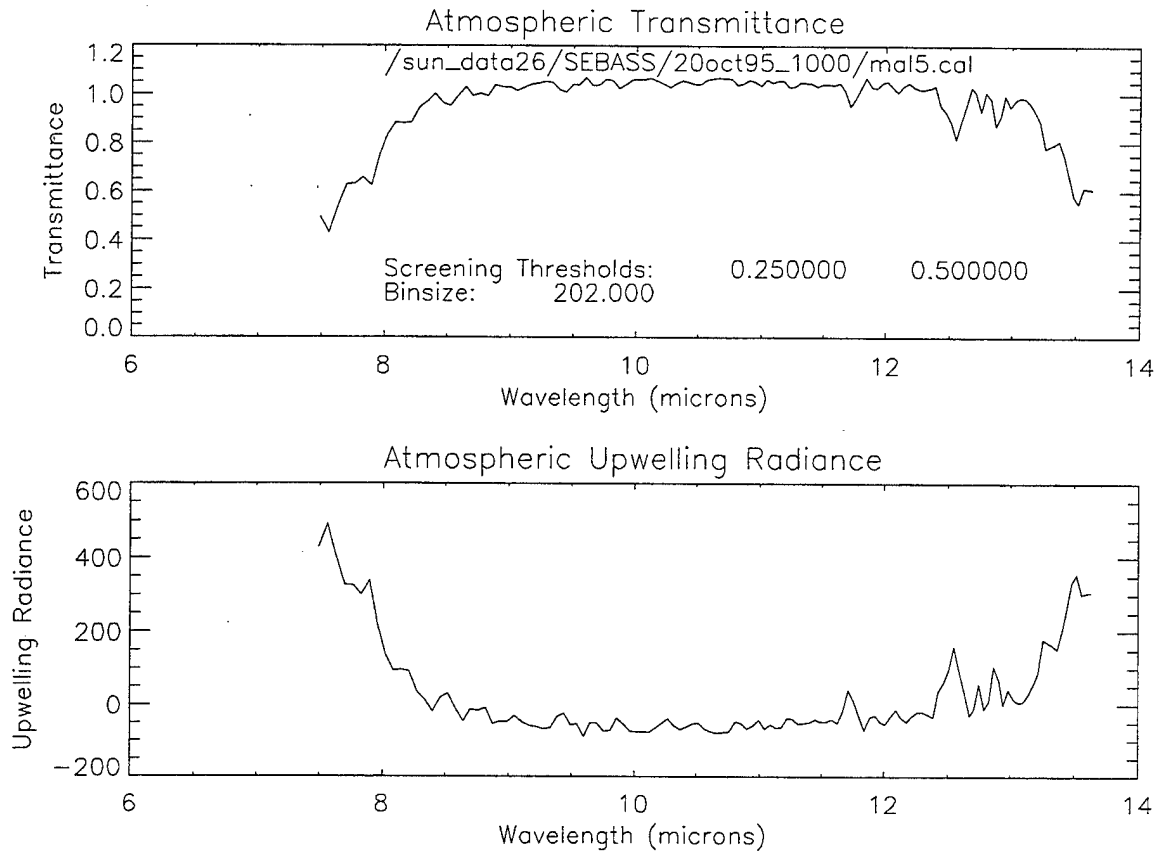


Figure 5.9. Results of Plastic Ruler Algorithm (With Screening) on SEBASS Data Collected Over Malpai Site.

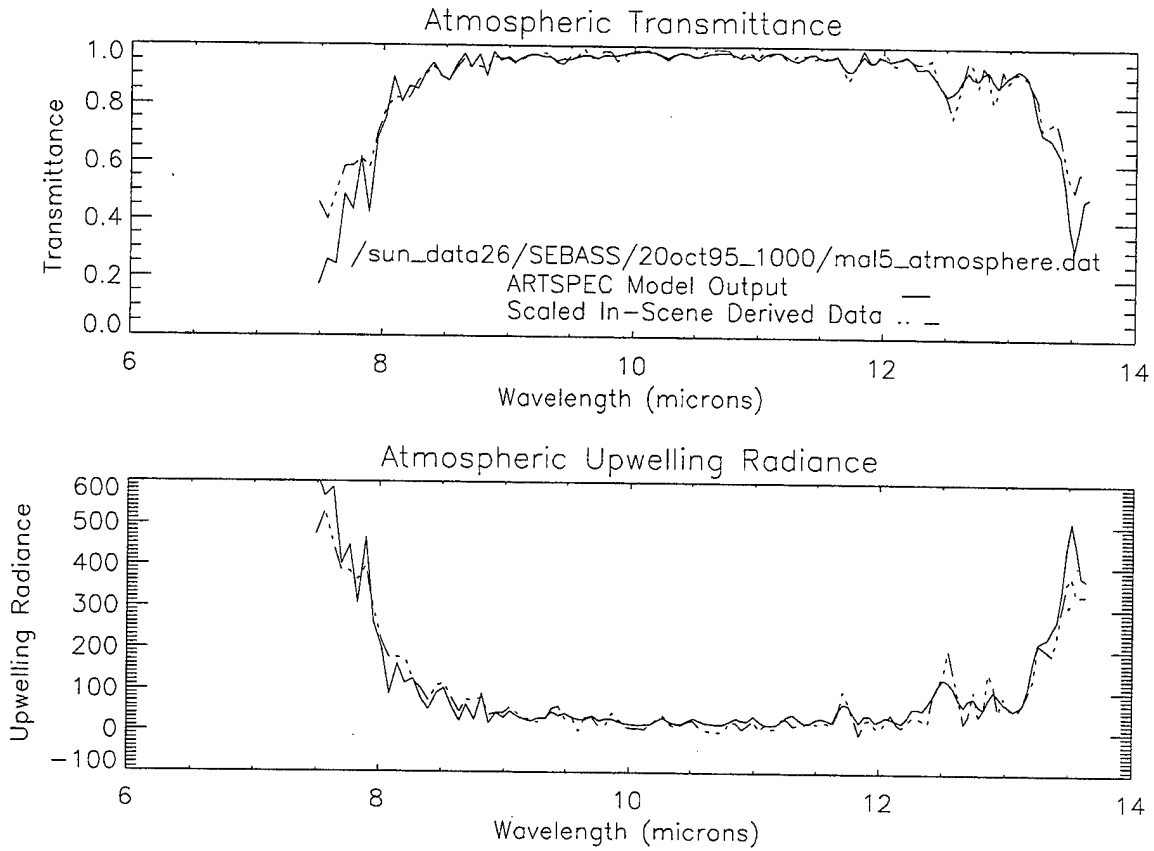


Figure 5.10. Results of ARTSPEC Fitting Routine on SEBASS Data Collected Over Malpai Site.

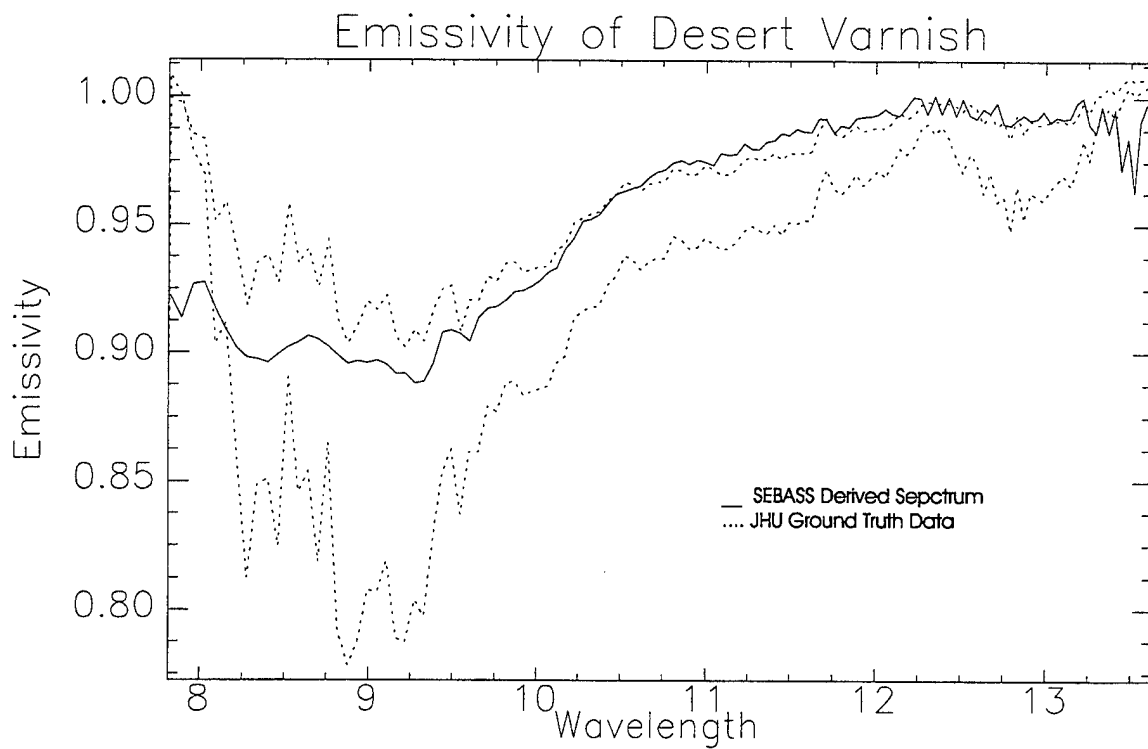


Figure 5.11. Comparison of JHU Ground Truth and SEBASS-derived Emissive Spectra.

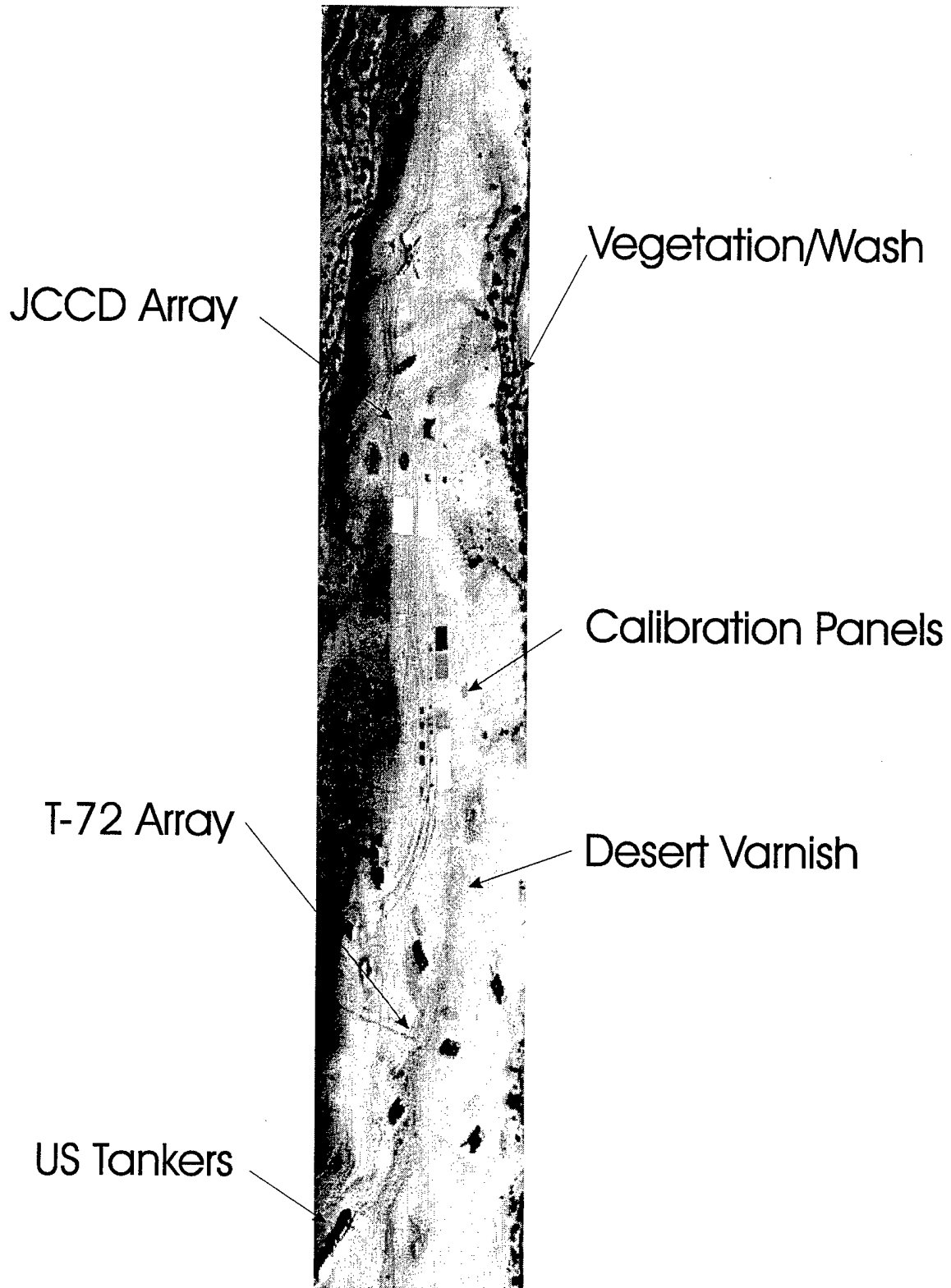


Figure 6.1. Simulated FLIR image of Malpai Collection Site, 1000 Local Time, 20 October 1995.

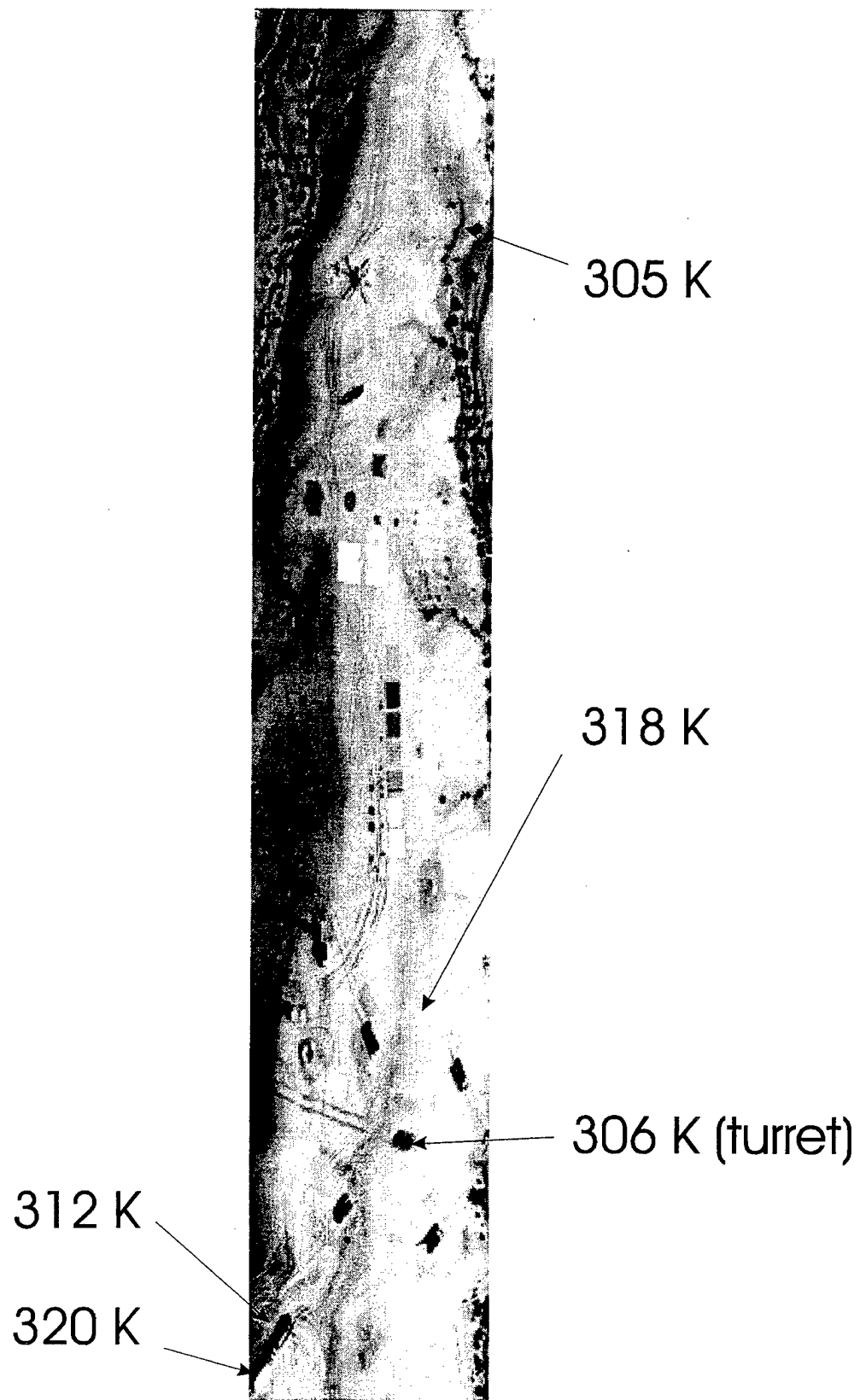


Figure 6.2. Surface Temperature Image of Malpai Collection Site, 1000 Local Time, 20 October 1995.

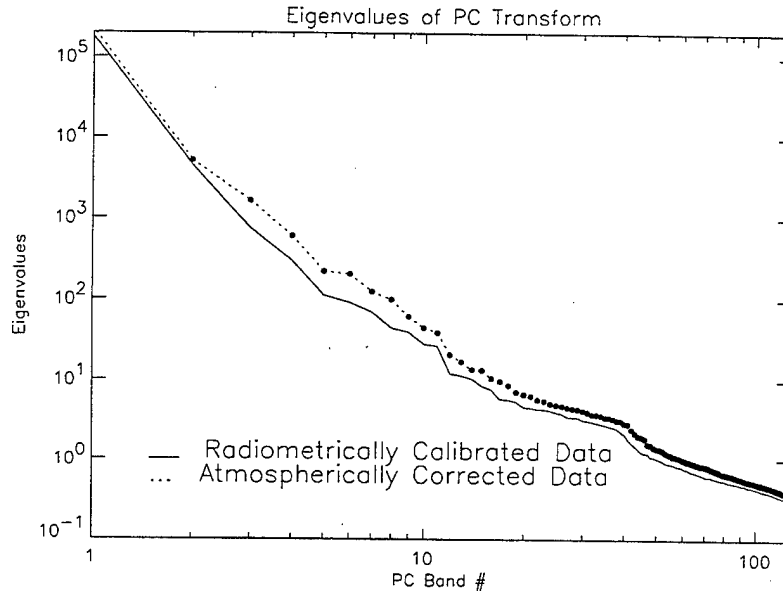


Figure 6.3. Eigenvalues of Radiometrically Calibrated Data and Atmospherically Corrected Data from Malpai Collection Site, 1000 Local Time, 20 October 1995.

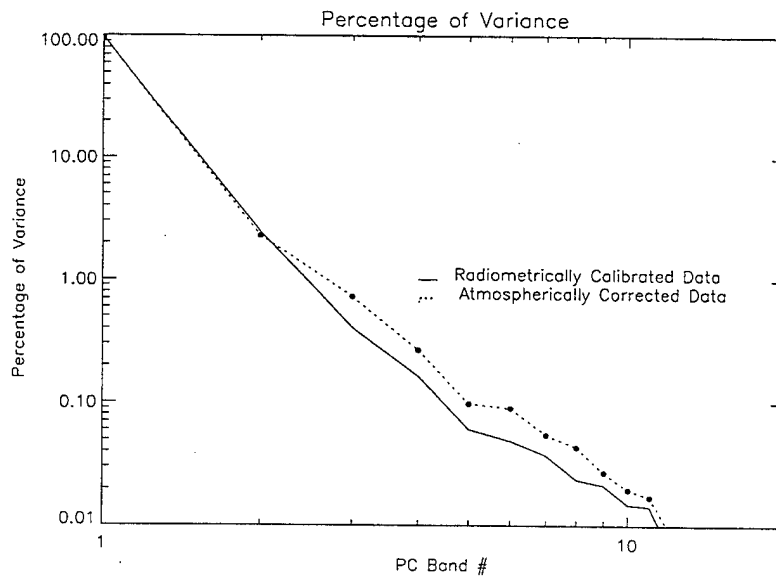
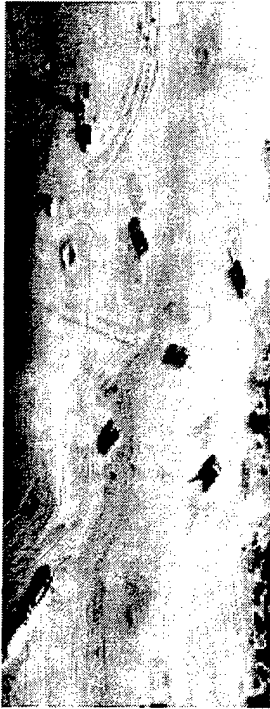


Figure 6.4. Percentage of Variance Contained in Principal Components of Radiometrically Calibrated Data and Atmospherically Corrected Data from Malpai Collection Site, 1000 Local Time, 20 October 1995.



Simulated FLIR



1st PC  
Radiometrically  
Calibrated



1st PC  
Atmospherically  
Corrected

Figure 6.5. Comparison of Simulated FLIR Image with First Principal Component Image of Radiometrically Calibrated Data and First Principal Component Image of Atmospherically Corrected Data from Malpai Collection Site, 1000 Local Time, 20 October 1995.

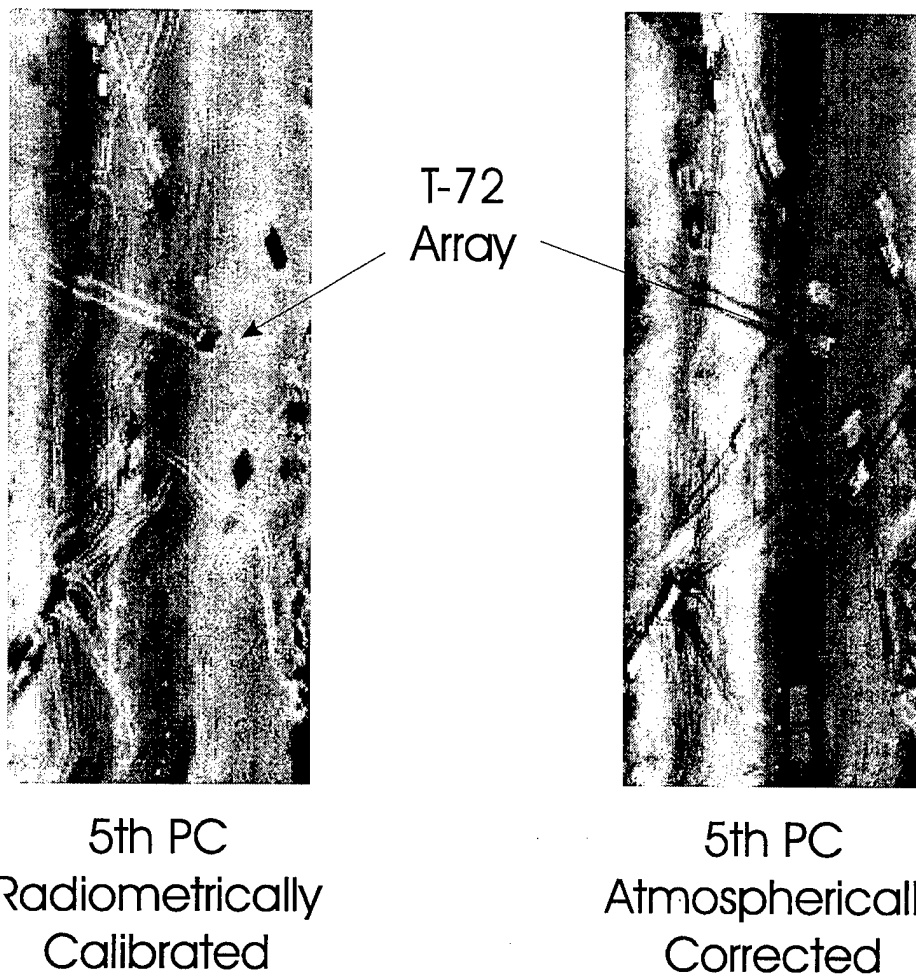


Figure 6.6. Comparison Between Fifth Principal Component Image of Radiometrically Calibrated Data and Fifth Principal Component Image of Atmospherically Corrected Data from Malpai Collection Site, 1000 Local Time, 20 October 1995.



Simulated FLIR

Tank Tracks



2nd PC  
Radiometrically  
Calibrated

Figure 6.7. Comparison Between Simulated FLIR Image and Second Principal Component Image of Radiometrically Calibrated Data from Malpai Collection Site, 1000 Local Time, 20 October 1995.

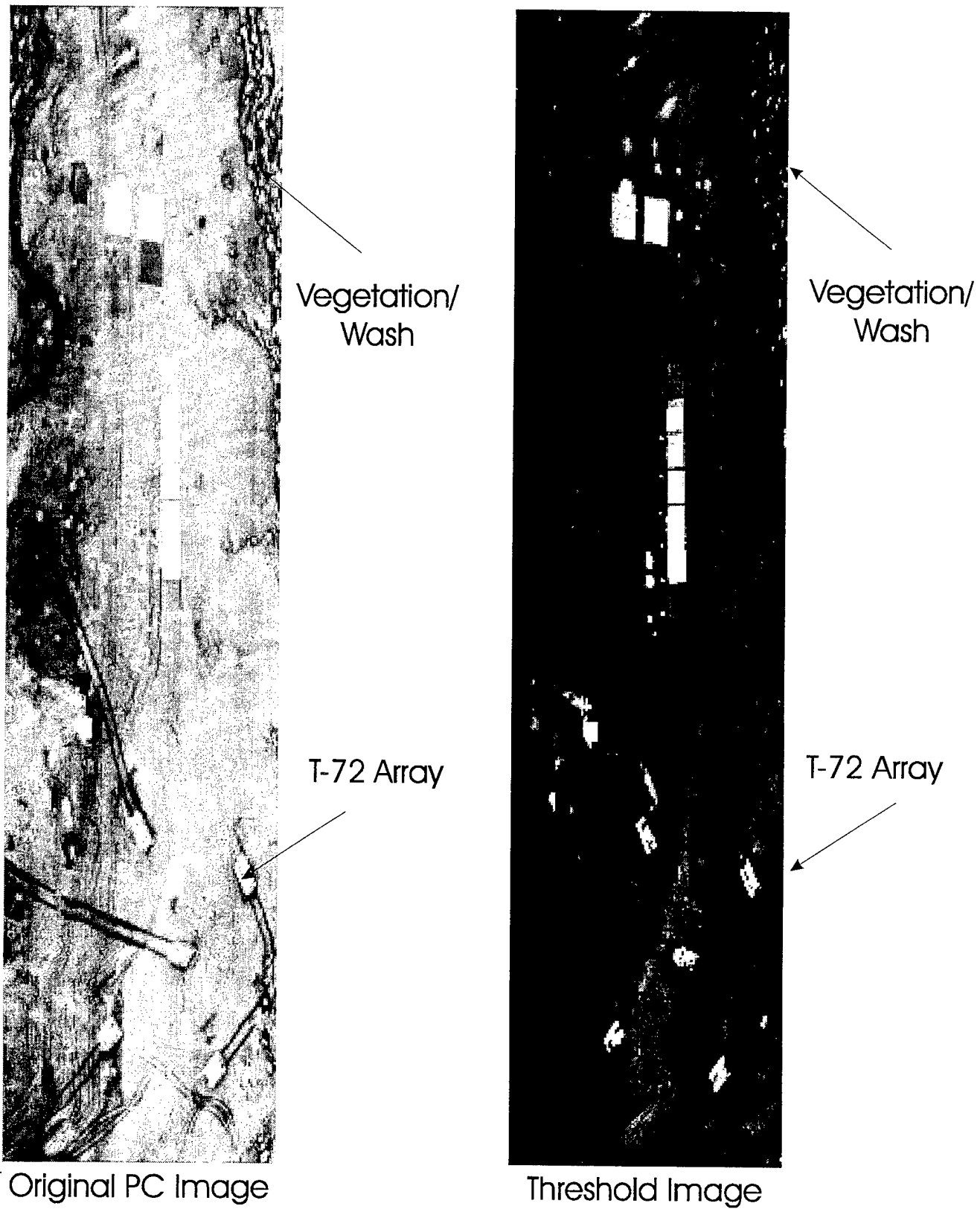


Figure 6.8. Third Principal Component Image of Radiometrically Calibrated Data from Malpai Collection Site, 1000 Local Time, 20 October 1995.

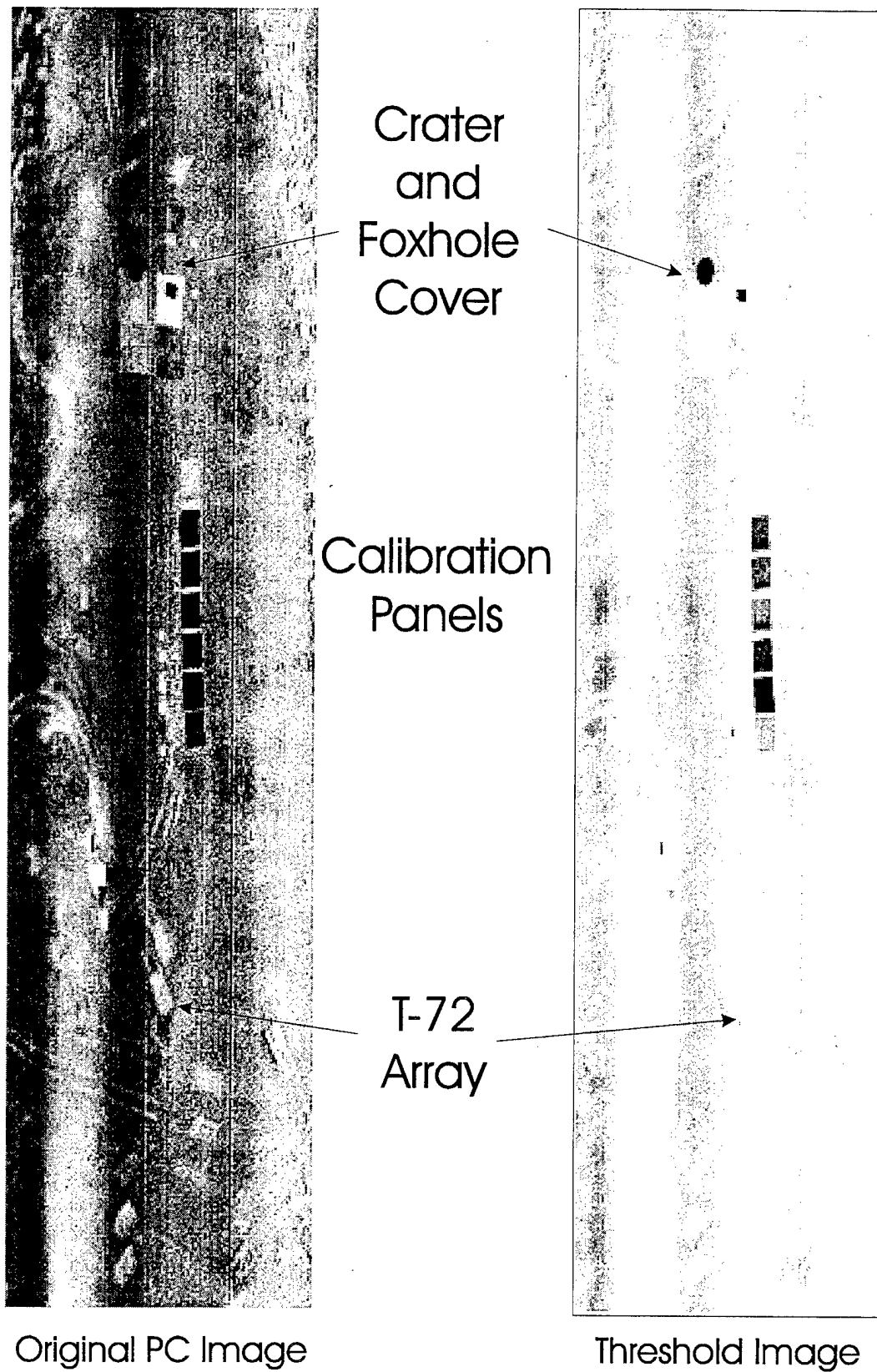


Figure 6.9. Eighth Principal Component Image of Radiometrically Calibrated data from Malpai Collection Site, 1000 Local Time, 20 October 1995.

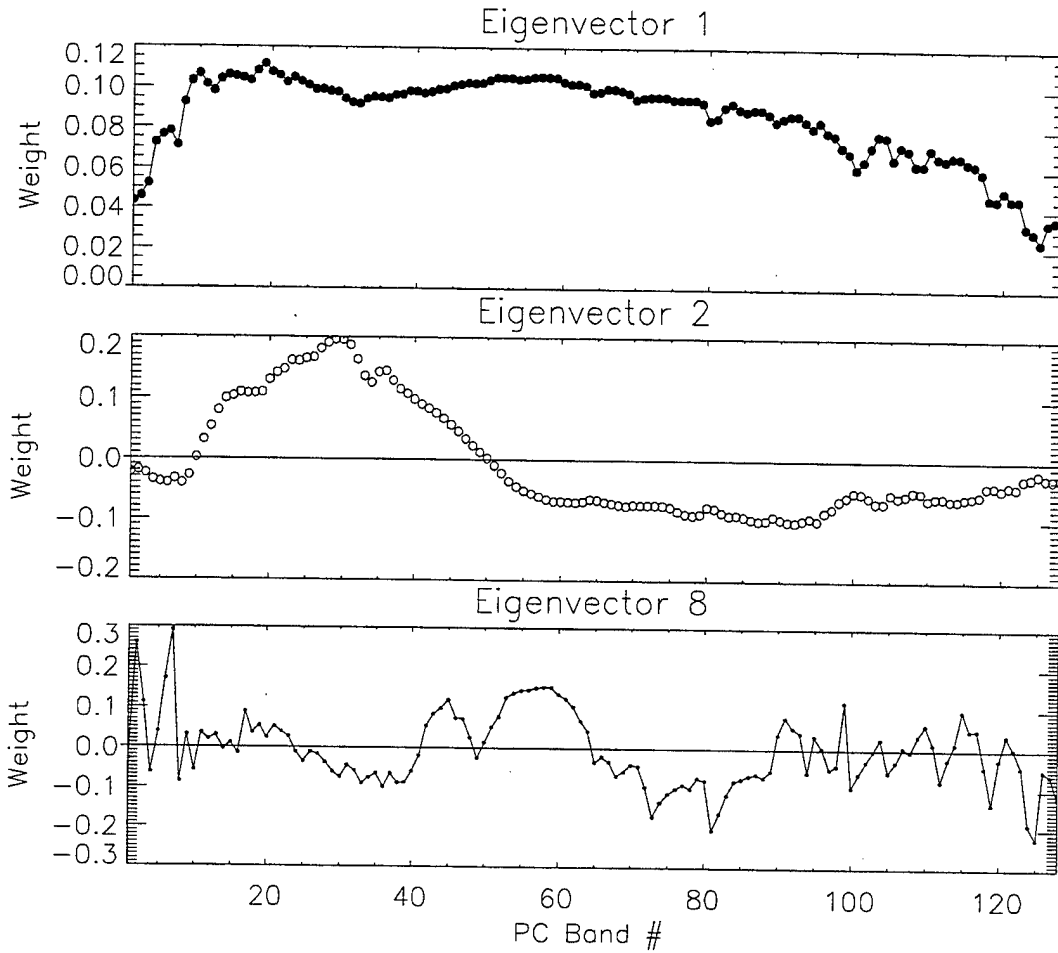


Figure 6.10. Weighting of Spectral Bands to Generate Principal Components One, Two, and Eight of Malpai Collection Site, 1000 Local Time, 20 October 1995.

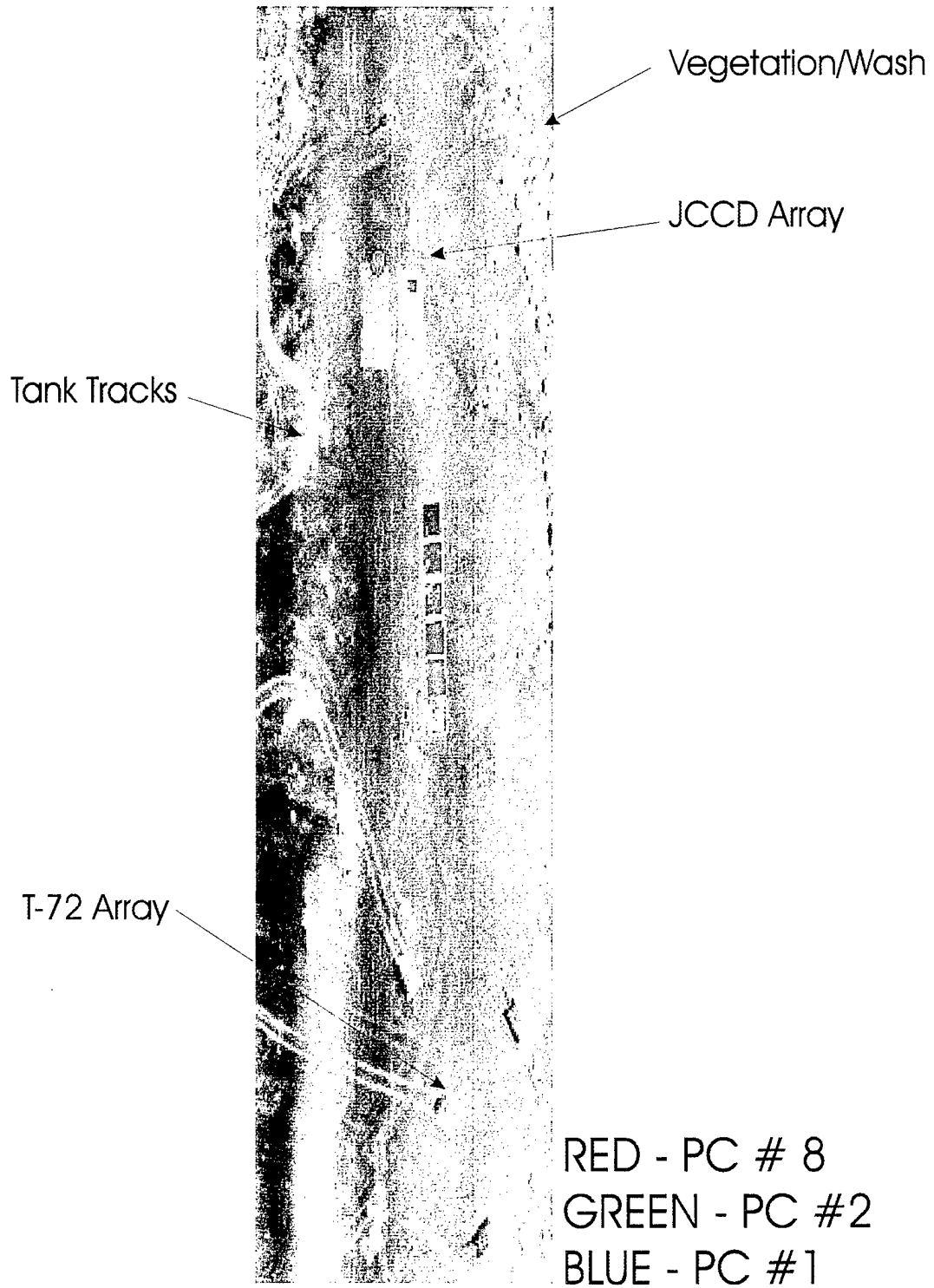


Figure 6.11. Red-Green-Blue Principal Component Image of Radiometrically Calibrated Data from Malpai Collection Site, 1000 Local Time, 20 October 1995.

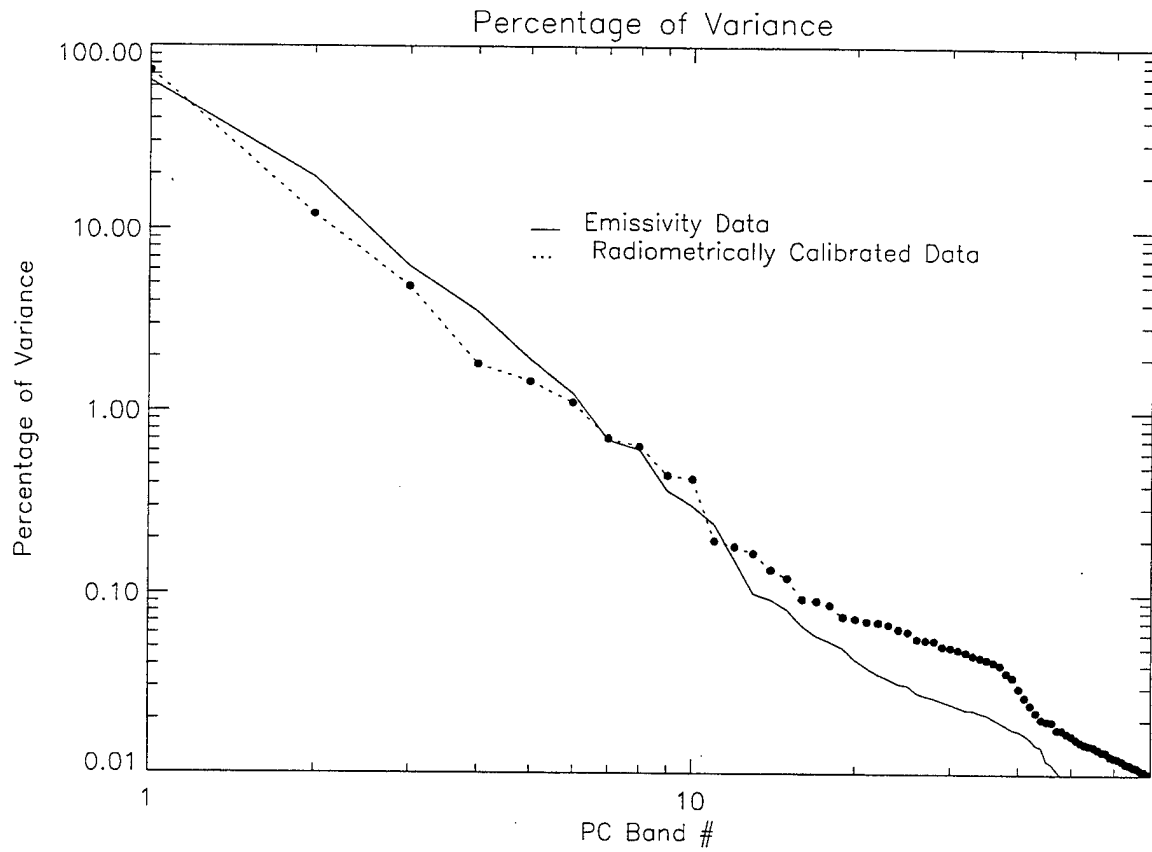


Figure 6.12. Percentage of Variance Contained in Principal Components of Emissivity data and Radiometrically Calibrated Data from Malpai Collection Site, 1000 Local Time, 20 October 1995.

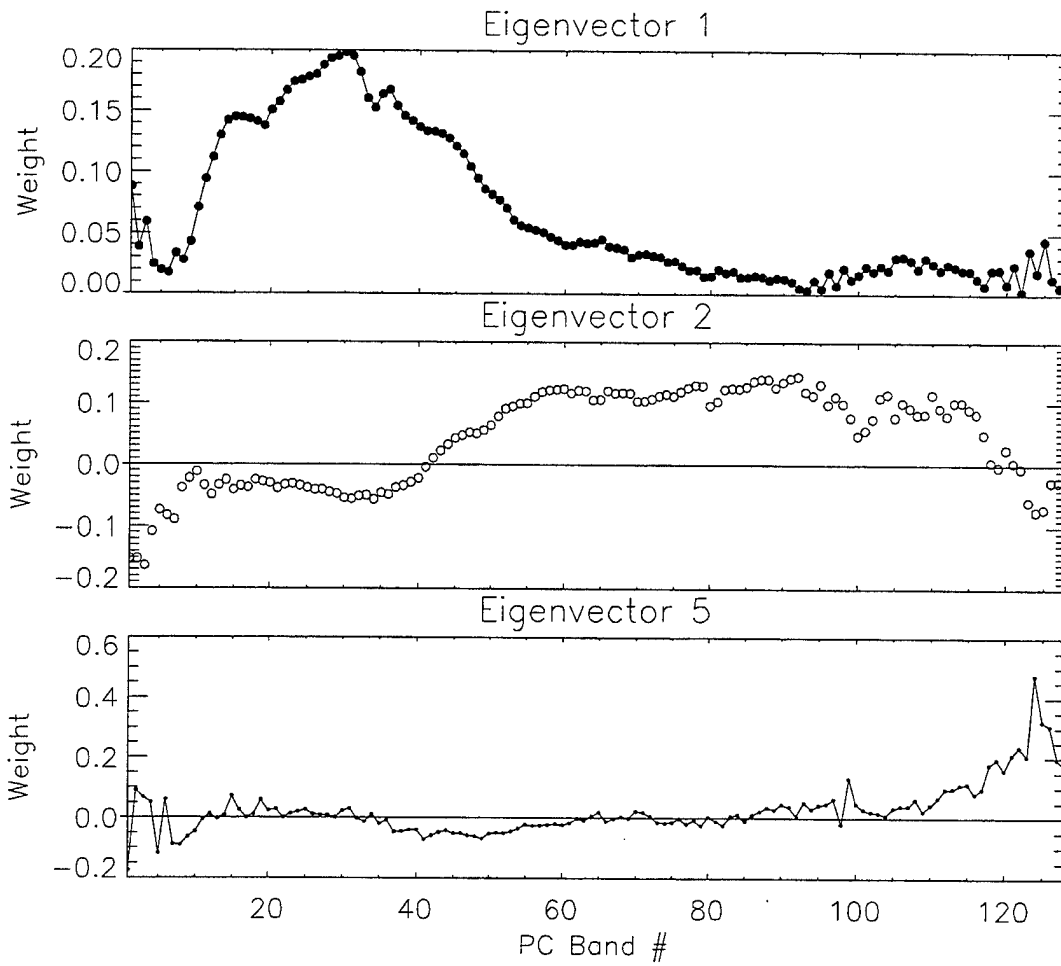


Figure 6.13. Weighting of Spectral Bands to Generate Principal Components One, Two, and Five of Malpai Collection Site, 1000 Local Time, 20 October 1995.

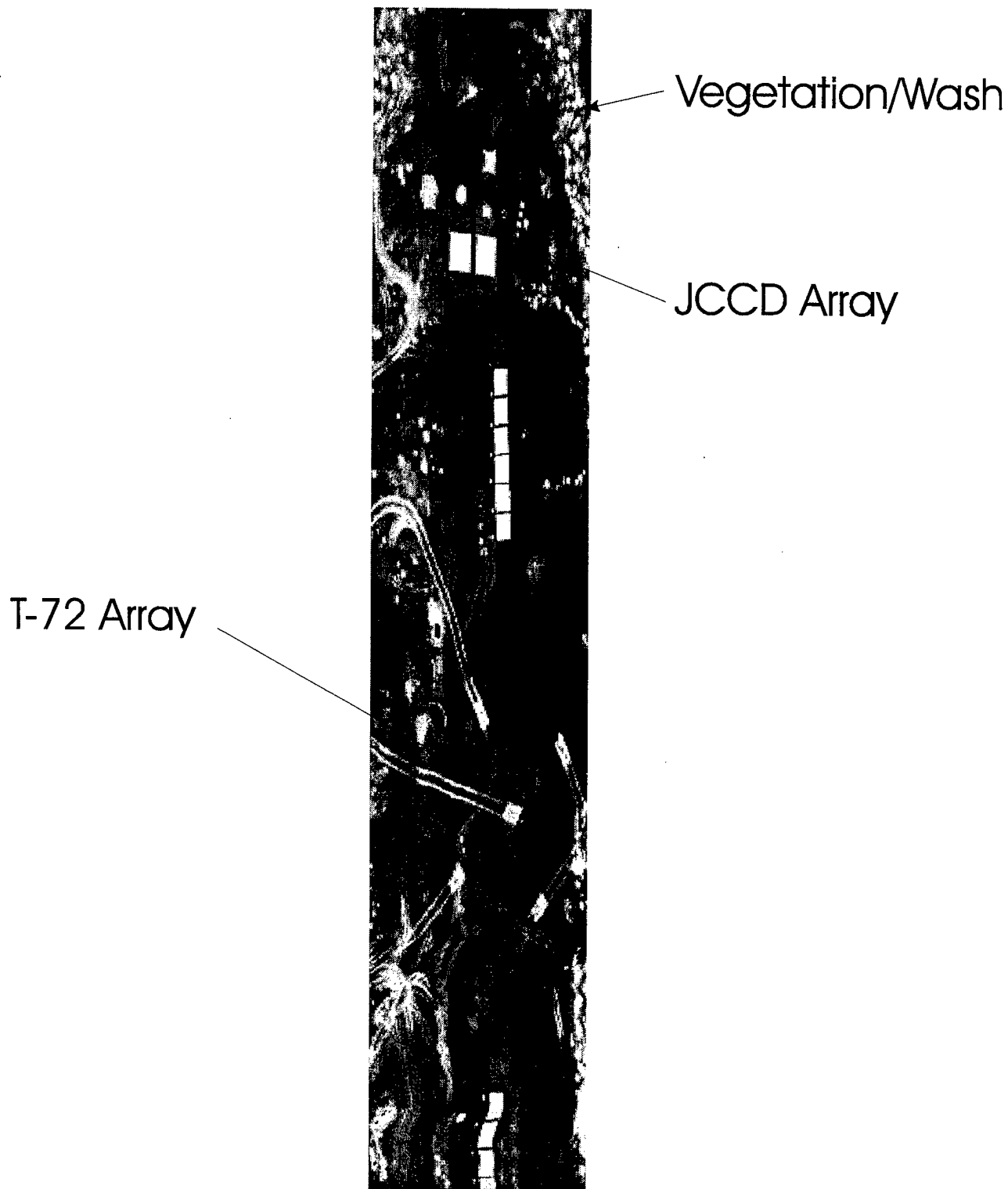


Figure 6.14. First Principal Component Image of Emissivity Data from Malpai Collection Site, 1000 Local Time, 20 October 1995.

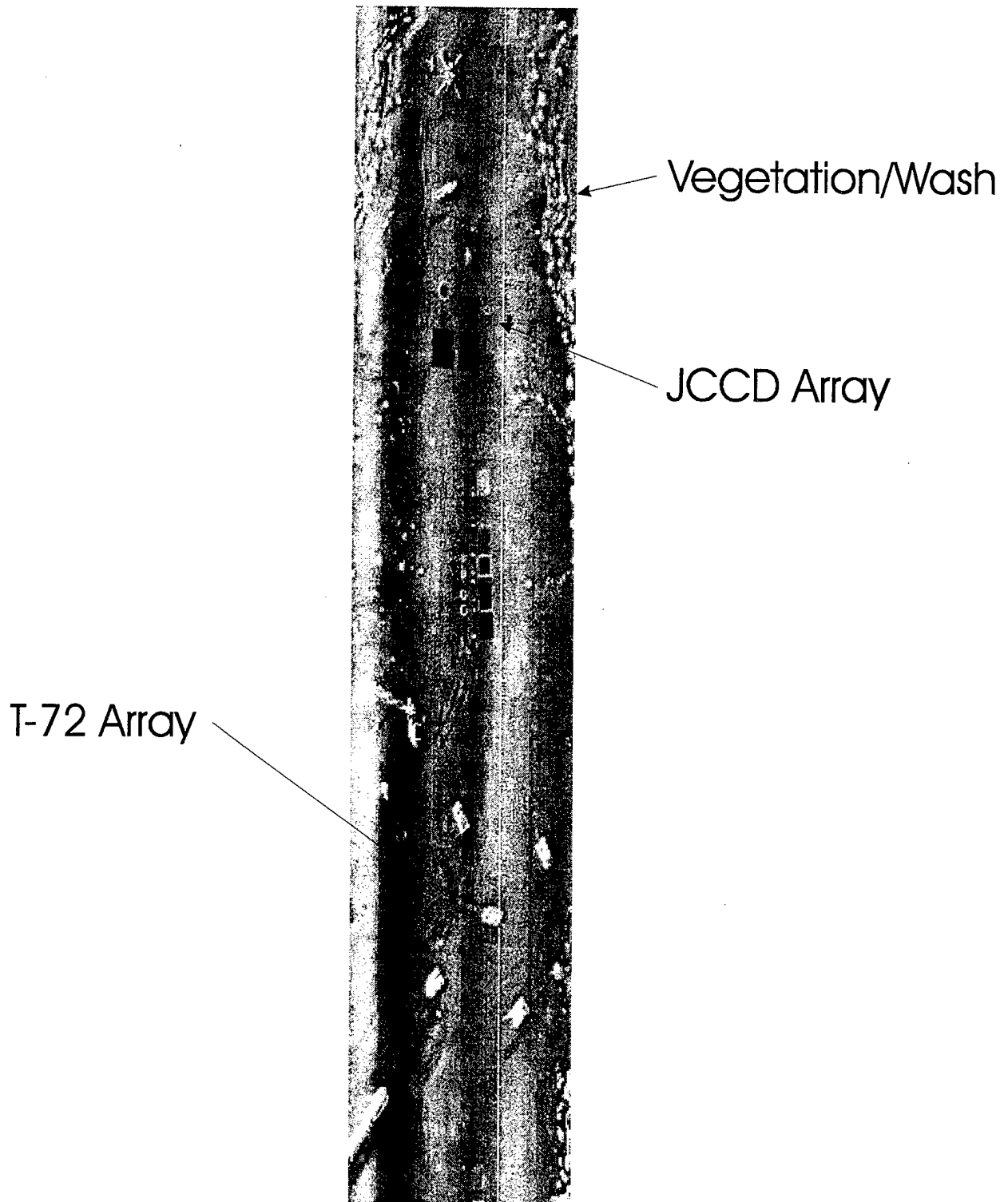


Figure 6.15. Fifth Principal Component Image of Emissivity Data from Malpai Collection Site, 1000 Local Time, 20 October 1995.

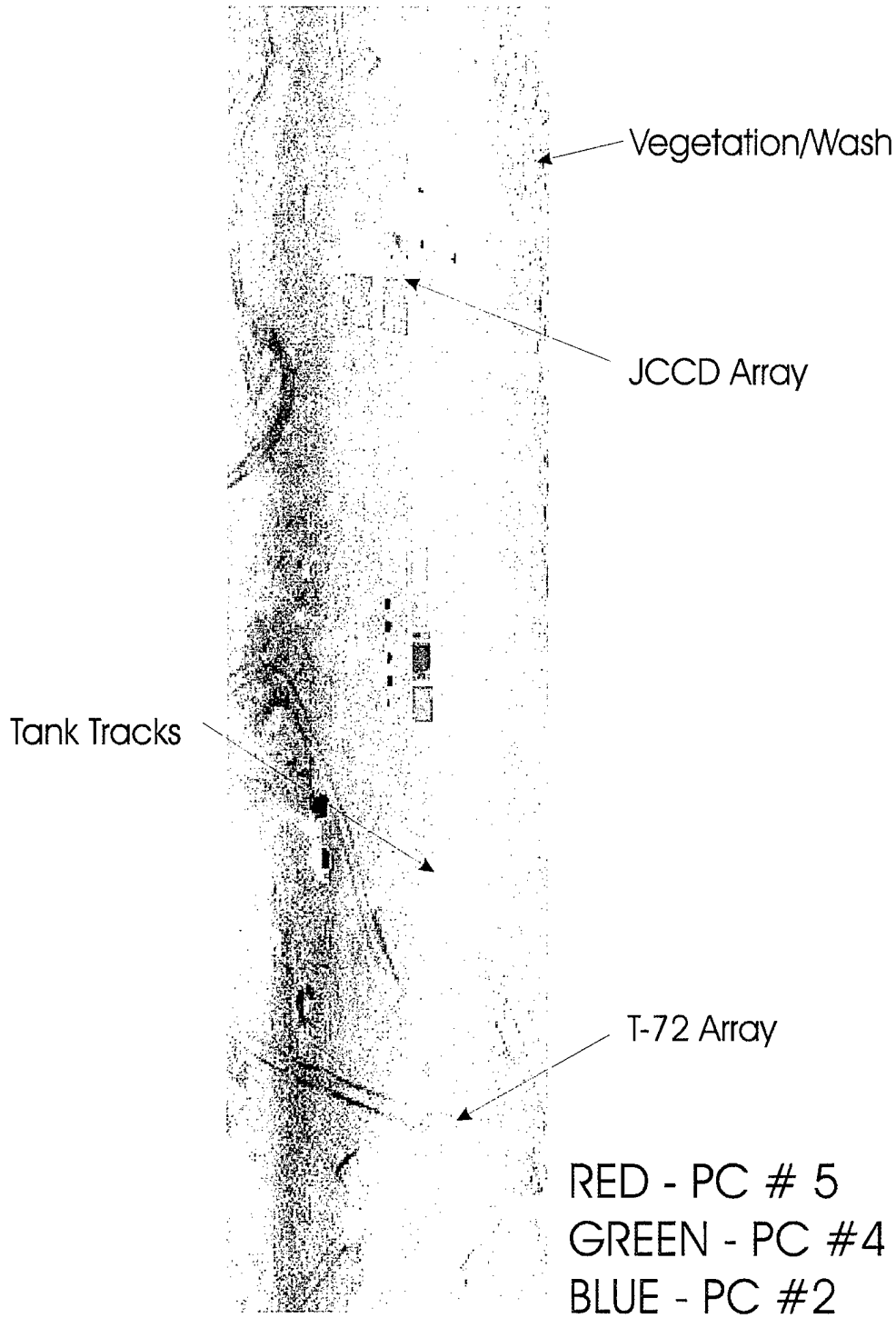


Figure 6.16. Red-Green-Blue Principal Component Image of Emissivity Data from Malpai Collection Site, 1000 Local Time, 20 October 1995.

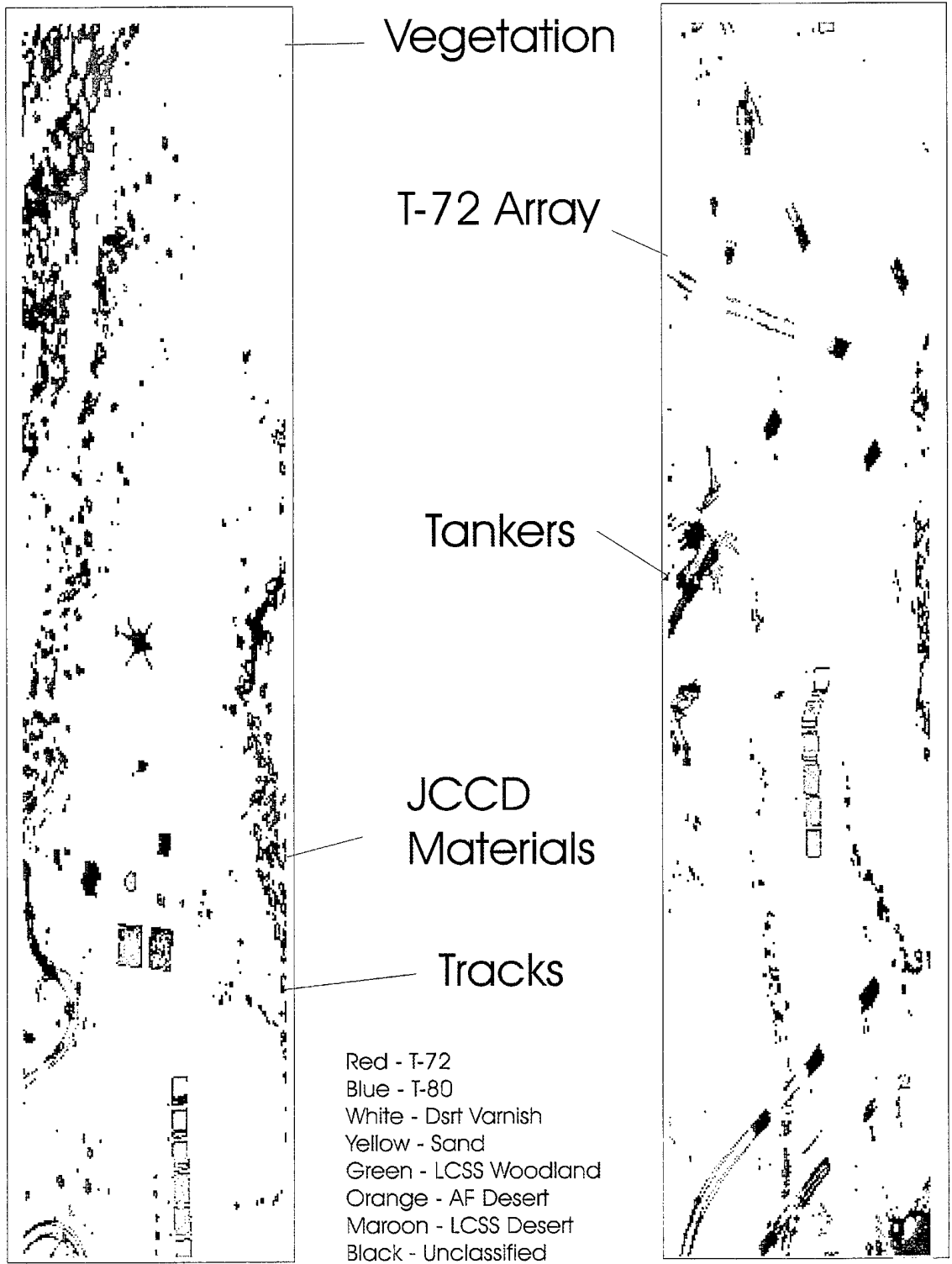


Figure 6.17. Results of SAM Classification of Malpai Collection Site, 1000 Local Time, 20 October 1995 Using Ground Truth Spectra.

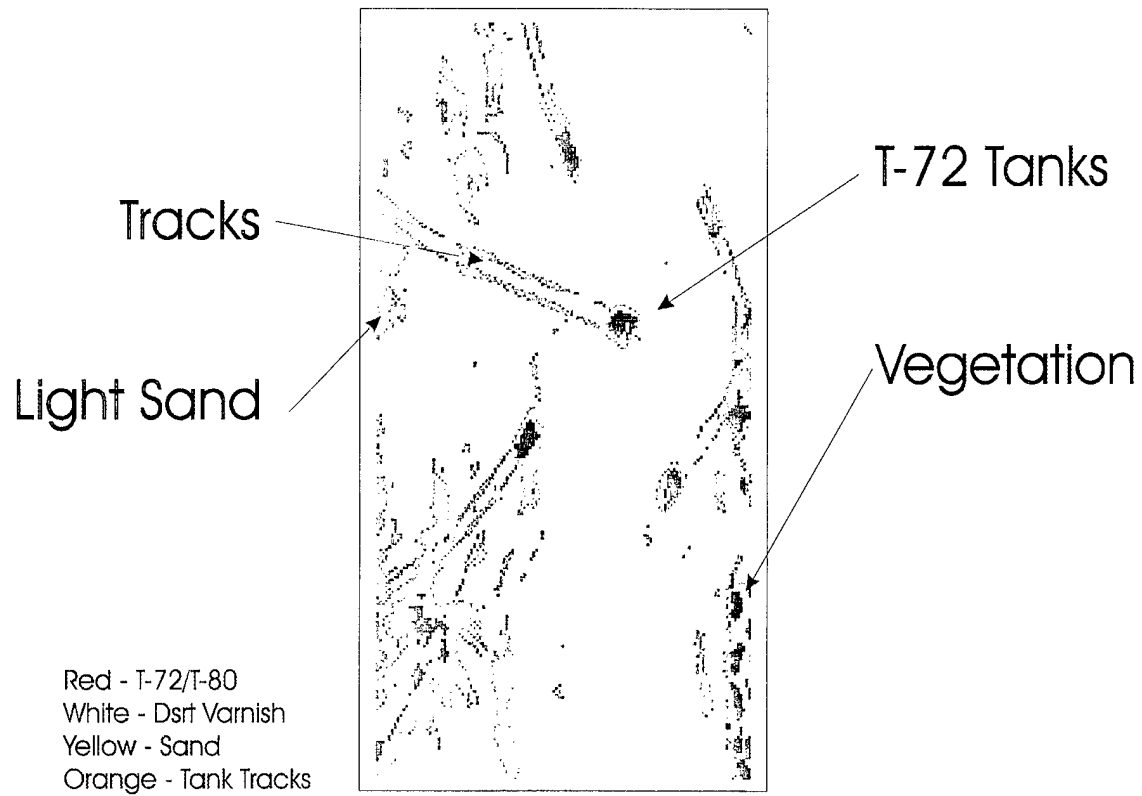


Figure 6.18. Results of SAM Classification of Malpai Collection Site, 1000 Local Time, 20 October 1995 Using Ground Truth and Extracted Spectra.

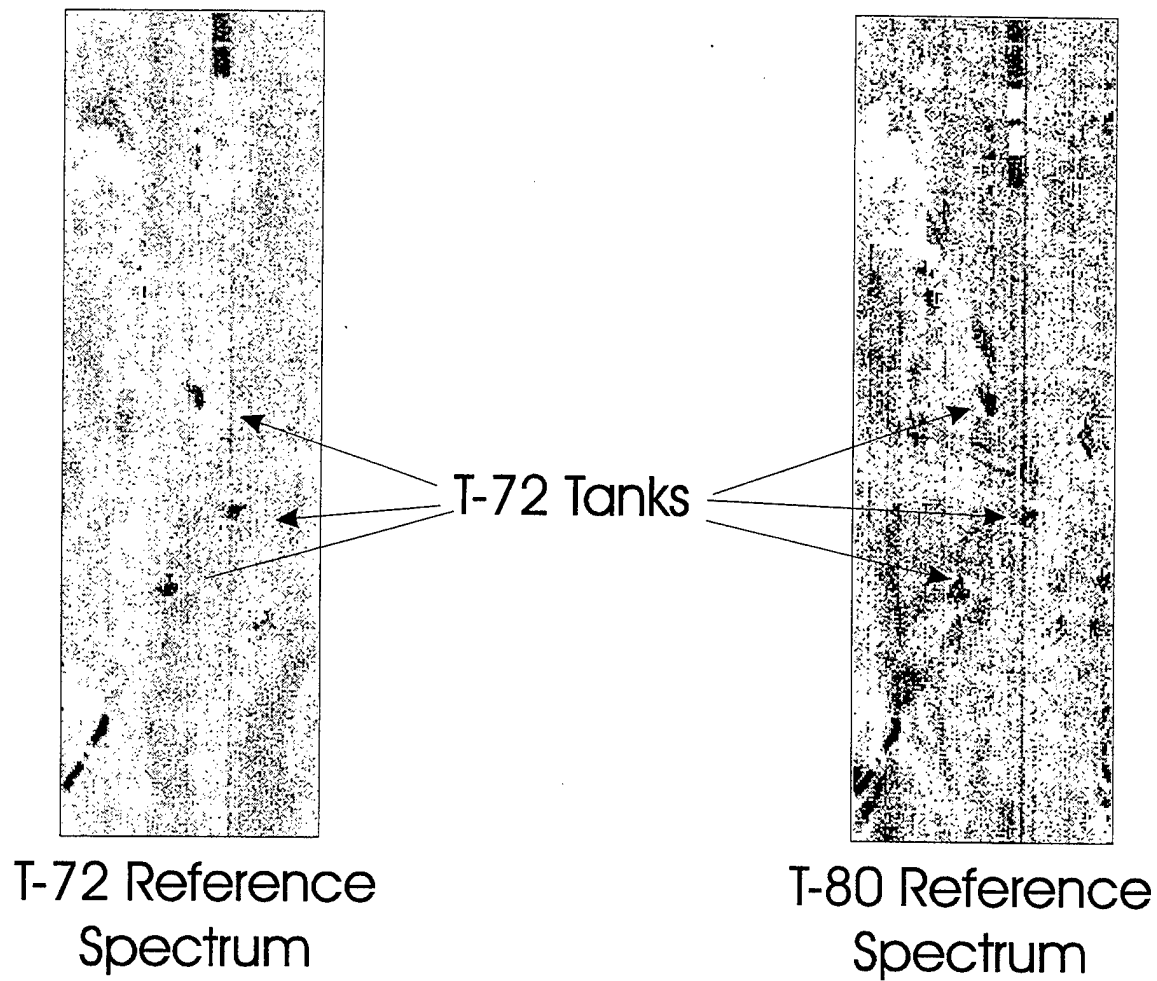


Figure 6.19. Results of SMF on Malpai Data, 1000 Local Time, 20 October 1995 Using T-72 and T-80 Spectra. Dark Areas Represent Matches to Reference Spectrum.

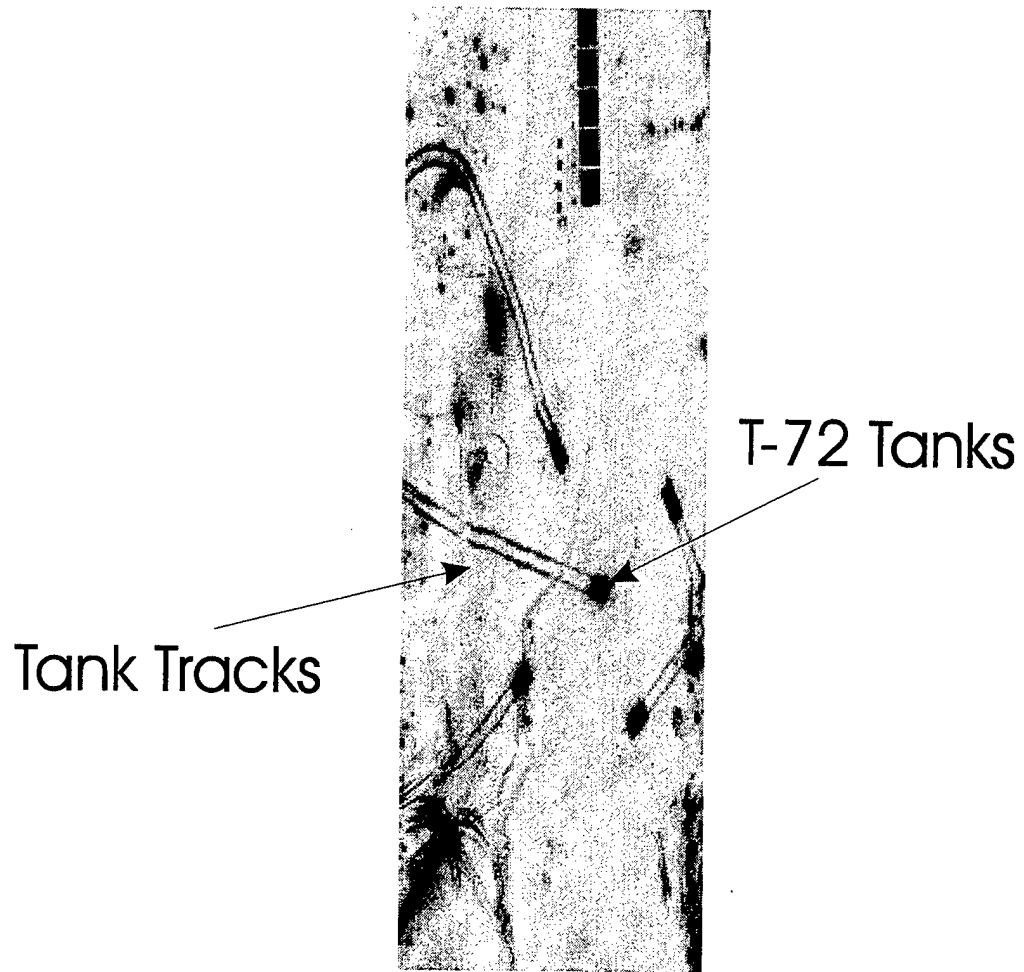


Figure 6.20. Results of SMF on Malpai Data, 1000 Local Time, 20 October 1995 Using Desert Varnish Spectrum. Bright Areas Represent Matches to Reference Spectrum

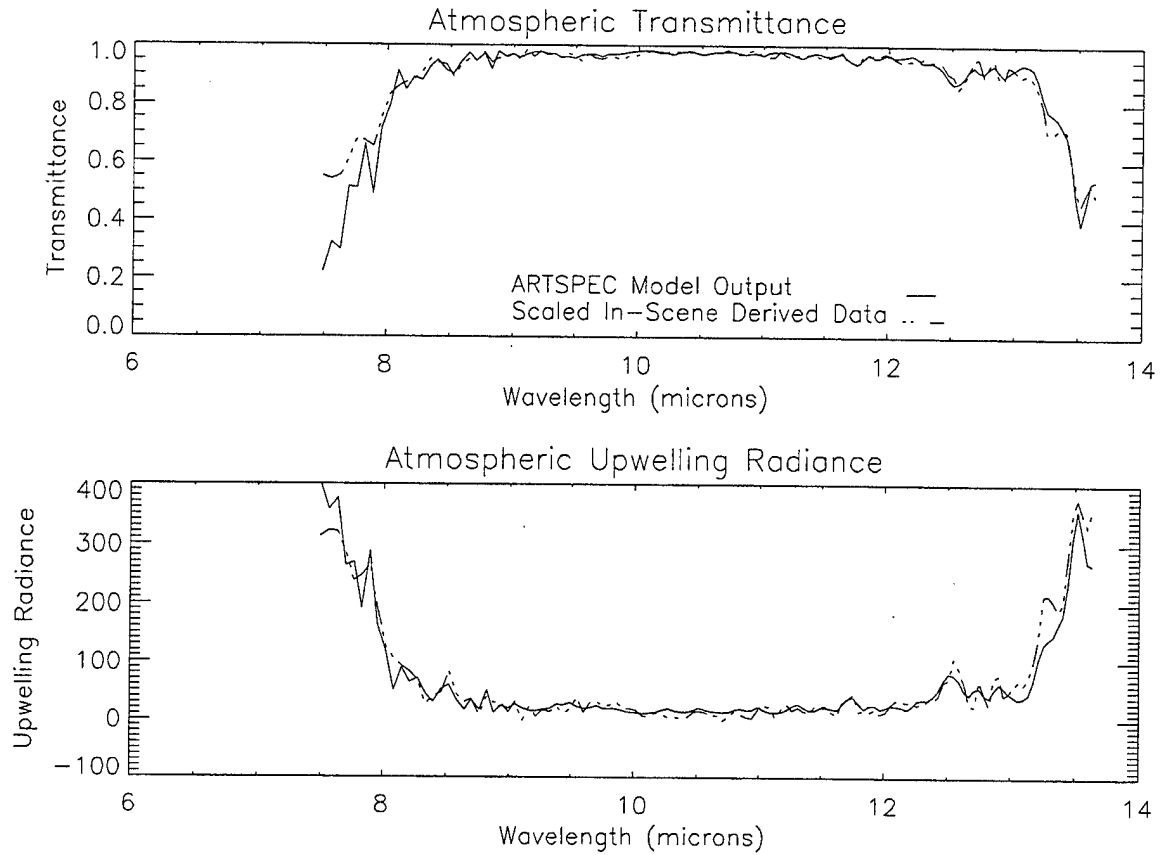


Figure 6.21. Results of ARTSPEC Fitting Routine for SEBASS Data Collected Over JCCD Collection Site, 1000 Local Time, 23 October 1995.

Top of  
Decoy  
Line 1

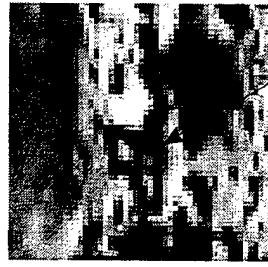
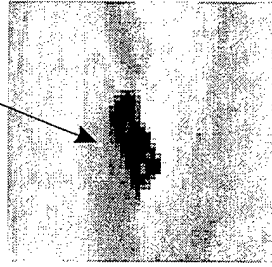
Decoy 1



Bottom of  
Decoy  
Line 1

Figure 6.22. Simulated FLIR image of Decoy Line One of JCCD Collection Site, 1000 Local Time, 23 October 1995.

T-72



Decoy 1

Figure 6.23. Comparison of FLIR Image of Decoy One with FLIR image of T-72 from the Malpai Data.

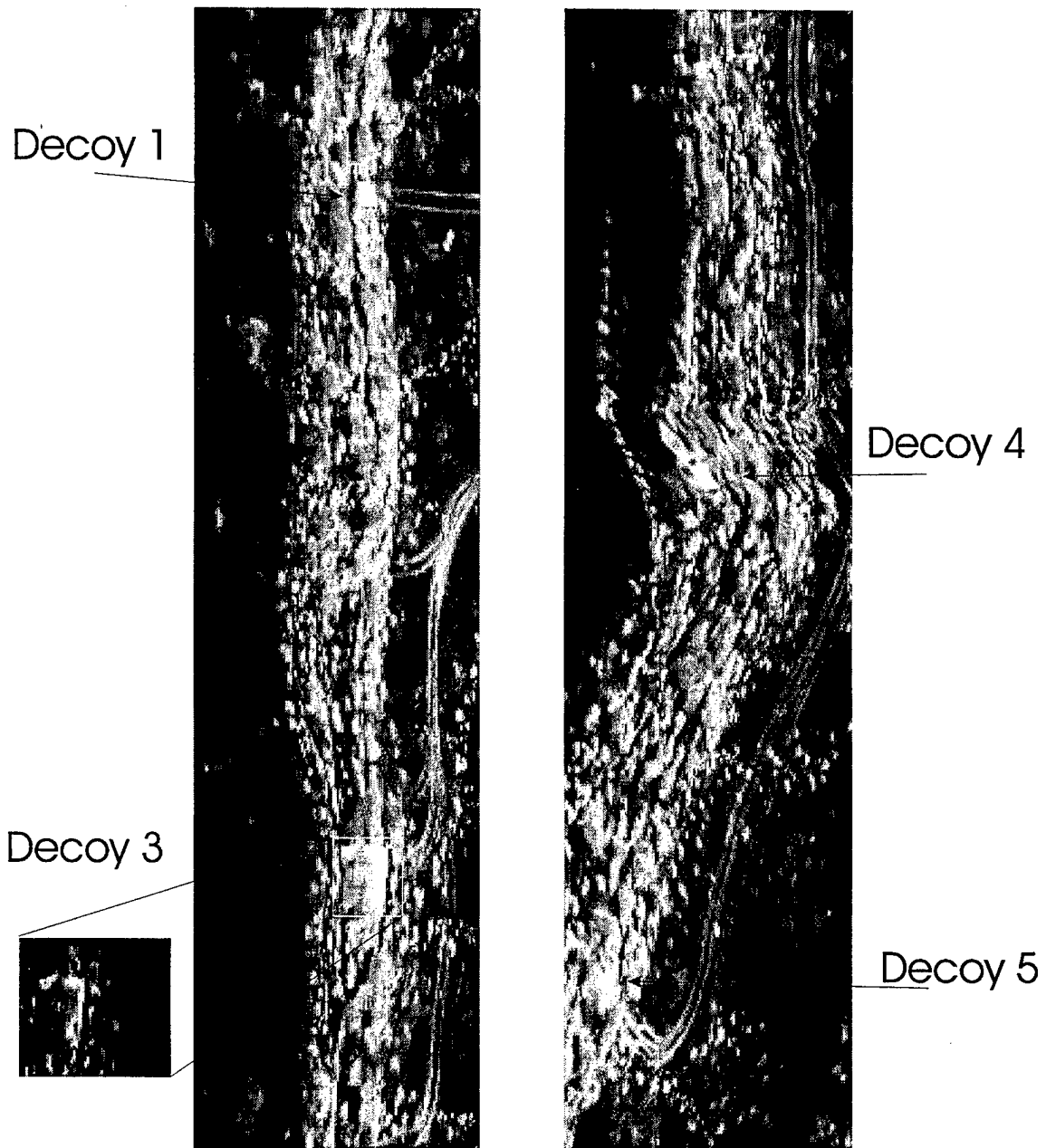


Figure 6.24. Second Principal Component of Radiometrically Calibrated Data from JCCD Decoy Line One, 1000 Local Time, 23 October 1995.

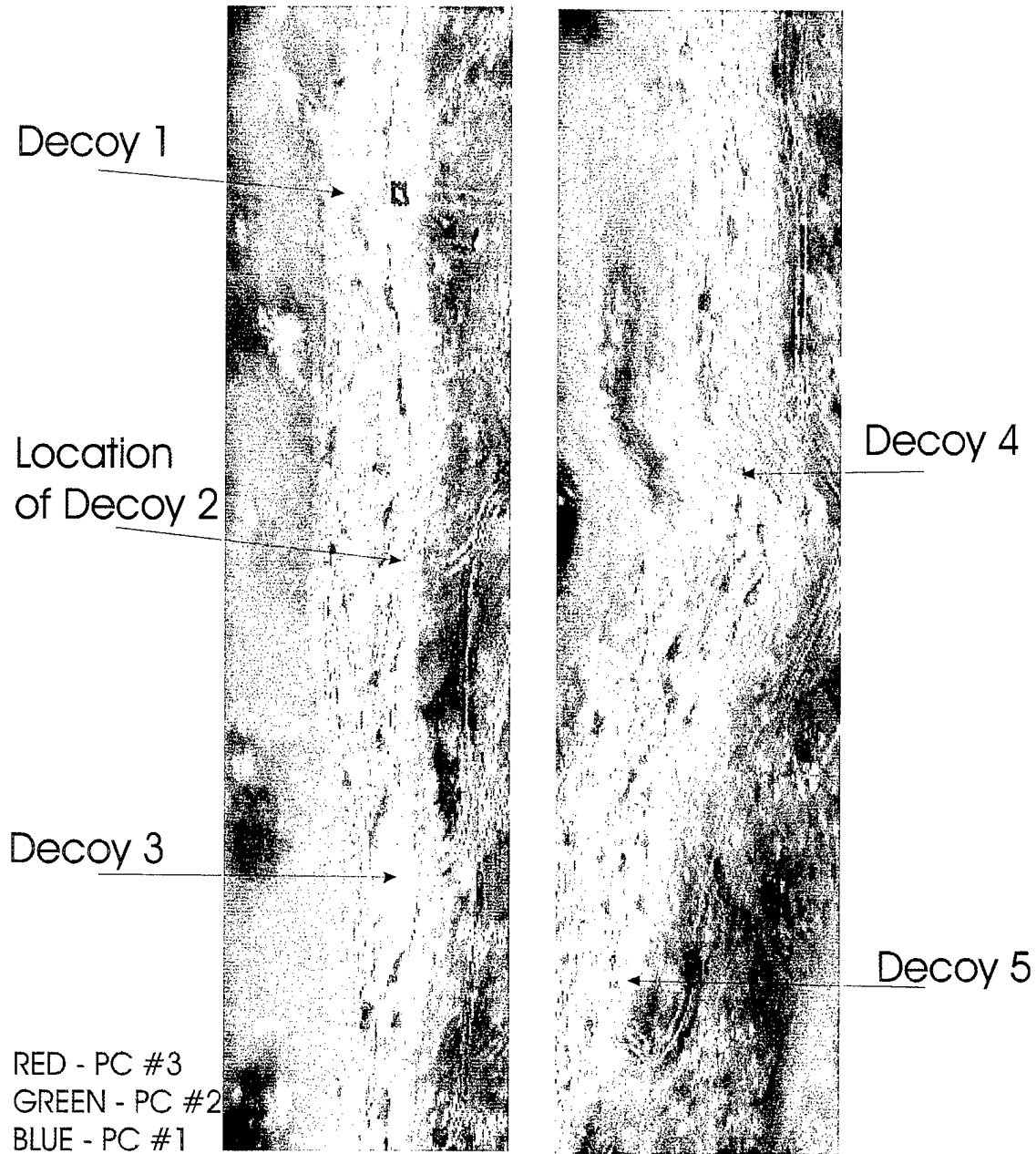


Figure 6.25. Red-Green-Blue Principal Component Image of Radiometrically Calibrated Data from JCCD Decoy Line One, 1000 Local Time, 23 October 1995.

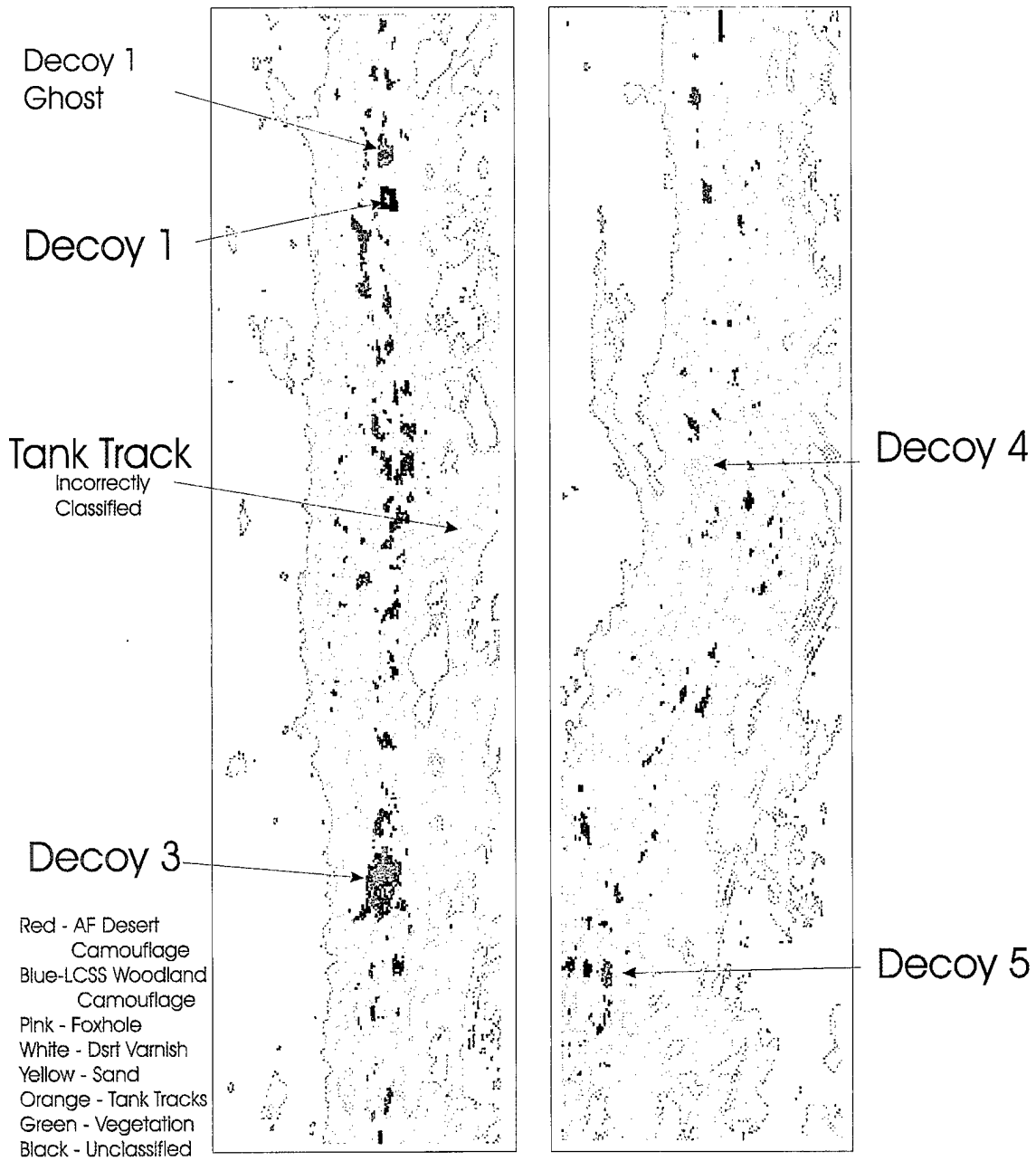


Figure 6.26. Results of SAM Classification of JCCD Decoy Line One, 1000 Local Time, 20 October 1995 Using Ground Truth and Extracted Spectra.

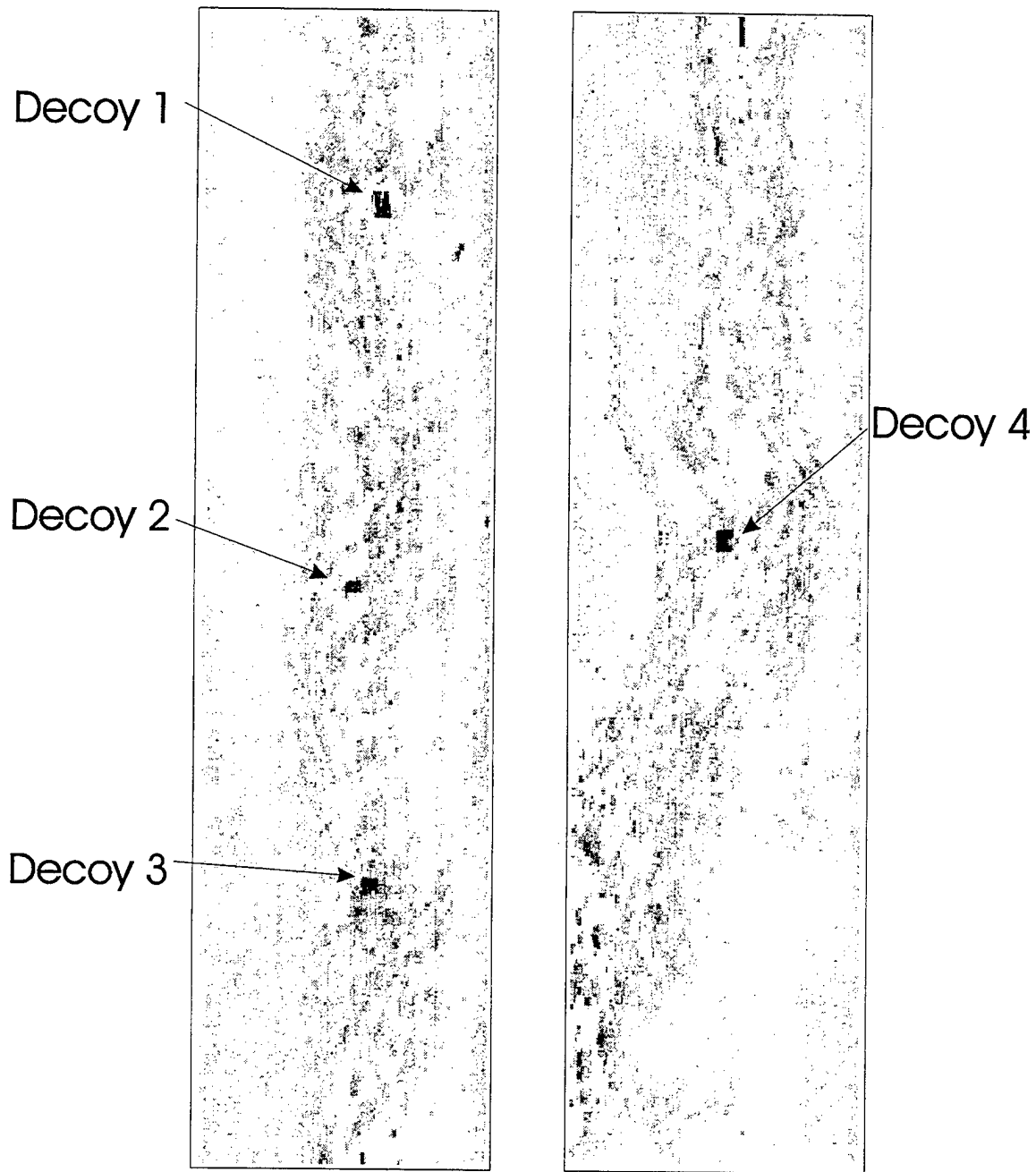


Figure 6.27. Results of SMF on JCCD Decoy Line One, 1000 Local Time, 20 October 1995 Using LCSS Woodland Camouflage. Dark Areas Represent Matches to Reference Spectrum.

Top of  
Decoy  
Line 2

Decoy 1



Bottom of  
Decoy  
Line 2

Figure 6.28. Simulated FLIR image of Decoy Line Two of JCCD Collection Site, 1000  
Local Time, 23 October 1995.

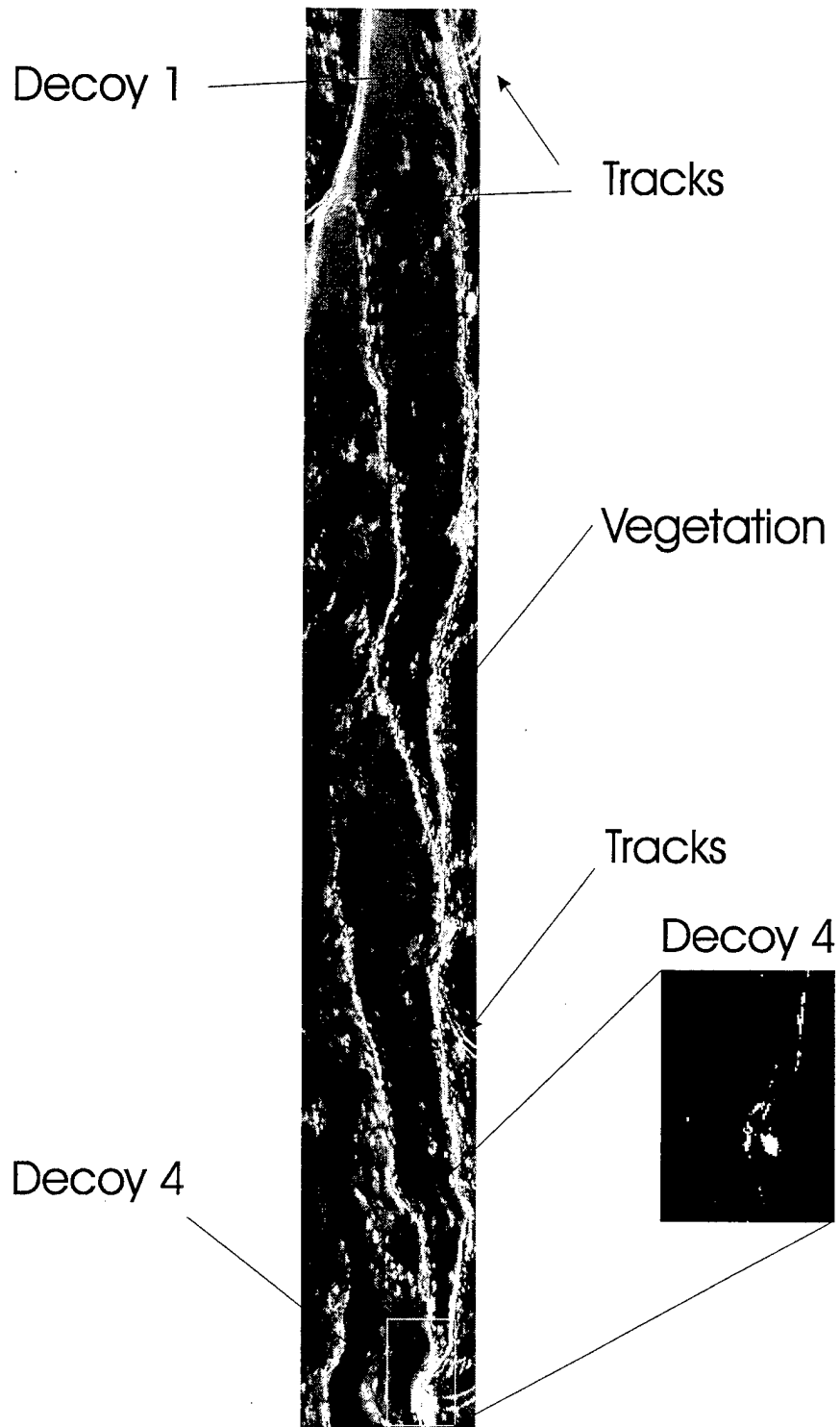


Figure 6.29. Second Principal Component of Radiometrically Calibrated Data from JCCD Decoy Line Two, 1000 Local Time, 23 October 1995.

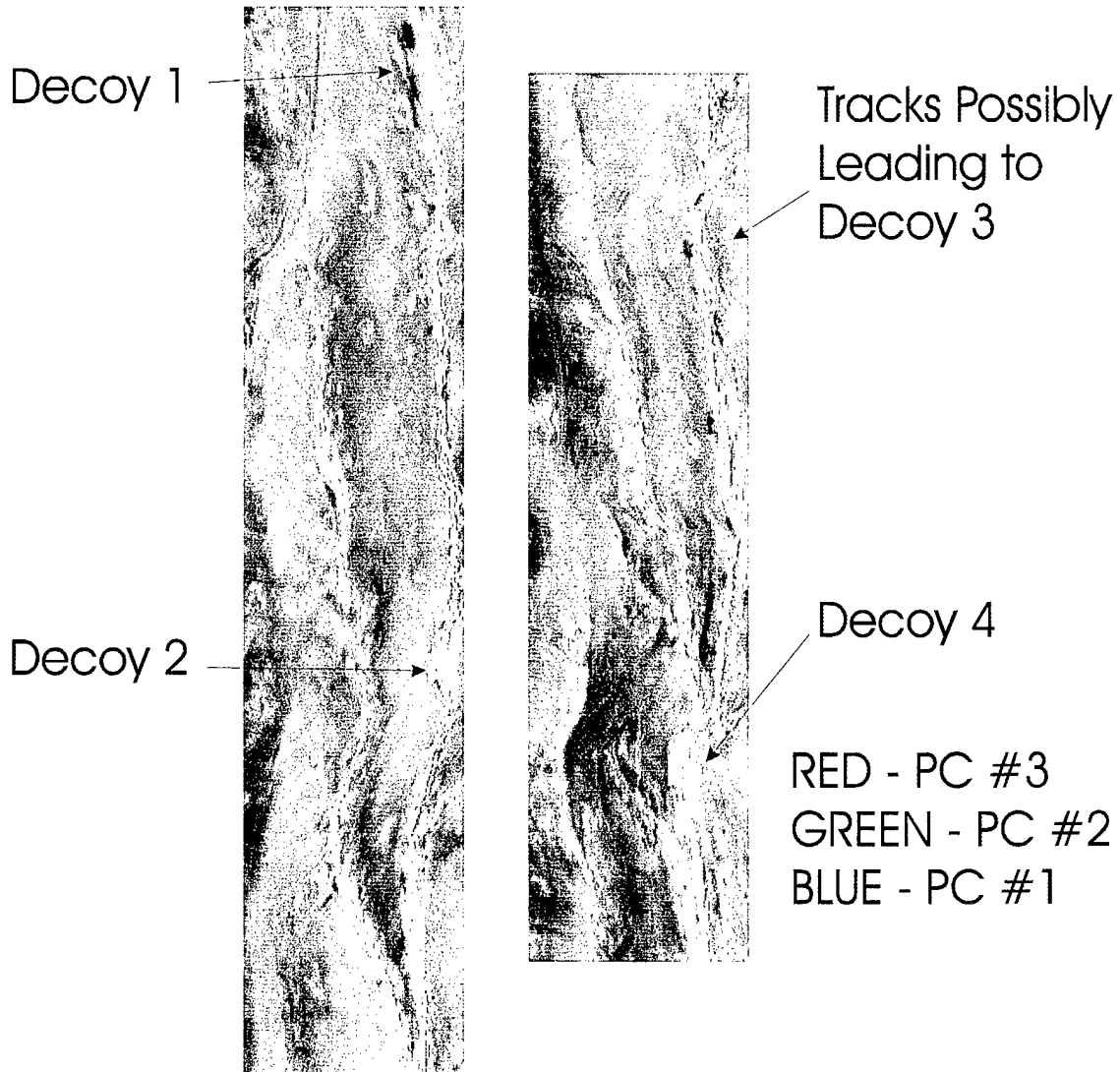


Figure 6.30. Red-Green-Blue Principal Component Image of Radiometrically Calibrated Data from JCCD Decoy Line Two, 1000 Local Time, 23 October 1995.

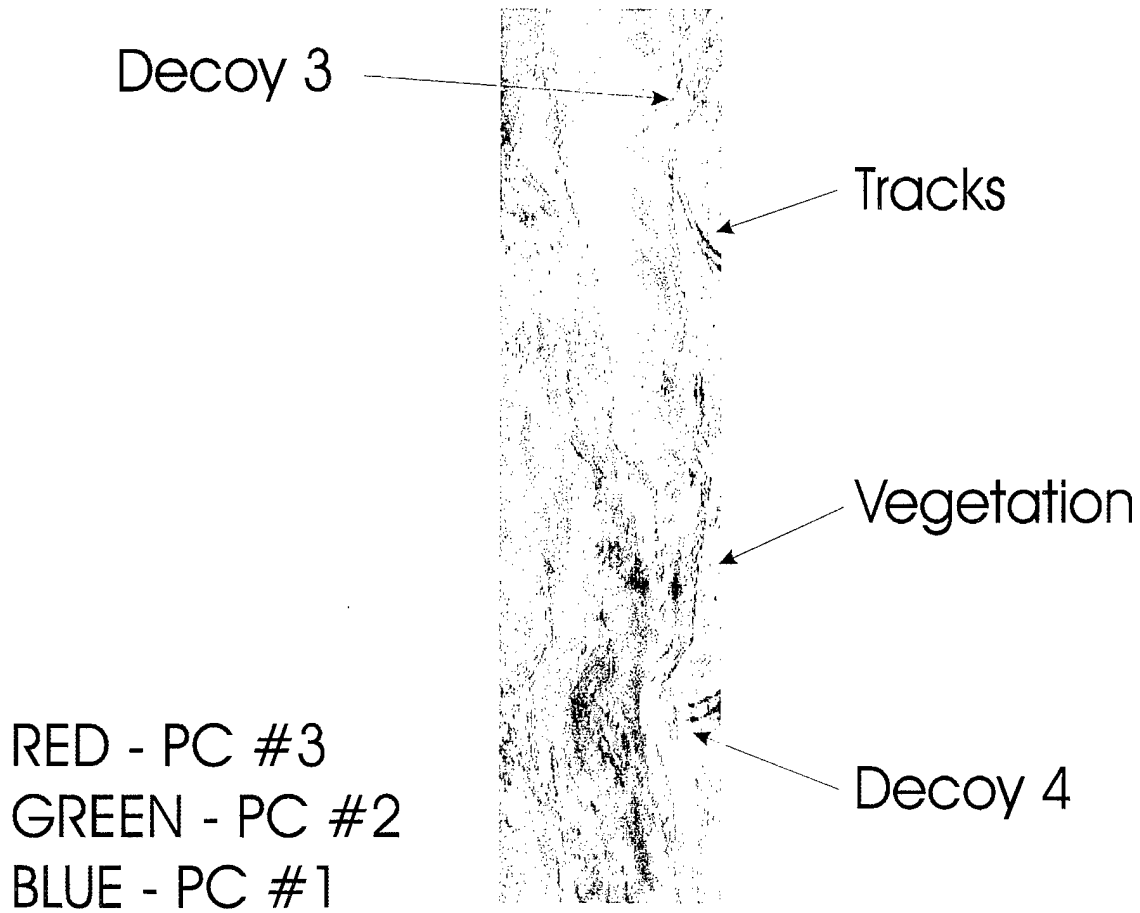


Figure 6.31. Red-Green-Blue Principal Component Image of Emissivity Data from JCCD  
Decoy Line Two, 1000 Local Time, 23 October 1995.

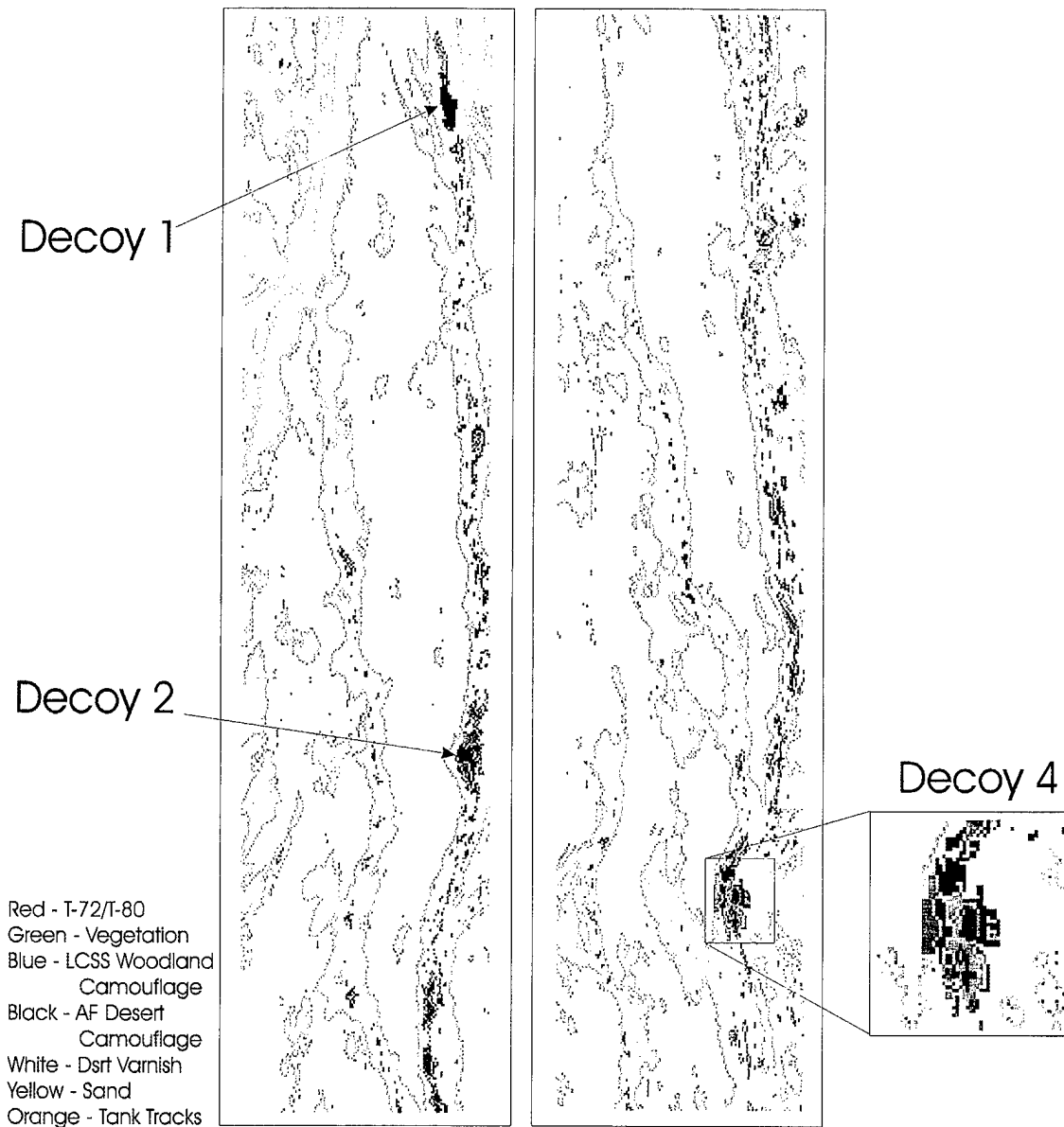


Figure 6.32. Results of SAM Classification of JCCD Decoy Line Two, 1000 Local Time, 23 October 1995 Using Ground Truth and Extracted Spectra.

Decoy 2

Decoy 3

False Alarms

Decoy 4

Red - T-72/T-80  
Green - Vegetation  
Blue - LCSS Woodland  
Camouflage  
Black - AF Desert  
Camouflage  
White - Dsrft Varnish  
Yellow - Sand  
Orange - Tank Tracks

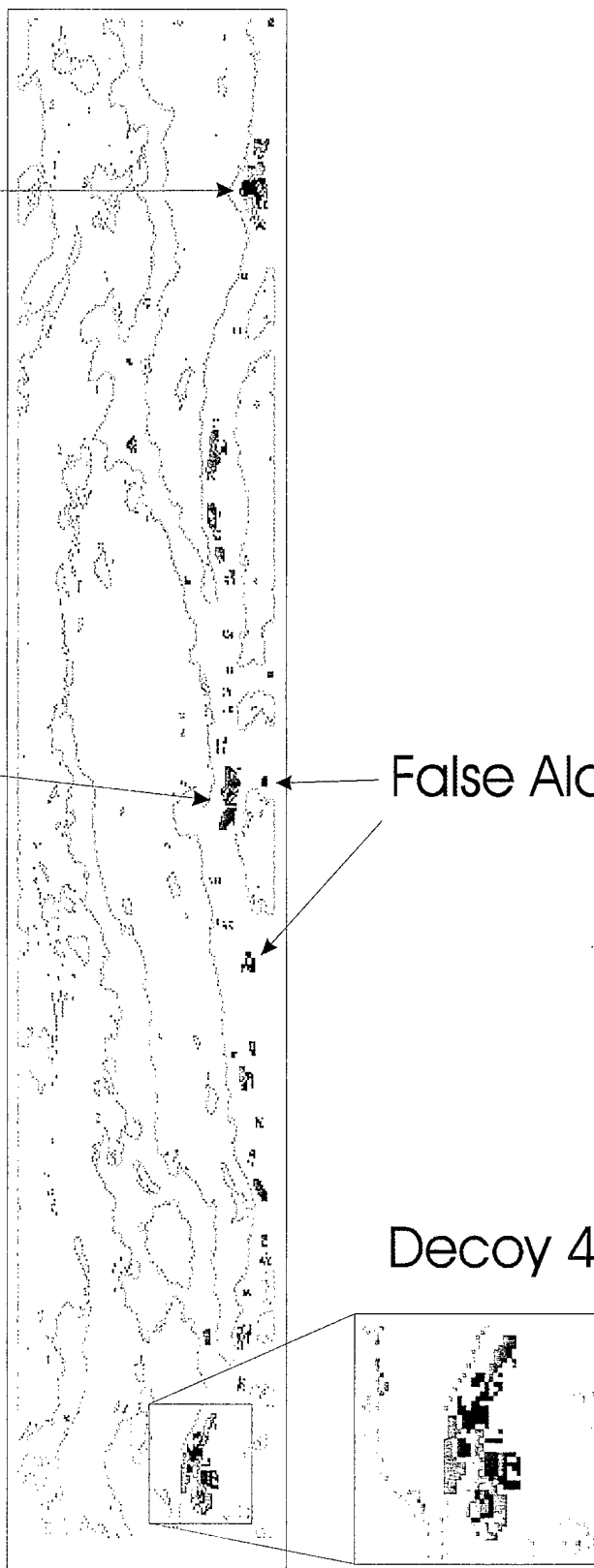


Figure 6.33. Results of SAM Classification of JCCD Decoy Line Two Following Application of Spatial Filtering Using Ground Truth and Extracted Spectra.

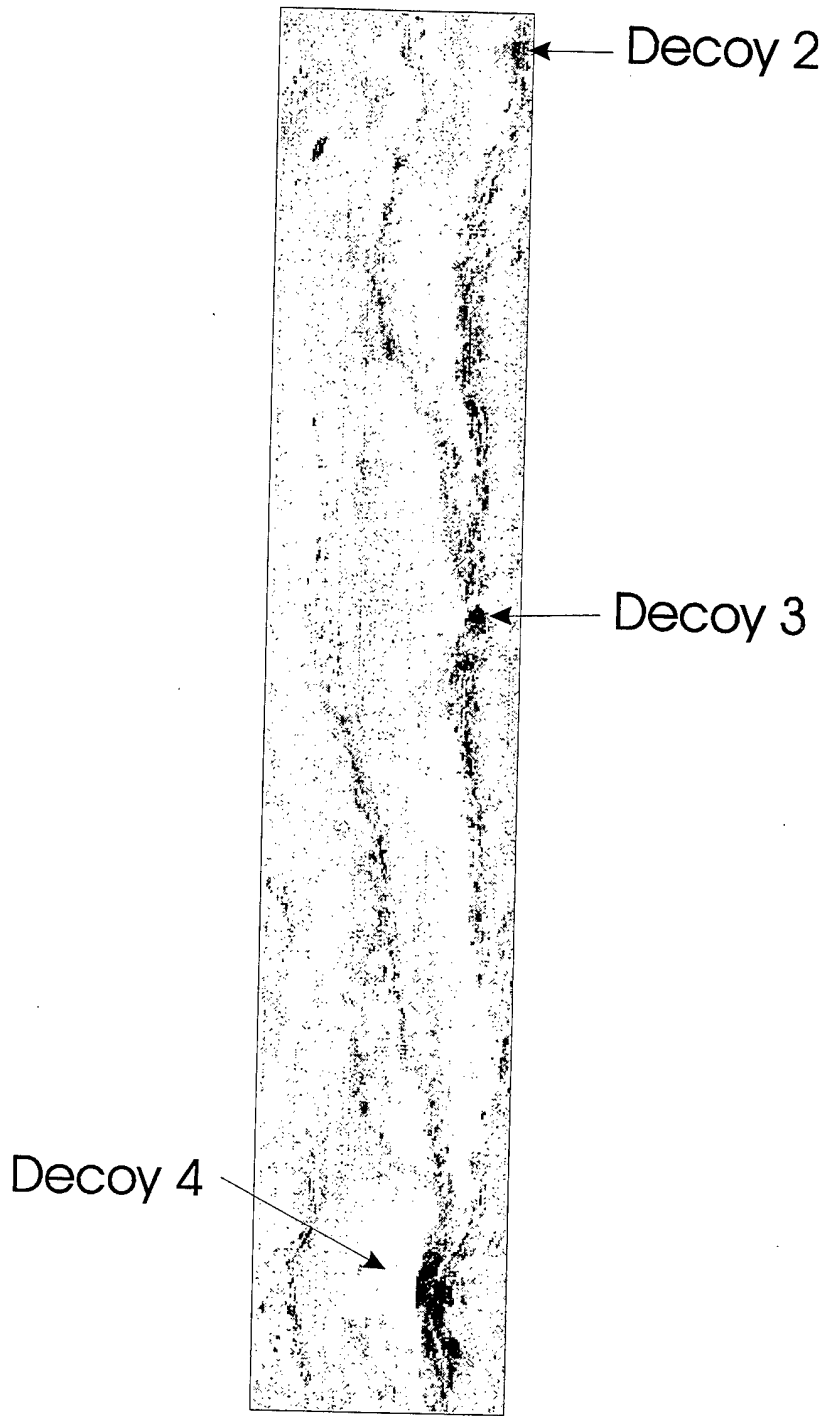
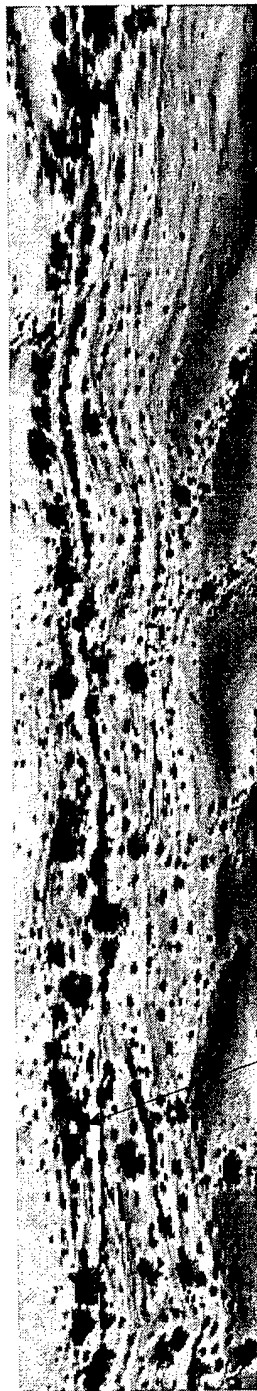


Figure 6.34. Results of SMF on JCCD Decoy Line Two, 1000 Local Time, 20 October 1995 Using LCSS Woodland Camouflage. Dark Areas Represent Matches to Reference Spectrum.

Top of  
Vehicle  
Target  
Line



Tank 4  
(325 K)

Bottom of  
Vehicle  
Target  
Line

Figure 6.35. Simulated FLIR image of Vehicle Target Line of JCCD Collection Site,  
1000 Local Time, 23 October 1995.

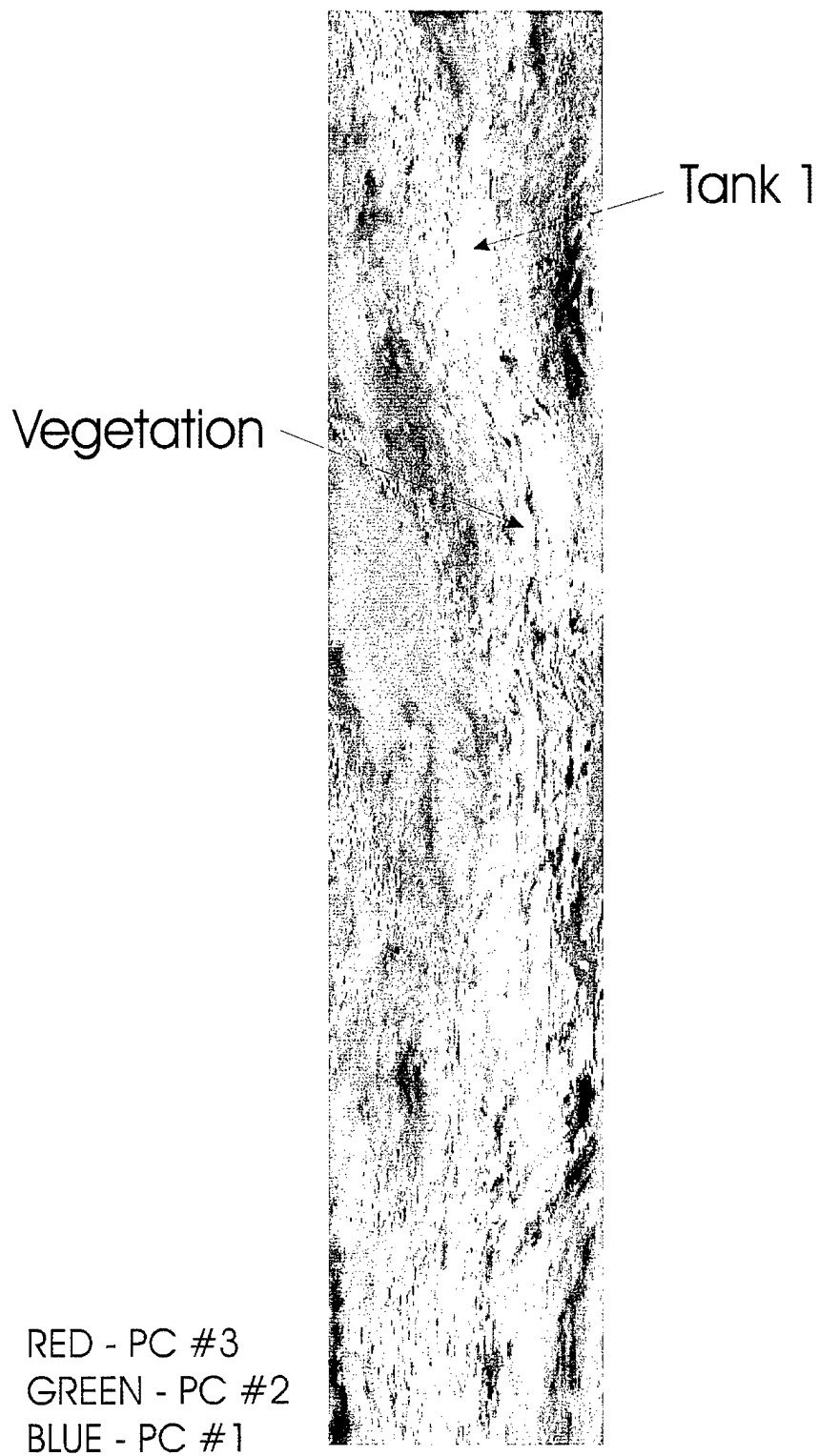


Figure 6.36. Red-Green-Blue Principal Component Image of Radiometrically Calibrated Data from JCCD Vehicle Target Line, 1000 Local Time, 23 October 1995.

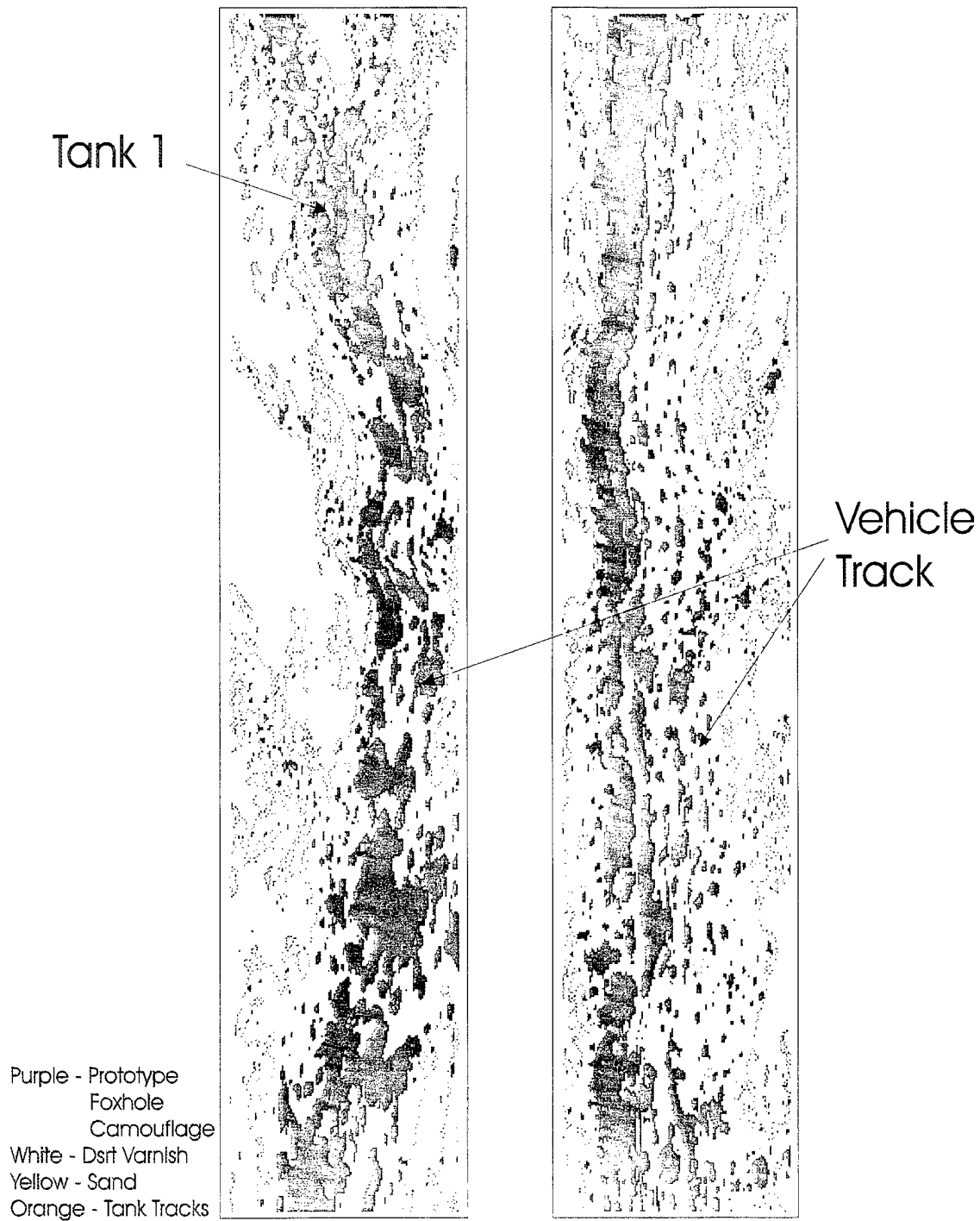


Figure 6.37. Results of SAM Classification of JCCD Vehicle Target Line, 1000 Local Time, 23 October 1995 Using Ground Truth and Extracted Spectra.

Tank 1

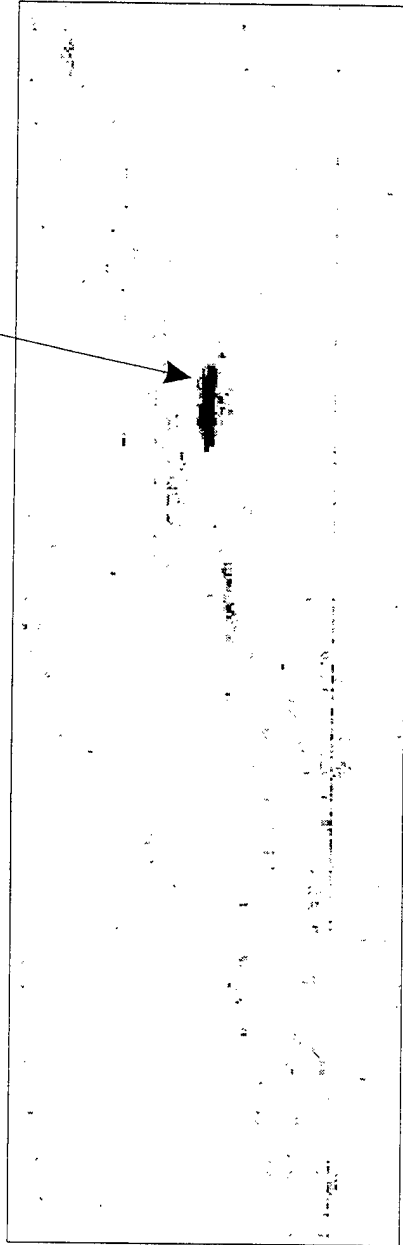


Figure 6.38. Results of SMF on JCCD Vehicle Target Line, 1000 Local Time, 20 October 1995 Using Air Force Desert Camouflage. Dark Areas Represent Matches to Reference Spectrum.

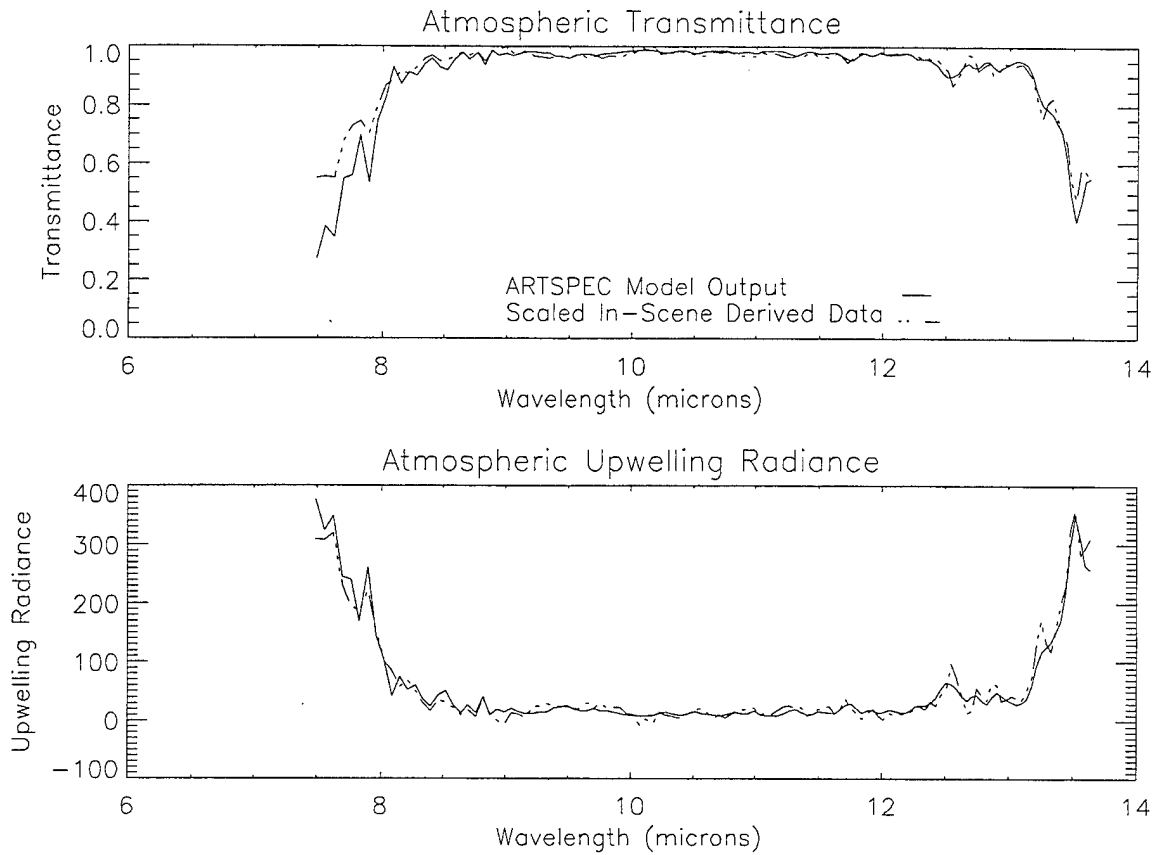


Figure 6.39. Results of ARTSPEC Fitting Routine for SEBASS Data Collected Over Arroyo Collection Site, 1000 Local Time, 23 October 1995.

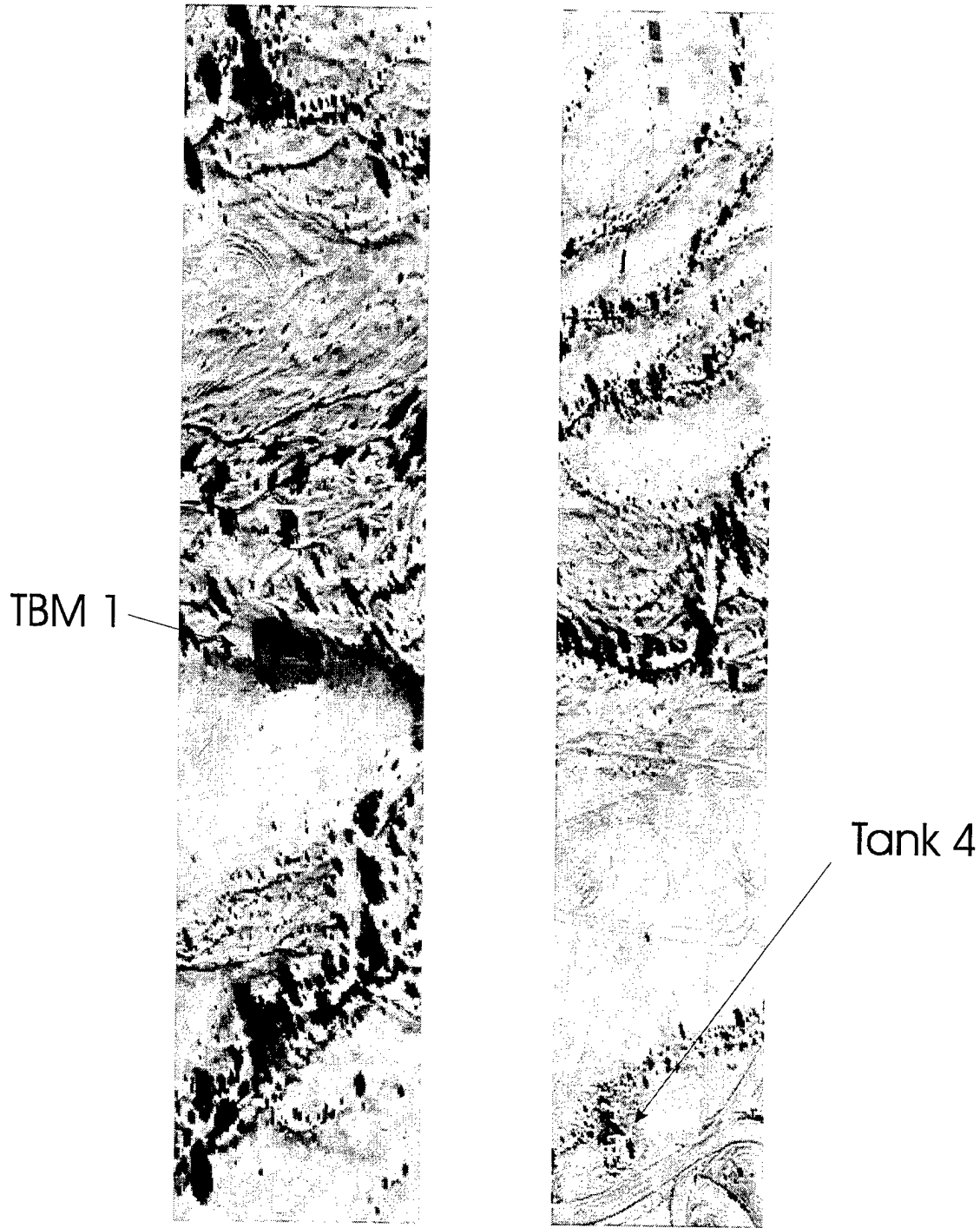


Figure 6.40. Simulated FLIR image of Arroyo Collection Site, 1000 Local Time, 23 October 1995.

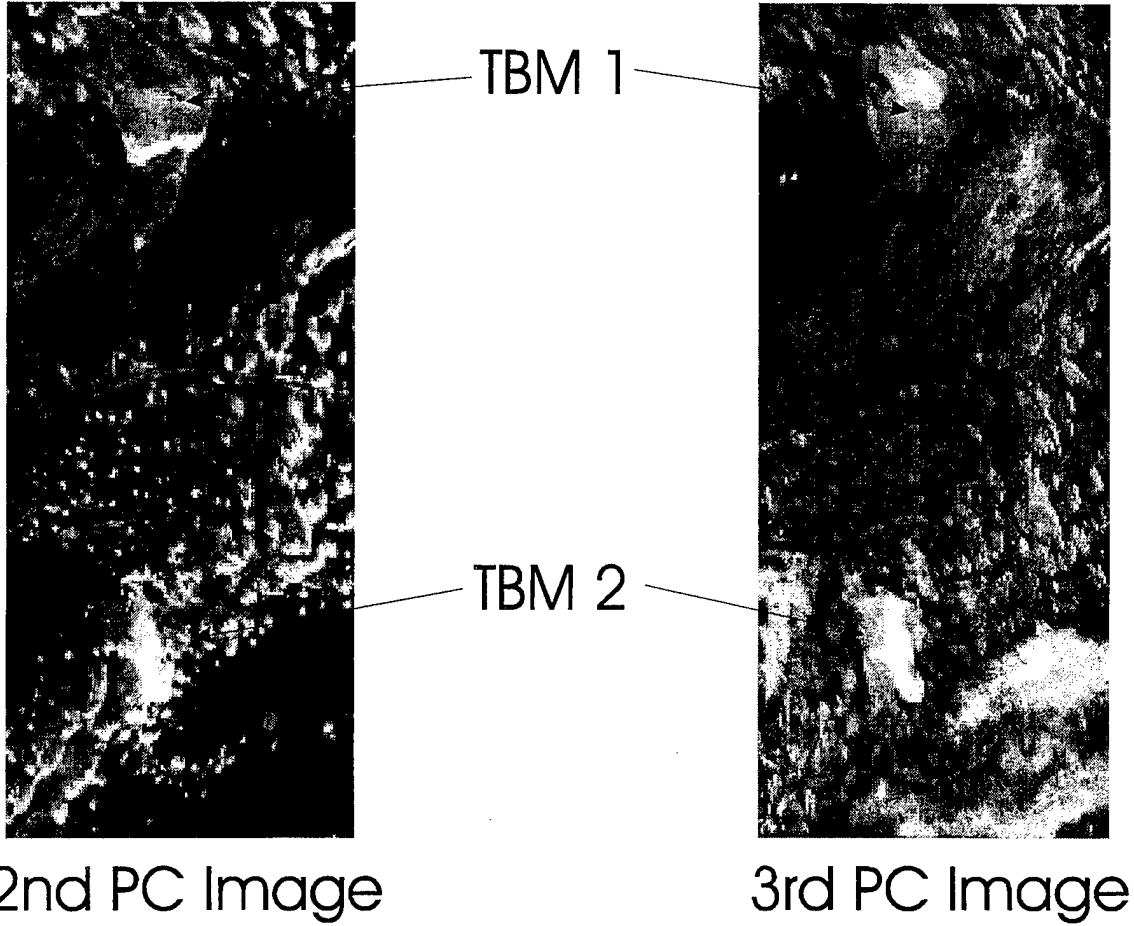


Figure 6.41. Second and Third Principal Components of Radiometrically Calibrated Data from Arroyo Collection Site, 1000 Local Time, 23 October 1995.

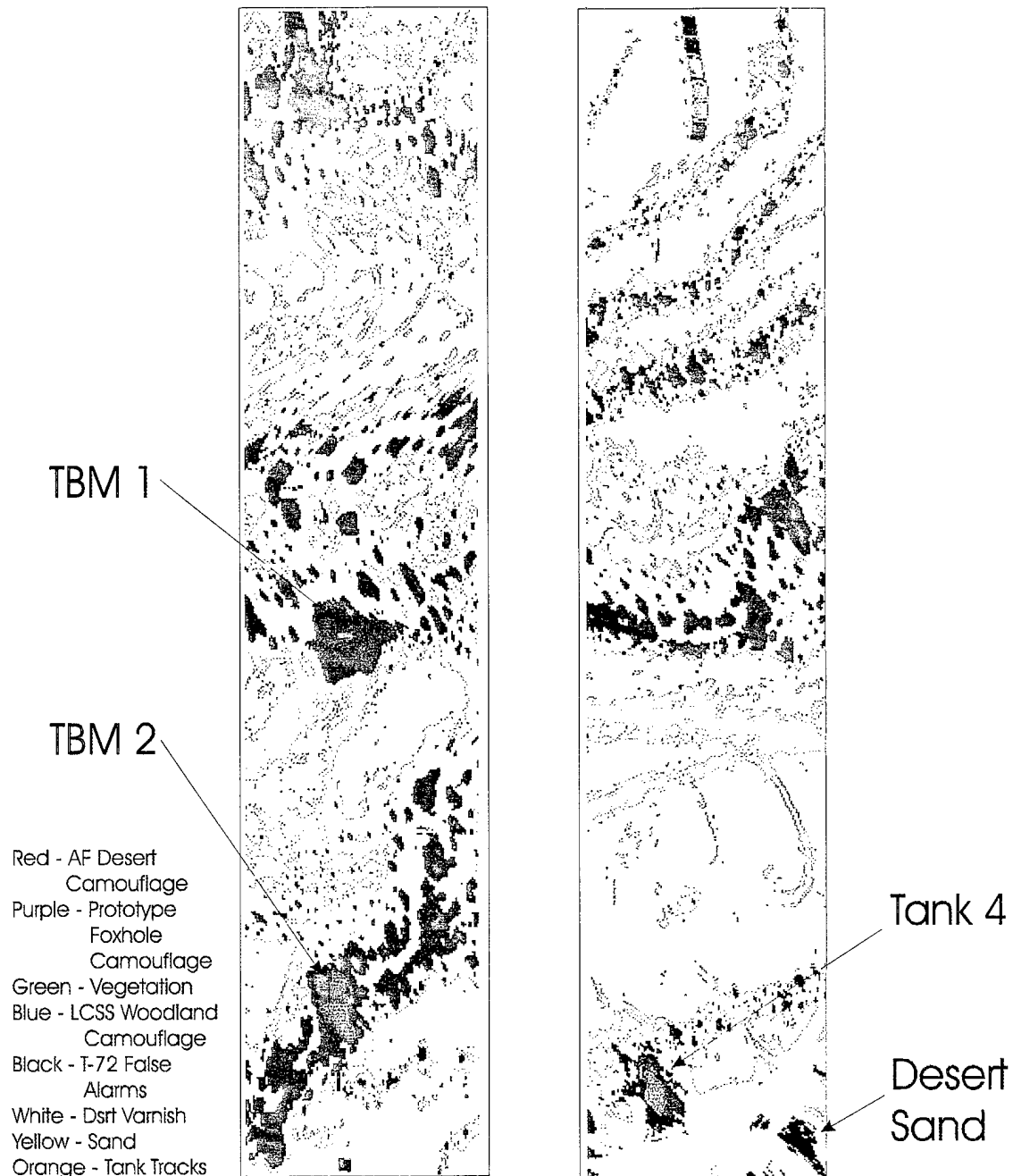


Figure 6.42. Results of SAM Classification of Arroyo Collection Site, 1000 Local Time, 23 October 1995 Using Ground Truth and Extracted Spectra.

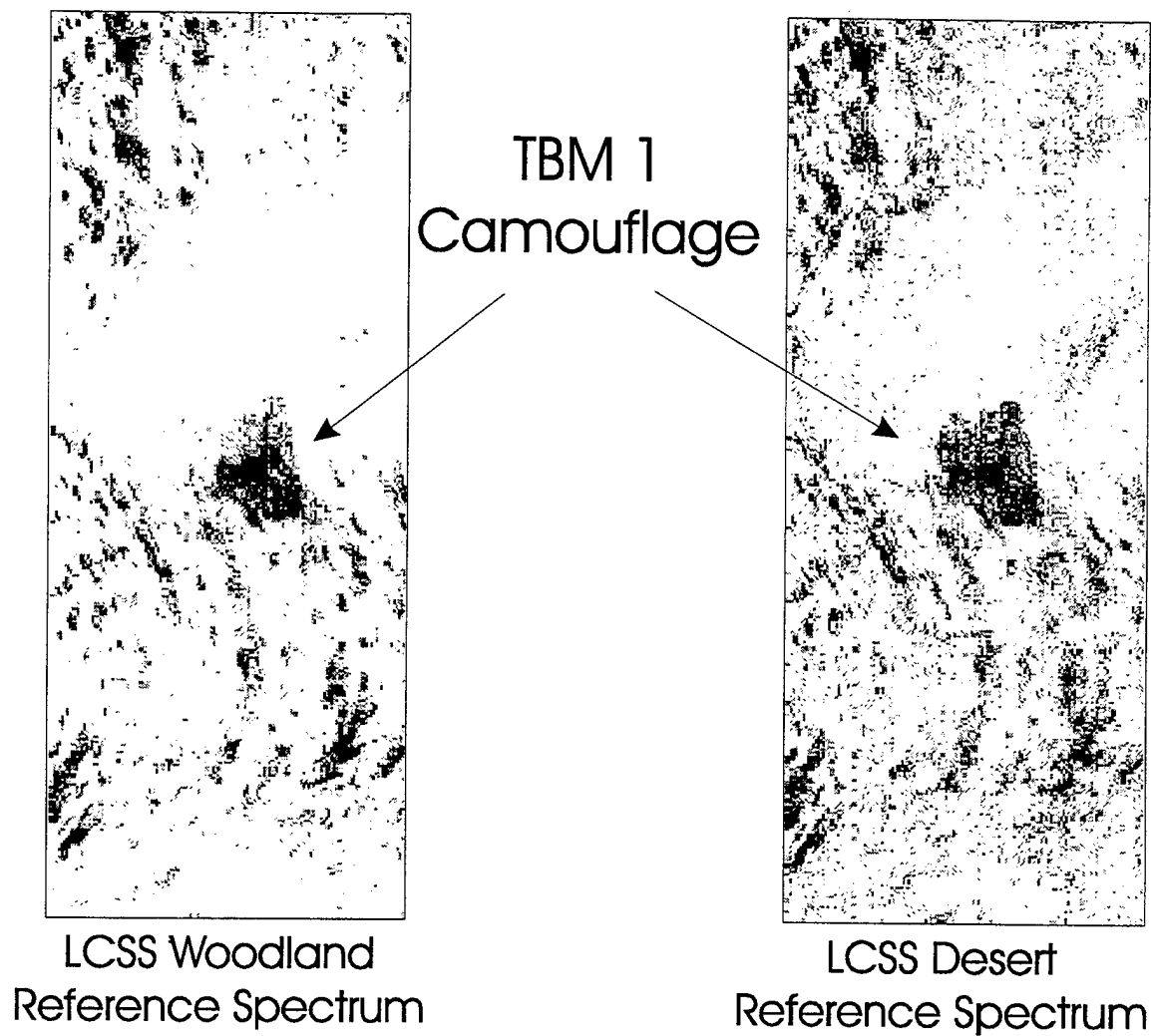


Figure 6.43. Results of SMF on Arroyo Collection Site, 1000 Local Time, 20 October 1995 Using LCSS Woodland Camouflage and LCSS Desert Camouflage. Dark Areas Represent Matches to Reference Spectrum.

## APPENDIX B. ATMOSPHERIC COMPENSATION ALGORITHM

```
; PROGRAM: plastic_ruler.pro
;     Revision: 21 May 96

;     PERFORMS PLASTIC RULER ATMOSPHERIC COMPENSATION
;     Performs basic plastic ruler routine then repeats using
;     lambda at maximum of transmittance for reference wavelength.
;     Based on IDL program written by Bongiovi, Hackwell, and Hayhurst
;     Modified on 21 May to skip reference calculation.

;     FUNCTIONS CALLED:
;     wave.pro     FUNCTION TO CALCULATE WAVELENGTH FOR EACH PIXEL
;                 SEBASS ARRAY (from Aerospace Corporation)
;     blackbody.pro FUNCTION TO CALCULATE BLACKBODY RADIANCE FOR
;                 EACH PIXEL IN ARRAY
;     brightness.pro FUNCTION TO GENERATE BRIGHTNESS TEMP FOR
;                 RADIANCE(uw/sr um cm^2)
;     noise_estimate.pro ;     FUNCTION TO PERFORM NOISE ESTIMATION
;                 REQUIRED FOR PLASTIC RULER
;                 ATMOSPHERIC COMPENSATION
;     screen.pro   FUNCTION TO SCREEN DATA FOR SPECIFIC THRESHOLD
;                 OF BRIGHTNESS VALUES
;     do_plot.pro  PROCEDURE TO PLOT STRIPS OF ATMOSPHERIC WINDOW
;     ks_line.pro  PROCEDURE WRITTEN BY JOHN HACKWELL TO PERFORM
;                 LINE FIT FOR CLUSTER OF POINTS

;     INPUT:
;     #####_cal.dat FLTARR(128,128,2000) Calibrated data file
;     cal#####.cal.bip FLTARR(128,128,256) Calibrated calibration file

;     OUTPUT:
;     atmosphere.dat [transmittance(128),upwelling(128)] FLOAT
;     results of basic Hackwell

; DEFINE WINDOW AND SET-UP FILES

calfile='/rs1_02/collins/b_tmp/23oct95_1000/cal2_15.75.cal'
infile='/rs1_02/collins/b_tmp/23oct95_1000/jccd4/jccd4.cal'
outfile='/tmp/jccd4_atmosphere.dat'

sand_threshold=.3
vegetation_threshold=.5

print,'Running Plastic Ruler with:
print,' sand_threshold= ',sand_threshold
print,' vegetation_threshold= ',vegetation_threshold

spatial=[0,127]
frame=[200,1200]
```

```

spawin=indgen(spatial(1)-spatial(0)+1)+spatial(0)
framewin=indgen(frame(1)-frame(0)+1)+frame(0)
print, 'Window Contains ', n_elements(spawin)*n_elements(framewin), ' pixels'

```

```

; SETUP WAVELENGTH ARRAY

```

```

wv=wave()
lambda=fltarr(128,n_elements(spawin))
for i=0,n_elements(spawin)-1 do lambda(*,i)=wv(*,63)

```

```

; PERFORM NOISE ESTIMATE

```

```

noise=noise_estimate(calfile,spatial)
;noise2=noise_estimate(calfile2,spatial)
plot,noise
;oplot,noise2,linestyle=2
stop

```

```

; LOAD IN WINDOW OF DATA

```

```

openr, unit, infile,/get_lun

```

```

temp=fltarr(128,128)
for loop=0, frame(0)-1 do begin
    forrd,unit,temp
endfor

```

```

data=fltarr(128,128,n_elements(framewin))

```

```

forrd,unit,data
close, unit
free_lun,unit

```

```

atmdata= data(*,spatial(0):spatial(1),*)
allatmdata=reform(atmdata,128,n_elements(spawin)*$
    n_elements(framewin))

```

```

; SCREEN FOR BLACKBODIES

```

```

print,'screening for blackbodies'

```

```

;     CHECK FOR SAND MIXING (10 to 9.45)
;     average pixels ivo 10 and compare to pixels ivo of 9.45
;     which is in reststrahlen band

```

```

lambdaA=[9.9,10.1]
lambdaB=[9.3,9.6]

```

```

vegetation=screen(allatmdata,lambda,lambdaA,lambdaB,sand_threshold)
vegetationcount=n_elements(vegetation)
print, ' Selected ',vegetationcount,' vegetation pixels'

```

```

;     CHECK FOR SENESCENT GRASS (10.65 to 11.5)
;     average pixels ivo 10.65 and compare to pixels ivo of 11.5
;     which is in peak in senescent grass (from JHU)

```

```

lambdaA=[10.6,10.7]
lambdaB=[11.4,11.6]
blackbody_veg=screen(allatmdata(*,vegetation),lambda,lambdaA,lambdaB, $
                    vegetation_threshold)
selected=vegetation(blackbody_veg)
count=n_elements(selected)
print, ' Selected ',count, ' pixels'

; DISPLAY PLOT OF STRIP

one_two_three='1'

read, 'Select a plot option: (1) none, (2) postscript, (3) screen: ', $
    one_two_three

case 1 of
    (one_two_three eq 2): begin
        set_plot,'ps'
        device,file='window.ps',/helvetica,/bold,bits=8
        do_plot,infile,reform(atmdata(63,*,*)),spawin,framewin, $
            2,25,vegetation,'All Vegetation',selected,'Healthy'
        device,/close_file
        set_plot,'x'
        end
    (one_two_three eq 3): begin
        set_plot,'x'
        device,true=24,retain=2
        zoom=950/n_elements(framewin)
        if (zoom eq 0) then zoom=1
        window,0,xsize=3*zoom*n_elements(spawin)+20, $
            ysize=zoom*n_elements(framewin)+50
        do_plot,infile,reform(atmdata(63,*,*)),spawin,framewin, $
            zoom,1,vegetation,'Vegetation',selected,'Screened'
        end
else: print,''
endcase

read,'Enter Binsize: ',binsize

; FIND TMAX

bright=fltarr(128,count)
tbright=fltarr(count)

locations=intarr(count)

for i=0,count-1 do begin
    bright(*,i)=brightness(allatmdata(*,selected(i)),lambda(*,0))
    tbright(i)=max(rebin(bright(*,i),64))
    shortlambdarebin(lambdarebin(64))
    locations(i)=shortlambdarebin(!c)
endfor

histo=histogram(locations,min=0)
histomax=max(histo)

```

```

print, ' Most Tmax at ',shortlambda(!c,0)

; BASIC PLASTIC RULER FIT!

print, 'Doing BASIC correction'

; MAKE BLACK BODIES

allblackbodies=fltarr(128,count)

for i=0,count-1 do begin
    allblackbodies(*,i) = blackbody(tbright(i),lambda(*,0))
endfor

; DO CORRECTION CALC

HACKWELL: temp=fltarr(5,128)
correction=fltarr(5,128,128)

for i=0,127 do begin
    temp(*,i)= $
        ks_line(allblackbodies(i,indgen(count)), $
            allatmdata(i,selected),noise(i),binsize,f)
endfor

transmittance=temp(1,*)
upwelling=temp(0,*)

maxtrans=max(transmittance)
channel=!c
print, ' Max transmittance at ', wv(!c,63)

; PLOT TRANSMITTANCE CURVES

window,1
!p.multi=[0,1,2]
plot,wv(*,63),transmittance,title='Atmospheric Transmittance',$
    ytitle='Transmittance',xtitle='Wavelength (microns)'
xyouts,8,1.1,infile
text='Screening Thresholds: ' + string(sand_threshold) + $
    string(vegetation_threshold)
xyouts,8,.25,text
text='Binsize:' + string(binsize)
xyouts,8,.15,text

plot,wv(*,63),upwelling,title='Atmospheric Upwelling Radiance',$
    ytitle='Upwelling Radiance',xtitle='Wavelength (microns)'

window,2
!p.multi=0
plot,wv(*,63),(allatmdata(*,selected(100))-upwelling)/transmittance,/ynoz
oplot,wv(*,63),(allatmdata(*,selected(200))-upwelling)/transmittance
oplot,wv(*,63),(allatmdata(*,selected(300))-upwelling)/transmittance

; PERFORM LOOP

```

```

read,'Select new binsize or zero to stop: ',input
if (input ne 0) then begin
    binsize=input
    goto, HACKWELL
endif

```

```

; SAVE RESULTS

```

```

one_or_two='1'

```

```

openw,unit, outfile,/get_lun

```

```

print,'Saving BASIC results'
forwrt,unit,transmittance
forwrt,unit,upwelling

```

```

close,unit
free_lun,unit

```

```

end

```

#### ;FUNCTIONS AND PROCEDURES CALLED BY ATMOSPHERIC COMPENSATION ALGORITHM

```

; FUNCTION: wave.pro
;     Generated by R. Bongiovi, Aerospace Corporation
;     Returns an array containing the
;     wavelength for the SEBASS LWIR array using the
;     plastic filter data from 20 Oct 95 (file: cal1_48.36p.dat)

```

```

function wave

```

```

; Set up and return function

```

```

wavel = fltarr(128,128)
x = findgen(128)
a0 = 57.0758 - 0.0216030*x + 0.000100471*x^2
a1 = 1.03258 + 1.88537e-5*x + 9.25211e-8*x^2
a2 = replicate(-0.000100671,128)
for j = 0,127 do begin
    wavel(*,j) = sqrt(a0(j) + a1(j)*x + a2(j)*x^2)
endfor
;
return,wavel
end

```

```

; FUNCTION:  blackbody.pro
;           revision: 30 Mar 96

```

```

;     FUNCTION TO GENERATE BLACKBODY RADIANCE FOR AN INPUT TEMP (KELVIN)

```

```

;     INPUT:
;           temperature (kelvin)

```

```

;           float data
;           wv (um)
;           float array stored as dim(1),dim(2)
;           contains wavelength bins for calculation

;   OUTPUT:
;           radiance (uw/um cm^2 sr)
;           double float data

function blackbody,temp,wv

dim=size(wv)
radiance=dblarr(dim(1),dim(2))
c1=1.19104e10
c2=1.438769e4

radiance=c1/((wv^5)*(exp(c2/(wv*temp))-1))

return,radiance
end

; FUNCTION:  brightness.pro
;           revision: 15 AUG 96

;   FUNCTION TO GENERATE BRIGHTNESS TEMP FOR RADIANCE(uw/sr um cm^2)

;   INPUT:
;           radiance  FLOAT (,)   Radiance at each pixel
;           wav       FLTARR (,)  Wavelengths for each pixel

;   OUTPUT:
;           bright FLTARR(128,128) [kelvin]

function brightness,radiance,wav

dim=size(wav)
brightness=dblarr(dim(1),dim(2))
c1=1.19104e10
c2=1.438769e4

brightness=c2/(wav*log(c1/(wav^5*radiance)+1.0))

return,brightness
end

; PROCEDURE: screen.pro
;           Revision: 7 May 96

;   FUNCTION TO SCREEN DATA FOR SPECIFIC THRESHOLD OF
;   BRIGHTNESS VALUES

;   INPUT:
;           data      FLTARR(128,range) (array of radiance data)
;           index     INT (index of data elements to check)
;           lambda    FLTARR(SEBASS Wavelengths)

```

```

;          lambdaA  FLTARR(2) (range A)
;          lambdaB  FLTARR(2) (range B)
;          threshold FLT (threshold value)

;          OUTPUT:
;          noise    [noise(128,n_elements(SPAWIN))] FLTARR

function screen,data,lambda,lambdaA,lambdaB,threshold

x=size(data)
number=x(2)
wv=wave()

tempA=fltarr(number)
tempB=fltarr(number)

for i=0L, number-1 do begin
    x=where(wv(*,63) gt lambdaA(0) and wv(*,63) lt lambdaA(1),xcount)
    tempA(i)=total(brightness(data(x,i),lambda(x,0)))/xcount
    x=where(wv(*,63) gt lambdaB(0) and wv(*,63) lt lambdaB(1),xcount)
    tempB(i)=total(brightness(data(x,i),lambda(x,0)))/xcount
endfor

selection=where(abs(tempA-tempB) lt threshold)

return, selection

end

; PROCEDURE: do_plot.pro
;          Revision: 9 May 96

;          PROCEDURE TO PLOT STRIPS OF ATMOSPHERIC WINDOW

;          INPUT:
;          infile    STR (name of file)
;          strip     FLTARR(spectral,spatial)
;          spawin,framewin FLTARR(spatal and frame window index)
;          zoom      FLT (scale factor)
;          pos_factor FLT (multiplicative factor for PS plot)
;          screenA,screenB FLTARR(selected pixels)
;          nameA,nameB STR (name of selections)
;          OUTPUT:

pro do_plot,infile,strip,spawin,framewin,zoom,pos_factor,screenA,nameA, $
    screenB,nameB

plotstrip=rebin(strip,n_elements(spawin)*zoom,n_elements(framewin)*zoom)
min=min(plotstrip)
max=max(plotstrip)+.2*median(plotstrip)
plotstrip(0,0)=max
tvsc1,bytsc1(plotstrip,min,max),0,40*pos_factor

all_plotstrip=reform(strip,n_elements(spawin)*n_elements(framewin))
all_plotstrip(screenA)=max

```

```

plotstrip=reform(all_plotstrip,n_elements(spawin),n_elements(framewin))
plotstrip=rebin(plotstrip,n_elements(spawin)*zoom,n_elements(framewin)*zoom)
tvsc1,bytsc1(plotstrip,min,max),zoom*pos_factor*n_elements(spawin)+10, $
    40*pos_factor

```

```

all_plotstrip=reform(strip,n_elements(spawin)*n_elements(framewin))
all_plotstrip(screenB)=max
plotstrip=reform(all_plotstrip,n_elements(spawin),n_elements(framewin))
plotstrip=rebin(plotstrip,n_elements(spawin)*zoom,n_elements(framewin)*zoom)
tvsc1,bytsc1(plotstrip,min,max),2*zoom*pos_factor*n_elements(spawin)+20, $
    40*pos_factor

```

```

xyouts,0.15,.04,'Window',alignment = 0.5,size = 1.5,/normal
xyouts,0.5,.04,nameA,alignment = 0.5,size = 1.5,/normal
xyouts,0.85,.04,nameB,alignment = 0.5,size = 1.5,/normal
xyouts,.5,.01,infile,alignment = 0.5,size=.75,/normal

```

```
end
```

```

; FUNCTION: noise_estimate.pro
;     Revision: 31 Mar 96

```

```

;     FUNCTION TO PERFORM NOISE ESTIMATION REQUIRED FOR PLASTIC RULER
;     ATMOSPHERIC COMPENSATION

```

```

;     INPUT:
;         filename  STR(name of calibration file)
;         spatial   intarr(2- start and stop spatial windows)

```

```

;     OUTPUT:
;         noise     [noise(128,n_elements(SPAWIN))] FLTARR

```

```
function noise_estimate,filename,spatial
```

```
; LOAD IN CALIBRATION FILE
```

```
nracs=128
cal_data=fltarr(128,128,nracs)
```

```
openr, unit, filename,/get_lun
forrd,unit,cal_data
close,unit
```

```
; PERFORM NOISE ESTIMATE
```

```
noise=fltarr(128)
```

```
for i=0,127 do begin
    noise(i)=stdev(cal_data(i,spatial(0):spatial(1),*))
endfor
```

```
return,noise
```

```
end
```

## LIST OF REFERENCES

Anderson, R., Malila, W., Maxwell, R., Reed, L., Military Utility of Multispectral and Hyperspectral Sensors, Environmental Research Institute of Michigan, Ann Arbor, MI, 1994.

Billingsley, Frank P., Sommese, Anthony, Benz, Kenneth D., Wilson, Wayne H., Waters, C. Ralph, *MHS Southern Rainbow Data Analysis Report: Task 1*, Photon Research Associates, Inc., pp. 7, 8, 9-11, 1995.

Boisjolie, Lisa, *Western Rainbow Collections Mission Ground Truth*, TASC, January 1996.

Bongiovi, R.P., *SEBASS Program Brief*, Aerospace Corporation, 4 January 1995.

Bongiovi, R.P., Hackwell, J.A., Hayhurst, T.L., *Airborne LWIR Hyperspectral Measurements of Military Vehicles*, Aerospace Corporation, 1995.

Burke, M. L., *Application of Atmospheric Model Corrections to BASS Data*, Remote Sensing Department, Aerospace Corporation, August 1995.

Elachi, Charles, Introduction to the Physics and Techniques of Remote Sensing, John Wiley and Sons, New York, 1987.

Farrand, W.H., Singer, R.B., Merenyi, E., Retrieval of Apparent Surface Reflectance From AVIRIS Data: A Comparison of Empirical Line, Radiative Transfer, and Spectral Mixing Methods, *Remote Sensing of the Environment*, Vol.47, pp. 311-321, 1994.

Goetz, A.F.H., Vane, G., Solomon, J. E., Rock, B.N., Imaging Spectrometry for Earth Remote Sensing, *Science*, Vol. 228, pp. 1147-1153, 1985.

Hackwell, J., Hayhurst, T., *In-scene Atmospheric Compensation of Hyperspectral Data*, Aerospace Corporation, Aerospace Corporation, 1995.

Hackwell, J., Warren, D. W., Bongiovi, R. P., Hansel, S. J., Hayhurst, T. L., Mabry, D. J., Sivjee, M. G., Skinner, J. W., *LWIR/MWIR Imaging Hyperspectral Sensor for Airborne and Ground-Based Remote Sensing*, Aerospace Corporation, 1996.

John Hopkins University, *Report on Spectra of Yuma Background Materials*, 1995.

Johnson, B. R., *SEBASS Calibration for Western Rainbow Collection*, Aerospace Corporation, August 1996.

Kahle, Anne B., Goetz, Alexander, F. H., Mineralogic Information from a New Airborne Thermal Infrared Multispectral Scanner, *Science*, Vol. 222, pp.24 - 27, 1983.

Kidder, S.Q., Haar, T.H.V., Satellite Meteorology: An Introduction, Academic Press, San Diego, CA, pp. 50-68, 1995.

Kruse, F.A, Lefkoff, A. B., Boardman, J. W., Heidebrecht, K. B., Shapiro, A. T., Barloon, P. J., Goetz, A. F. H., The Spectral Image Processing System (SIPS)- Interactive Visualization and Analysis of Imaging Spectrometer Data, *Remote Sensing of the Environment*, Vol. 44, pp. 145- 163, 1993.

*MASINT HYPERSPECTRAL STUDY: Interim Progress Report*, Office of Research and Development, October 1995.

Multispectral Users Guide, Department of Defense, August 1995.

Operations Order, Exercise WESTERN RAINBOW, 10 October 1995.

Richards, J. A., Remote Sensing Digital Imagery Analysis: An Introduction, Springer-Verlag, Germany, pp. 13, 20-21, 133-140, 1993.

Rickard, L. J., Basedow, R., Zalewski, E., Silvergate, P., and Landers, M., HYDICE: An Airborne System for Hyperspectral Imaging. *Proceedings of Imaging Spectrometry of the Terrestrial Environment*, Vol. 1937, p. 173, 1993.

Rinker, J. N., Hyperspectral Imagery - What Is It? - What Can It Do?, Presented at the USACE Seventh Remote Sensing Symposium, 1990.

Santisteban, A., Munoz, L., Applications of Image Principal Component Technique to the Geological Study of a Structural Basin in Central Spain, Presented at the Machine Processing of Remotely Sensed Data Symposium, pp. 228, 1977.

Schowengerdt, Robert A., Multispectral Image Processing, Course from SPIE, Orlando, 1994.

Stocker, Alan D., Reed, Irving S., Yu, Xiaoli, Multi-Dimensional Signal Processing for Electro-Optical Target Detection, *SPIE Proceedings*, Vol. 1305, pp. 218-231, 1990.

*WESTERN RAINBOW: Camouflage, Concealment, and Deception Report*, Joint Camouflage, Concealment, and Deception Group, Department of Defense, January 1996.

Vane, G., Chrien, T. G., Enmark, H. T., Hansen, E. G., and Porter, W. M., The Airborne Visible/Infrared Imaging Spectrometer (AVIRIS), *Remote Sensing of the Environment*, Vol.44, pp. 127-143, 1993.

Zissis, G. J., Sources of Radiation, Volume 1, The Infrared & Electro-optical Systems Handbook, Infrared Information Analysis Center, Environmental Research Institute of Michigan, Ann Arbor, MI, pp. 26, 32, 83-86, 244, 1993.



## INITIAL DISTRIBUTION LIST

1. Defense Technical Information Center .....2  
8725 John J. Kingman Road., Ste 0944  
Ft. Belvoir, VA 22060-6218
2. Dudley Knox Library .....2  
Naval Postgraduate School  
411 Dyer Rd.  
Monterey, California 93943-5101
3. Director, Training and Education.....1  
MCCDC, Code C46  
1019 Elliot Rd.  
Quantico, Virginia 22134-5027
4. Director, Marine Corps Research Center.....2  
MCCDC, Code C40RC  
2040 Broadway Street  
Quantico, VA 22134-5107
5. Director, Studies and Analysis Division.....1  
MCCDC Code C45  
3300 Russel Road  
Quantico, VA 22134-5130
6. Richard C. Olsen, Code PH/OS .....5  
Department of Physics  
Naval Postgraduate School  
Monterey, California 93943-5002
7. Chairman, Code SP .....1  
Space Systems Academic Group  
Naval Postgraduate School  
Monterey, California 93943-5002
8. David Cleary, Code PH/CL.....1  
Department of Physics  
Naval Postgraduate School  
Monterey, California 93943-5002

9. James Justin .....1  
 ORD/ETD  
 MS 4132  
 Washington, D. C. 20505
  
10. Dr. Jim Baker .....1  
 ORD/ETD  
 MS 4132  
 Washington, D. C. 20505
  
11. Bob Alexander .....1  
 ORD/ETD  
 MS 4132  
 Washington, D. C. 20505
  
12. Captain A. LeGrow .....1  
 Department of the Navy, CNO  
 Code N632, Room 5P773, The Pentagon  
 Washington, D.C. 20350-2000
  
13. John A. Hackwell.....2  
 Space and Environment Technology Center  
 Aerospace Corporation  
 2350 E. El Segundo Bl.  
 El Segundo, California 90245-4691
  
14. Wayne H. Wilson.....1  
 Photon Research Associates, Inc.  
 5720 Oberlin Drive  
 San Diego, CA 92121-1723
  
15. Dr. John Schott .....1  
 Center for Imaging Science  
 Rochester Institute of Technology  
 54 Lomb Memorial Drive  
 Rochester, NY 14623-5604
  
16. Dr. Alex F. Goetz.....1  
 CSES/CIRES  
 Box 216  
 University of Colorado  
 Boulder, CO 80309

17. Commander, Naval Space Command .....1  
ATTN: N112  
5280 4<sup>th</sup> Street  
Dahlgren, VA 22448-5300
18. Captain Brian H. Collins, USMC .....2  
11828 Barryknoll  
Houston, TX 77024